12-13-2017

Development and Applications of a Real-time Magnetic Electron Energy Spectrometer for Use with Medical Linear Accelerators

Paul Ethan Maggi
Louisiana State University and Agricultural and Mechanical College, paul.e.maggi@gmail.com

DEVELOPMENT AND APPLICATIONS OF A REAL-TIME MAGNETIC ELECTRON ENERGY SPECTROMETER FOR USE WITH MEDICAL LINEAR ACCELERATORS

A Dissertation

Submitted to the Graduate Faculty of the
Louisiana State University and
Agricultural and Mechanical College
in partial fulfillment of the
requirements for the degree of
Doctor in Philosophy

in

The Department of Physics and Astronomy

by
Paul Ethan Maggi
B.S., California Polytechnic State University, San Luis Obispo, 2012
May 2018

ACKNOWLEDGEMENTS

I thank Kenneth Hogstrom for providing the initial idea for this project, as well as partial funding support. I thank Edison Liang of Rice University for providing the magnet block and measurements of the magnetic field. I thank my adviser, Kip Matthews for his advice, guidance, and patience during my tenure at LSU. Additionally, I thank the rest of my committee, Dana Browne, Robert Carver, Scott Marley, and Todd Monroe for their critiques and assistance. Lastly, I thank my wife Christine, who followed me from the beaches and mountains of California to the swamps of Louisiana while I continued my education.

TABLE OF CONTENTS

LIST OF TABLES

LIST OF FIGURES

ABSTRACT

Purpose – This work presents a design for a real-time electron energy spectrometer, and provides data analysis methods and characterization of the real-time system. This system is intended for use with medical linear accelerators (linacs). The goal is 1 Hz acquisition of the energy range 4-25 MeV, reconstructed in 0.1 MeV increments.

Methods – Our spectrometer uses a nominal 0.54 T permanent magnet block as the dispersive element and scintillating fibers coupled to a CCD camera as the position sensitive detector. A broad electron beam produced by a linac is collimated by a 6.35 mm dimeter aperture at the entrance to the spectrometer. The collimated beam is dispersed by the magnetic field onto a row of 60 vertical 1 mm x 1 mm square scintillating fibers mounted to a lateral face of the magnet. Detector response functions (DRFs) were created using a simplified physics model of the spectrometer to determine electron trajectories within the magnet block from the entrance aperture to the detector plane. The DRFs were used in an iterative method to transform the fiber signal intensity versus position into an energy spectrum. We made measurements on an Elekta Infinity linac; each available energy (7, 9, 10, 11, 13, 16, 20 MeV) was investigated. Measurements were used to assess setup reproducibility, pinhole mismatch, dose rate effects, temporal stability, and linac detuning.

Results – Our reconstruction method was able to reconstruct energy spectra from idealized simulations to within 0.14 MeV ± 0.28 MeV of the ideal FWHM value, and 0.06 MeV ± 0.12 MeV of the ideal most probable energy, E_{p0}. The measured spectral stability was consistent with the expected linac operating stability. The system achieved a refresh rate of 0.8 Hz during real-time operation.

Conclusions – We developed a real-time electron energy spectrometer that measures electron energies from 4 to 25 MeV with a continuous readout rate of 0.8 Hz. The device can be used for

assessing linac performance as a routine clinical tool, assist in diagnostic maintenance and repair, or potentially provide a more efficient method for beam tuning and matching.

1. INTRODUCTION

This work describes a real-time magnetic electron energy spectrometer designed for use with medical linear accelerators (linacs). This chapter summarizes the use of electron beams for cancer treatment, linac design and operation, and magnetic spectrometers. It provides the motivation for this project, and why a real-time spectrometer can be an important clinical tool.

1.1. Background and Significance

Currently, the three common methods of treating cancer are chemotherapy, surgery, and radiation. Of the approximately 2 million new cancer diagnoses expected in 2014[1], nearly two-thirds of these patients are treated with some form of radiation therapy[2]. The most common type of radiation therapy is external beam radiotherapy produced by linacs, comprising about 88% of the treatments in 2004. Special techniques such, as brachytherapy and Gamma Knife®, are based around the use of radioisotopes as the radiation source. According to the US Department of Energy, in 2009, there were an estimated 5,000 medical linacs in use throughout the world[3].

1.2. Overview of Electron Beams in Radiotherapy

High energy electrons have been used as a form of radiation therapy since the 1930s[4]. They are predominately used for treating superficial disease within 6 cm of the patient surface. Single field electron treatments are advantageous compared to single field photon treatments due to the electron's finite range, sharp distal and lateral falloff, and uniform dose plateau.

Selection of electron beam energy is crucial to ensure acceptable target coverage. Most modern clinical linacs are able to produce electron beams with nominal energies between 6 MeV and 20 MeV; this provides depths of the distal 90% dose line, R_{90}, in the range of 2-6 cm. When selecting a nominal energy for an electron beam, one selects an energy where R_{90} is past the

deepest edge of the planning target volume. This provides adequate target coverage while minimizing dose to healthy tissue downstream from the target.

Linacs do not typically provide a continually adjustable output energy; they only produce a fixed set of nominal beam energies. Output energies are usually preconfigured by the vendor, but are tunable within a small range to match clinical requirements for R_{90}. The number and nominal values of the output energies vary by vendor (such as 6 and 18 MeV for Varian compared to 7 and 20 MeV for Elekta). The nominal energy value of a beam is not necessarily its actual energy, but rather represents the general therapeutic characteristics. For example, at the Mary Bird Perkins Cancer Center (MBPCC) in Baton Rouge, LA, the Elekta Infinity linac has nominal beam energies (in MeV) of 7, 9, 10, 11, 13, 16, and 20. These energies were tuned to provide R_{90} values (in mm) of 20, 25, 30, 35, 40, 50, and 60. At other cancer centers, beams of the same nominal energies may not be tuned to the same R_{90} values.

The percent dose deposited vs depth (PDD or depth-dose) behavior of an electron beam is illustrated in Figure 1. Initially dose builds up from the surface to the maximum dose (labeled D_m or D_{max}, at a depth of R_{100}). The maximum dose is commonly used as the normalization point (e.g. $D_m = 100\%$). Following this maximum dose, the dose sharply declines until the practical electron range (R_p) is reached. The low dose tail beyond the practical electron range results from bremsstrahlung x-rays produced by the electrons in both the linac and patient. R_{90}, the depth in the patient where the dose is 90% of the maximum, is generally taken as the therapeutic treatment range for electrons and is used when selecting an energy for treatment. R_{50}, the depth in the patient where the dose is 50% of the maximum, is used to specify beam quality for quality assurance (QA) and commissioning.

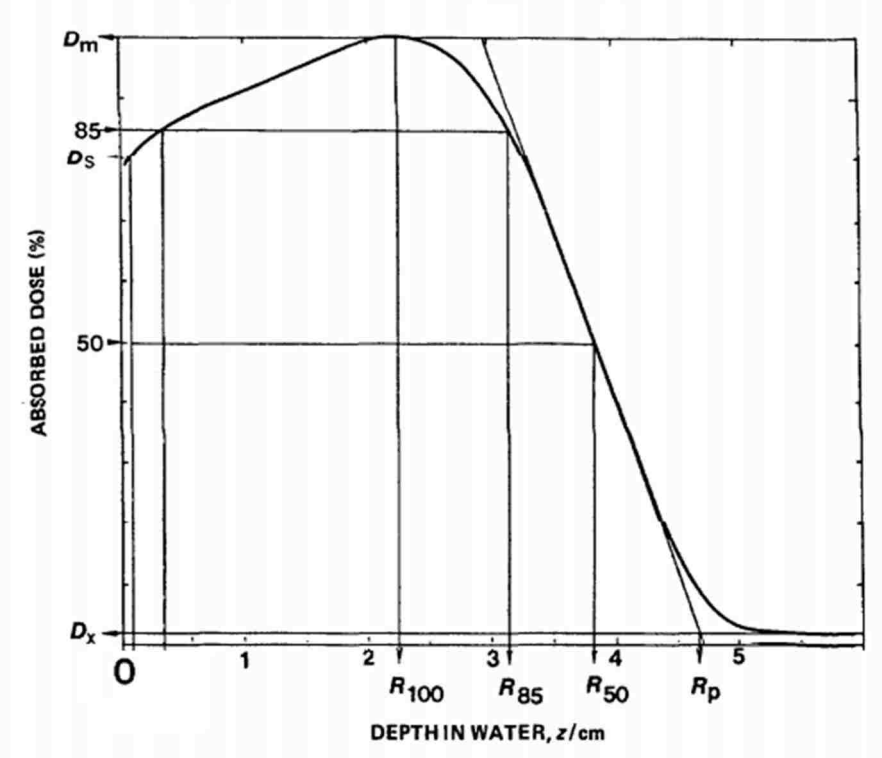

Figure 1. Absorbed-dose vs depth of a clinical electron beam in a water phantom. D_m is the maximum absorbed dose, D_s is the surface dose measured at a depth of 0.5 mm, D_x is the absorbed dose due to x-ray contamination, R_p, the practical electron range, is the depth where the steepest tangent intersects the D_x dose level, $R_{\#}$ are the depths at a given percent of the maximum dose (e.g. R_{50} is the depth of 50% of the maximum dose deposition), from ICRU[5].

The depth-dose behavior of an electron beam depends on its initial energy spectrum upon leaving the accelerator head. The energy spectrum is commonly modeled as a Gaussian distribution, specified by the peak (or most probable) energy and full width at half maximum (FWHM), plus a low energy tail, as shown in Figure 2; however non-Gaussian or multi-peaked spectra can occur [6]. A variety of empirical equations are used to relate the quantities that describe the energy spectrum to the parameters that describe the PDD. These include

$$\overline{E_0} = 0.656 + 2.059\,\mathrm{R}_{50} + 0.22R_{50}^2, \text{ in MeV}, \tag{1.1}$$

$$R_p = 1.271R_{50} - 0.23, \text{ in cm}, \text{ and} \tag{1.2}$$

$$\overline{E_d} = \overline{E}_0\left(1 - \tfrac{d}{R_p}\right), \text{ in MeV}, \tag{1.3}$$

where $\overline{E_0}$ is the mean incident energy in MeV at the patient or phantom surface, R_{50} is the depth in cm of 50% dose deposition, R_p is the practical range in cm, d is depth in cm, and $\overline{E_d}$ is the mean energy in MeV, at depth[7]. Other useful equations from ICRU 35[5] are

$$E_{p,0} = 0.22 + 1.98R_p + 0.0025R_p^2 \text{ and} \tag{1.4}$$

$$E_{p,0} = 1.95R_p + 0.48, \tag{1.5}$$

where R_p is in cm, and $E_{p,0}$ is in MeV. Equations 1.4 and 1.5 were originally derived for monoenergetic or narrow Gaussian beams, and agree to within ±1%. These relationships were extended to clinical beams and are consistent within 95% confidence bounds of ±0.8 MeV[8]. The depth-dose curve of a therapeutic electron beam strongly depends on the energy distribution of the incident beam, primarily the mean energy and most probable energy[5].

Depth-dose curves are typically measured using a large water tank with a small diode or ion chamber that is positioned at different depths in the tank. The depth-dose curve reflects the overall behavior of the energy spectrum, usually described in terms of composite descriptors such as $E_{p,0}$, $\overline{E}$, and FWHM. Methods to determine energy spectra include analytical back-calculations of energy spectra from PDD data[9] or by matching measured PDD data to iterative Monte Carlo simulations [10]. These predicted spectra are generated assuming a Gaussian spectrum that is not excessively broad (e.g. less than 15% FWHM), ignoring the low-energy tail[5] that results from beam conditioning for therapeutic use. Measurements[6,11], have shown that spectra for traveling-wave linacs can have additional spectral deviations further complicating the use of these descriptive quantities.

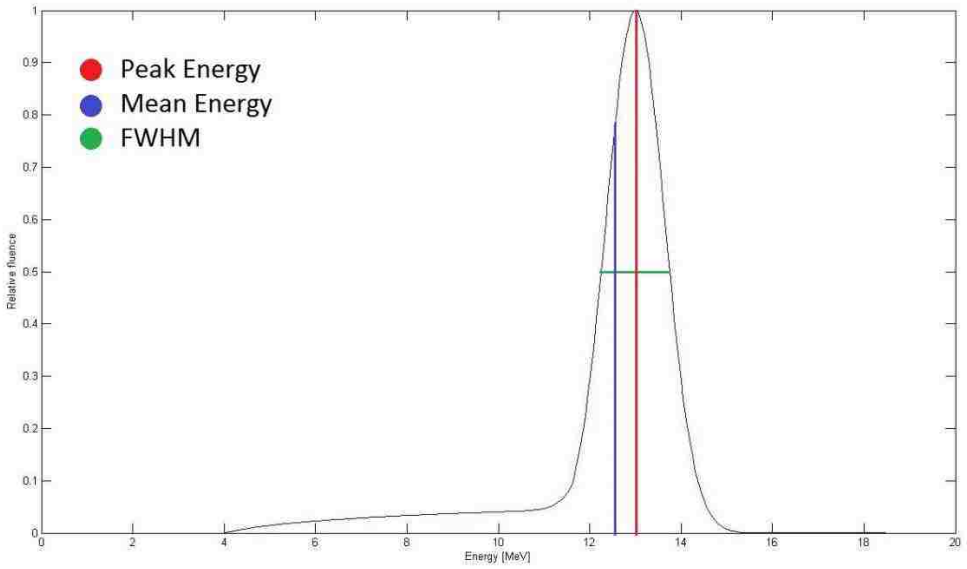

Figure 2. Hypothetical energy spectrum at the patient surface of a 13 MeV electron beam produced by a linac. The red line indicates the peak/most probably energy, the blue line indicates the mean energy, and the green line represents the full width at half max of the primary Gaussian portion of the spectrum.

Every linac requires post-installation commissioning and routine quality assurance (QA). Commissioning involves fully documenting the performance of the machine for use with treatment planning calculations and as the reference for QA. Guidelines for commissioning can be found in the AAPM TG-106 report[12]. A QA program verifies that a linac is functioning the same as it was during commissioning by routinely checking properties such as PDD measurements, ionization measurements at relevant depths (e.g. R_{50}), and spatial radiation profiles as outlined in the AAPM TG-142 report[13]. The key performance values of a linac are not generally based on factory specifications for that model of linac; rather, each clinic has its own preference for beam quality and tunes its linacs accordingly.

QA is primarily concerned with value constancy compared to the commissioned baseline reference. Most tolerance and matching criteria are specified as either a percent difference or a distance to agreement, such as 2%/2mm. This means for a dose point at a given depth, e.g. R_{50} measured to be 5.15 cm at the time of commissioning, repeat measurements for QA must be

within 2% (dose at 5.15 cm is 48%-52% of max), or the 50% dose value must occur within 2 mm from the initial point (4.95 cm to 5.35 cm). Tolerance values differ depending on the frequency of the QA tests; annual assessments have tighter acceptance tolerance values compared to daily or monthly tests. Not all tests are performed on all time scales; for example PDD measurements are generally only taken during annual QA or after machine service, while output measurements taken at R_{50} are routinely measured.

Some cancer centers with multiple linacs, such as MBPCC, prefer to have a single set of commissioning data that is used for all treatment planning and QA regardless of the linac. The process of tuning a linac's performance to match a reference data set is called beam matching. Having matched beams simplifies that treatment planning and delivery process, as a patient can be treated on any machine without the need for a re-plan, though it increases the complexity of linac commissioning. Commissioning an accelerator to match a clinical reference data set is an iterative process involving the physicists and service engineers. Matching is performed by repeatedly measuring PDD curves while slightly modifying linac operating parameters between measurements. The beam matching criteria for electrons used at MBPCC is 2%/0.5 mm. Additional information about beam matching for electrons can be found in[14]. Linac operating parameters and their effect on beam energy are discussed in Section 1.4.

1.3. Linac Design Overview

The majority of accelerators used for radiotherapy since the 1990s have been electron linacs. A linac consists of an electron source; a microwave power generator; an accelerating structure; beam redirection magnets; and additional components for shaping, broadening, and monitoring the beam. A block diagram of these systems is presented in Figure 3. Different accelerator vendors use different components and designs, such as a klystron-powered standing-wave linac

(Varian) or a magnetron-powered traveling-wave linac (Elekta). The focus of this section is on the Elekta configuration of a constant-impedance, traveling-wave, S-Band (2856 MHz) magnetron-powered linac with RF feedback. Detailed information on accelerator and RF theory can be found in[15-18].

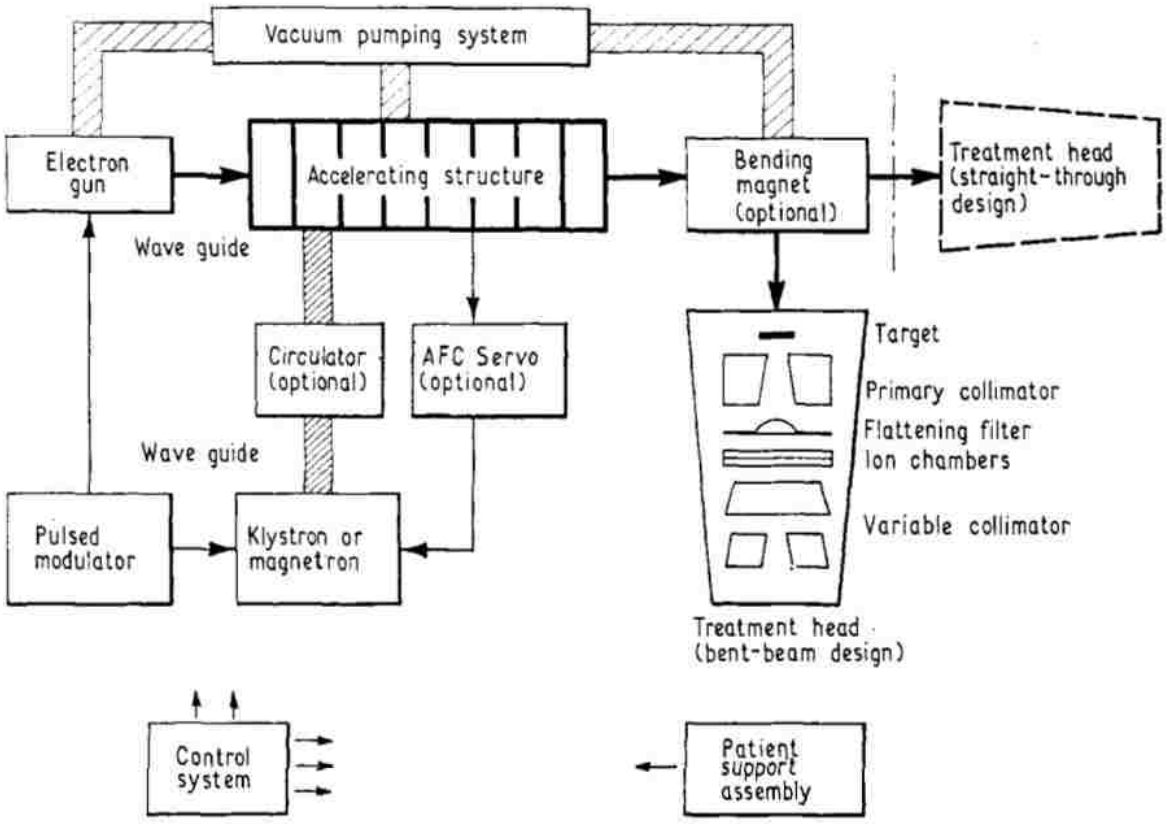

Figure 3. Block diagram of a generic medical linac, from Karzmark[19].

1.4. Linac Properties Affecting the Energy Spectrum

The electron energy spectrum is governed by many aspects of linac operation. They can be broadly classified as static properties that do not change after energy selection, and variable settings that can be modified or feedback controlled as part of energy selection.

1.4.1. Static Settings

Static modifiers of the electron energy spectrum include physical beam modifiers such as scattering foils and the vacuum exit window, and the acceptance range of the bending magnet system. The scattering foils are necessary to create the broad, flat beam used for treatments. The beam passes through the vacuum exit window, which maintains the high vacuum environment of the accelerating structure. The bending magnet system directs the beam from the accelerating structure towards the patient.

Most scattering foil systems use a dual foil setup[20], with the first foil being a high-Z material, and the second a low-Z material. Each linac has multiple sets of scattering foils available for different energies. The vacuum exit widow is usually a thin sheet of low-Z metal, such as nickel, that the electrons must pass through. As the electron beam passes through these physical beam modifiers, the energy spectrum changes from an initial narrow Gaussian distribution with an average energy approximately equal to the most probable energy, to a broader Gaussian with a low energy tail where the average energy is lower than the most probable energy[21,22]. Figure 4 illustrates the effect on the energy spectrum of the beam passing through a layer of aluminum. This demonstrates the spectral broadening of an electron beam passing through a material, changing the spectrum from a narrow Gaussian distribution to a broad distribution with a low energy tail.

Knowledge of the approximate energy loss through the scattering foils and vacuum window is needed to better relate the measured energy spectrum to the linac performance because the high energy electrons output by the accelerating structure and bending magnets must pass through the vacuum window and scattering foil to reach the patient. For an Elekta Infinity[21]

provides the approximate energy loss of the beam at different energies when passing through these structures.

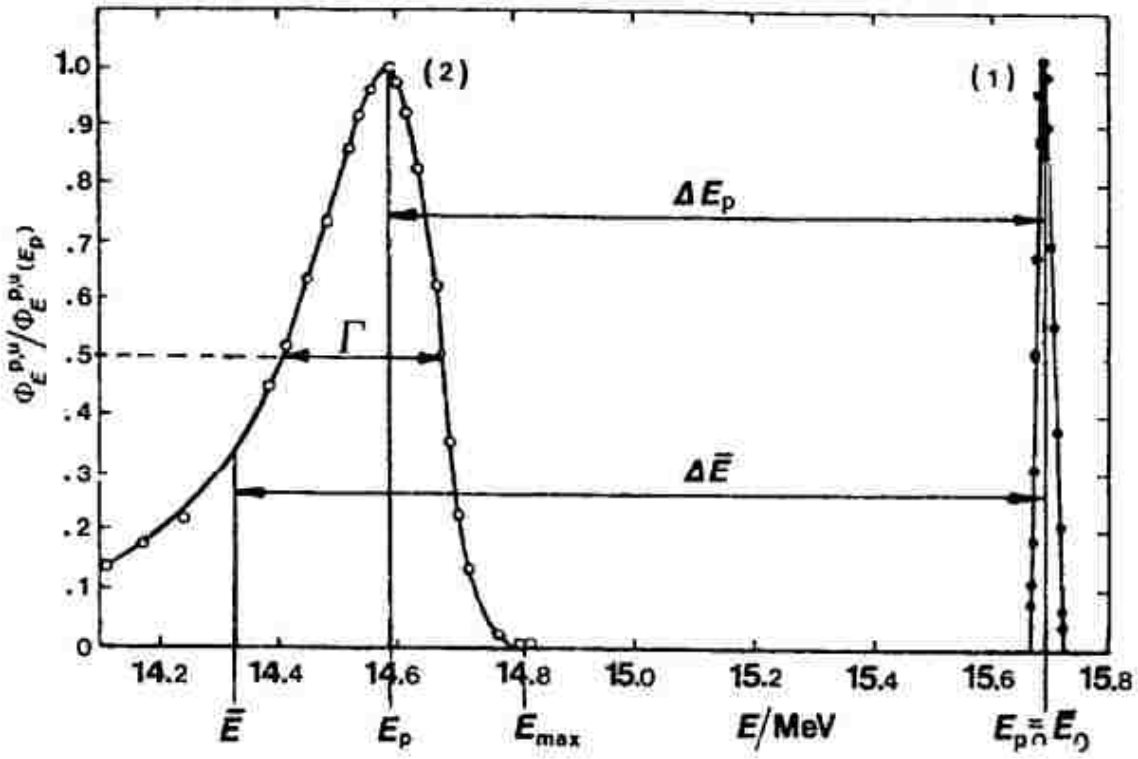

Figure 4. Energy spectrum of electrons beams before and after passing through material. Energy distribution of an "unobstructed" betatron beam (1) and of electrons that have passed through 0.86 g/cm2 of aluminum (2). Experimental values are given by the points. The apparent width of the "unobstructed" electron beam was mainly due to the limited resolution of the spectrometer (Goldwasser et al., 1952). The solid curve (2) agrees approximately with the energy distribution predicted theoretically by Landau (1944). Figure and caption from ICRU 35[5].

The energy acceptance aperture in the bending magnet system defines the maximum energy spread of the initial Gaussian spectrum, as depicted in Figure 5. The location of the energy slits depends on the optics system design, and is usually located at the point of maximum energy spread in an achromatic optics system. Energy slits can be additional physical devices inserted into the flight tube, or the flight tube itself. The acceptance slits physically block electrons with energies outside of the desired range from continuing down the accelerator. Kok reported an

energy acceptance window of ±9% for the optics system on Philips SL-25 linacs with a slalom magnet system[23], which was the basis for modern Elekta linacs; the acceptance range varies depending on manufacturer and model.

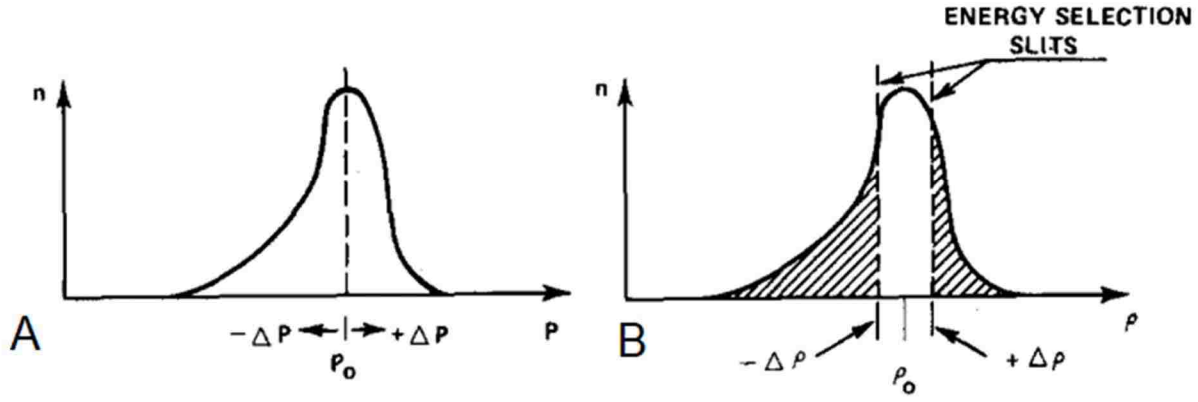

Figure 5. Effect of energy selection slits. A) Intrinsic energy spectrum produced by an accelerator. B) Depiction of limiting the energy spread using energy selection slits (shaded area removed). Increasing (or decreasing) the physical width of the energy selection slits allows for a wider (or narrower) range of energies to pass through the accelerator. Figure modified from Karzmark[24].

1.4.2. Variable Settings

Variable settings are adjustable parameters that govern the transient linac operation. These include RF source (magnetron) settings, electron source settings (electron gun current, voltage), pulse forming network charge rate, RF feedback system (high power phase shifter). Many of these components (e.g., magnetron and electron gun) have servo-controlled, automatic feedback for improved stability. The bending magnets and the RF feedback system are described below because they are the primary settings used in tuning the beam energy (personal communications, Alex Solodkin and Wayne Avren, Elekta Inc.).

1.4.2.1. Bending Magnets

Bending magnet systems are used to redirect the beam of electrons leaving the accelerating structure towards the patient, usually a 90º bend. Modern bending magnet systems are designed

to be achromatic, and are usually made of multiple dipole elements. The achromatic, double focusing magnet system in many Elekta linacs uses a slalom magnet arrangement[25-27] as shown in Figure 6. Magnets M1 and M2 have the same bending angle and radius of curvature, while magnet M3 provides the final bend to redirect the beam towards the patient.

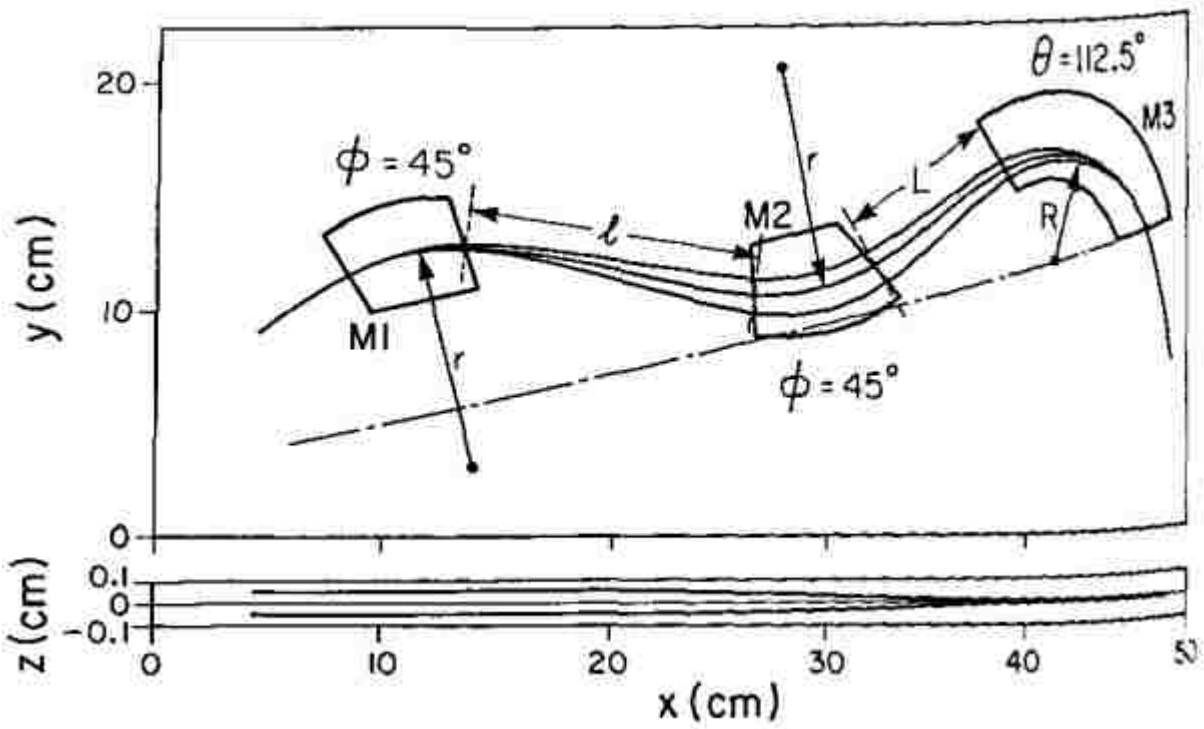

Figure 6. Layout of bending system. Rays of different energy (±6% energy spread) are indicated. Monoenergetic parallel beams have a crossover in M_2 after M_3. Image and caption from Botman[26].

For this three magnet system, two equations must be satisfied[26]:

$$\sin(\theta) = 2\sin(\varphi)(1-\cos(\varphi)) + (\ell / r)\sin^2(\varphi) \tag{1.6}$$

$$R(1-\cos(\theta)) + L\sin(\theta) = 2r\cos(\varphi)(1-\cos(\varphi)) + \ell\cos(\varphi)\sin(\varphi) \tag{1.7}$$

with the variables defined in Figure 6. Calculating the bend radii of the magnets using the values of ℓ = 12.4 cm and L =7.4 cm from Bates[27] gives r =12.16 cm and R =3.18 cm.

The field strengths of the bending magnets are calculated using the magnetic rigidity equation for relativistic electrons,

$$3B\rho = (T^2 + 2E_0T)^{1/2} \tag{1.8}$$

where B is in Tesla, ρ is in cm, T is the kinetic energy in MeV/c, and E_0 is the rest energy, in MeV/c. Using values of T based on estimates of the average electron beam energy[21], along with a ±3% energy bandwidth (personal communication, Alex Solodkin, Elekta Inc.), calculated field strengths and approximate energy windows are listed in Table 1.

Table 1. Bending magnet strength and beam energy windows for a slalom magnet system and a ±3% energy bandwidth

Nominal Energy [MeV]	7	9	10	11	13	16	20
B [T]	0.21	0.27	0.29	0.34	0.39	0.48	0.61
Center Energy [MeV]	7.33	9.27	10.25	11.93	13.71	16.84	21.88
Min Energy [MeV]	7.11	8.99	9.94	11.57	13.30	16.33	21.22
Max Energy [MeV]	7.55	9.55	10.56	12.29	14.12	17.35	22.54

These magnetic field strengths are achievable using conventional water-cooled electromagnets operating outside of saturation. Plotting the beam energy versus the machine reported bending current (Figure 7) in M1 and M2 produced a line that provides the approximate center energy of the optics passband based on the bending current. Modifying the bending magnet current, along with changes to the RF power setting, is the main method used to change the linac output energy. This relationship has also been used to try to back calculate the intrinsic energy spectrum of the beam[28].

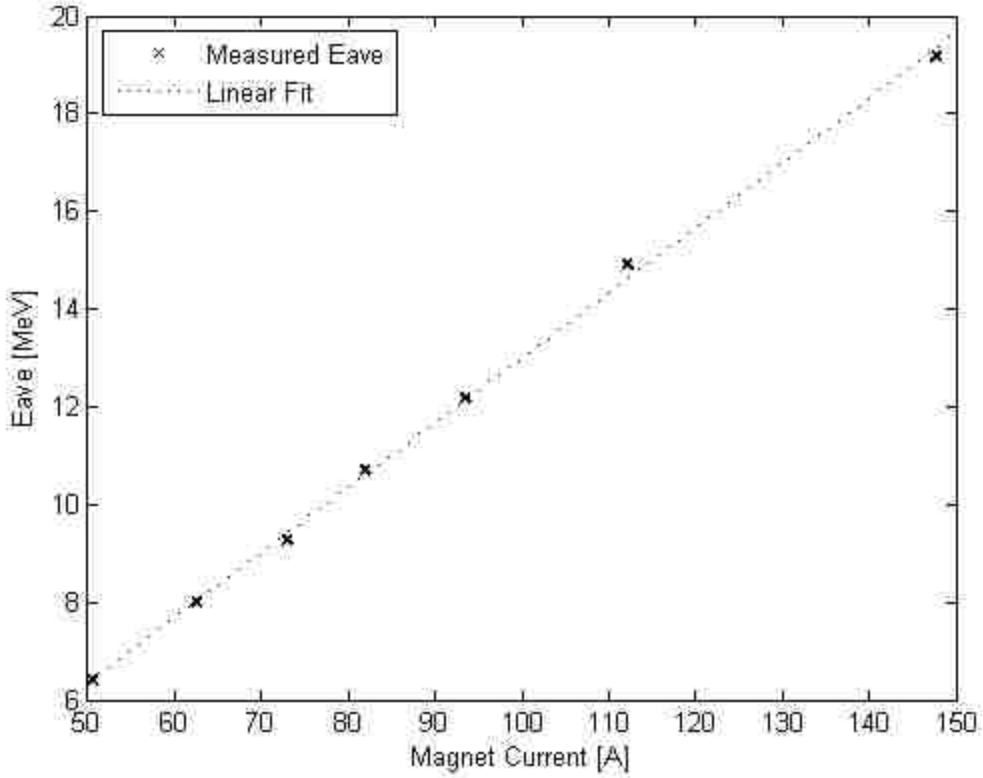

Figure 7. Use of magnet current in energy selection. The magnet current is the current in magnets M1 and M2. Eave is the measured average energy of the electrons. The slope of the linear fit is 0.13 MeV/A.

1.4.2.2. RF Recirculation and the High Power Phase Shifter

Magnetron powered traveling wave linacs are not able to reach electron energies higher than ~18 MeV without recycling a portion of the unused RF energy[29]. For the constant impedance traveling wave linac modeled in, ~15% of the input RF power can be reused to accelerate electrons to higher energies. The phase of this recycled RF must be matched to the phase of the incident RF to increase the output energy and improve overall linac stability. This matching is achieved by using a phase shifter.

Phase shifters are two port devices that alter the relative phase between the input and output of the device. This can be achieved through a variety of ways, such as line stretching, ferrites, and diodes. High power applications such as linacs use a Riblet coupler with two shorted

ports[30,31] as a phase shifter (Figure 8) inserted into the RF feedback system as in Figure 9. The phase change is controlled by adjusting the location of the short-circuit pistons via the motor drive shaft. For Elekta linacs, the servo connected to the motor drive shaft used for tuning is software controlled. The software variable reports a length, in cm; the RF in the accelerator has a wavelength of ~10.5 cm, so a 1 cm movement of the piston corresponds to a 10.9º phase change between the input and output.

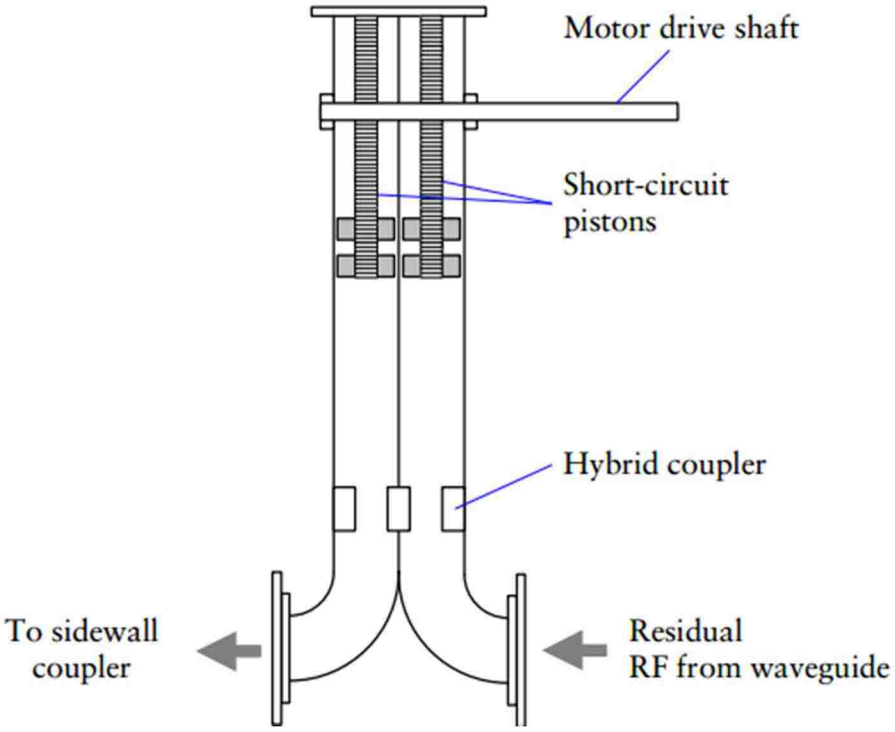

Figure 8. Waveguide high power phase shifter based on a Riblet coupler design, from Elekta[32].

1.5. Review of Charged Particle Analysis Techniques

Charged particle analysis techniques seek to classify a partially known or unknown field of particles (e.g. ions and molecules) by mass to charge ratio, momentum to charge ratio, or by energy. The former is known as mass spectrometry, and is used to primarily determine what species of ions and molecules comprise a sample or mixture. Energy and momentum

spectrometry seek to classify a cohort of particles with a known mass to charge ratio by the energy distribution of the particles. Energy spectrometry is the focus of this dissertation.

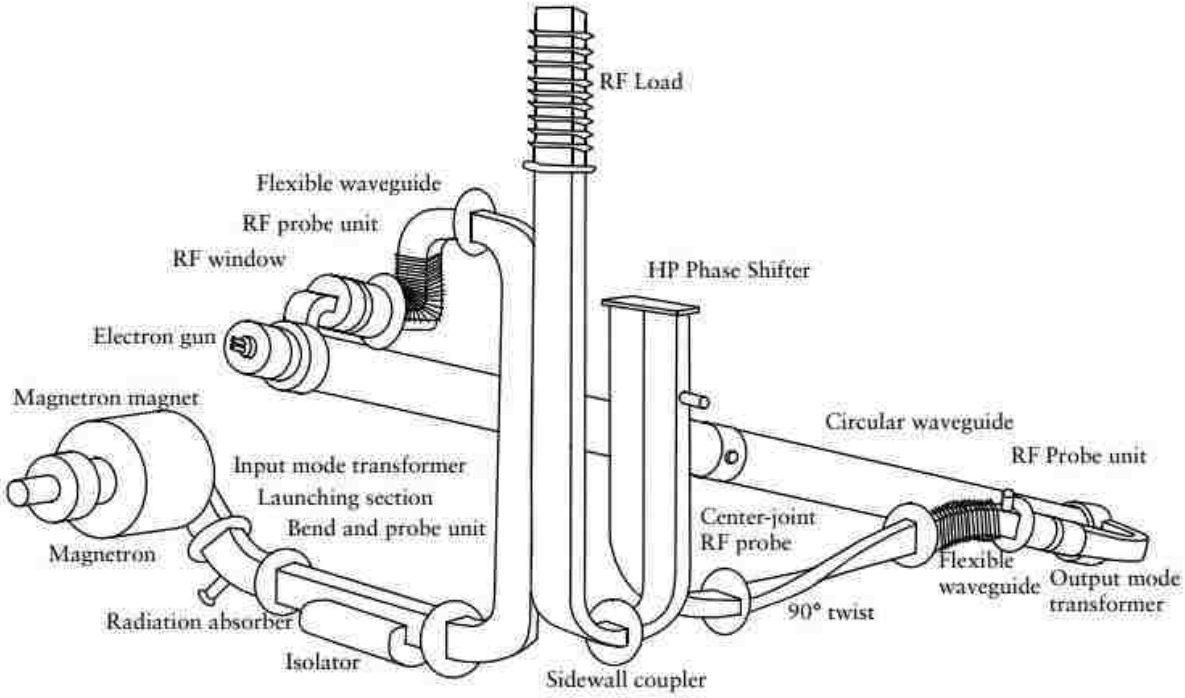

Figure 9. Diagram of the RF system in an Elekta accelerator[32]. The high power phase shifter is located near the center of the figure, and is part of the RF feedback path.

Roy and Tremblay[33] identify four principles or methods of energy analysis: resonant collision phenomenon, time of flight, retardation by a potential barrier, and dispersion in a deflecting field. These methods are discussed in more detail by Enge[34]. Of these four methods, dispersion by a deflecting field has seen the most use and is the method used in this work.

Deflecting field spectrometers operate on one concise relationship: the Lorentz Force Law,

$$\vec{F} = q\left(\vec{E} + \vec{v} \times \vec{B}\right) \tag{1.9}$$

where $\vec{F}$ is the resultant force, q is the particle charge, $\vec{E}$ is the electric field strength experienced by the particle, $\vec{v}$ is the particle velocity, and $\vec{B}$ is the magnetic field strength

experienced by the particle. This law states that a charged particle experiences a force parallel to an applied electric field, and perpendicular to both the velocity vector and magnetic field vector. This gives rise to the use of electric, magnetic, or combined fields to separate charged particles based on their charge to mass ratio or charge to momentum ratio.

The choice of whether to use electric, magnetic, or hybrid fields strongly depends on the kinetic energy of the particle. For non-relativistic particles, any field combination can be used. For relativistic particles, the required electric field strengths become difficult to generate and magnetic fields are primarily used. Electrons are relativistic in the therapeutic energy range. Additional information on relativistic effects can be found in any modern physics textbook (e.g. Helliwell[35]).

1.6. Magnetic Spectrometer Concept

In magnetic spectrometers, the electron velocity and force due to the magnetic field are perpendicular, resulting in the electrons traversing paths of constant radius (Figure 10). The radius of curvature is energy dependent, and can be calculated using equation (1.8). Placing a position sensitive detector along the y-axis allows for a determination of an electron's energy based on its position at the detector plane.

Many magnetic spectrometers designs have been created in the past century. The review by Enge[36] provides a survey of several of the historic magnetic spectrometer systems and Siegbahn provides a detailed discussion of electron spectrometer theory and design[37]. Several spectrometers have been designed and used to study the electron beams produced by medical accelerators[11,38-41].

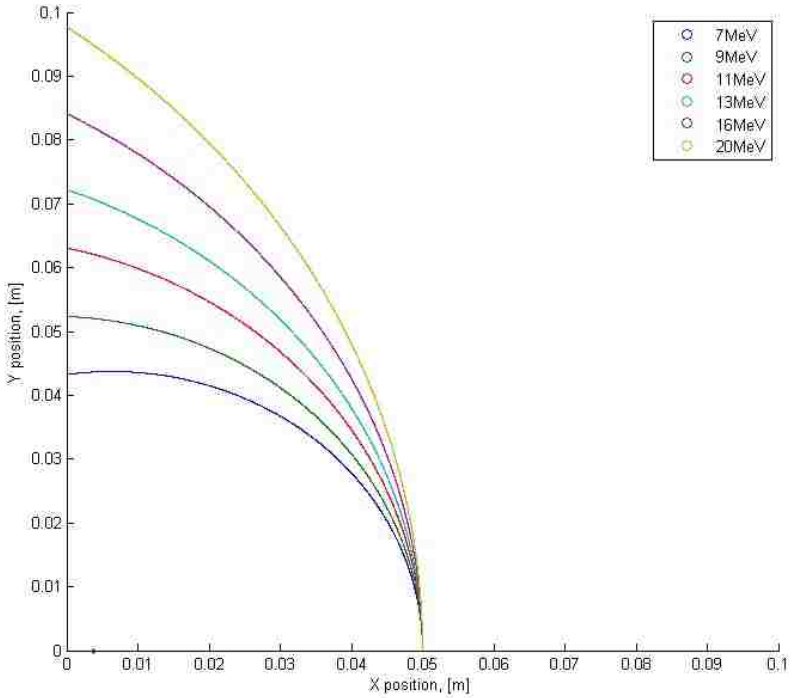

Figure 10. Movement of electrons in a 0.5 T magnetic field directed out of the page. The energies shown are representative of clinical electron energies. All electrons started at the same position, with their initial velocity in the y direction. Calculations performed using MATLAB (R2012a, MathWorks Inc., Natick, MA).

1.7. Passive Magnetic Spectrometer Using a CR Plate Detector

The spectrometer in[14,40] was the forerunner to the current project. This previous spectrometer (Figure 11) had three key differences compared to the spectrometer reported in this dissertation:

1) passive detector system with post-acquisition readout;

2) analytic model to convert spatial distribution of electrons into the energy spectrum; and

3) iterative processing of data requiring manual user input.

These differences are described below to facilitate comparison to the current project. The same magnet block was used for both spectrometers. In addition to a passive integrating detector, this prior system used a dual pinhole collimator and a lead x-ray block to reduce the background signal.

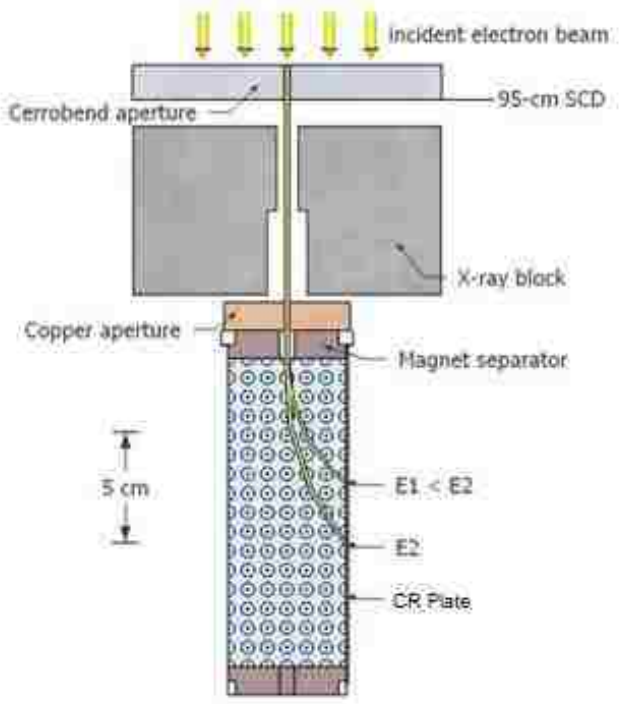

Figure 11. Top down view of the magnetic spectrometer of [14,40]. The Cerrobend and copper apertures define the pencil beam size at the entrance of the magnet block. (used with permission from McLaughlin[14])

1.7.1. Passive Detector System

The passive detector was a computed radiography (CR) imaging plate. A detailed discussion of CR can be found in[42]. A CR plate is a photostimulable phosphor layered on a flexible substrate. When exposed to ionizing radiation, a latent image is formed in the phosphor by trapping electrons in an excited state. When exposed to appropriate energy, such as the laser light of a CR readout system, the electrons are released and decay to a lower energy state, releasing visible light. The intensity of the released light is proportional to the absorbed dose in the CR plate. This light is recorded by a camera element in the readout system. A CR plate has a high spatial resolution, usually limited by laser spot size in the readout system.

As a passive detector, some time always elapses between when the CR plate is exposed and when the images are available for analysis, making CR plates unfit for real-time measurements. Unlike film, CR plates are reusable once they are fully erased by exposure to bright light.

1.7.2. Passive Detector Response Function

Due to the high spatial resolution of CR plates, and the use of a double pinhole collimation system, an analytic detector response function (DRF) could be defined. The double pin-hole collimator reduced the incoming electron beam from a wide area, multidirectional flood field to a nearly parallel pencil beam, described by

$$DRF(E,x)=\left[\left(\frac{r^2}{r^2-\left(x-x_0\right)^2}\right)\left(b^2-\left\{r-L_0\left[r^2-\left(x-x_0\right)^2\right]^{1/2}\right\}^2\right)\right]^{1/2} \tag{1.10}$$

with an energy-dependent r given by

$$r(E)=\frac{(E^2+2E_0E)^{1/2}}{3B} \tag{1.11}$$

where r is the radius of curvature of the electron with kinetic energy E, b is the aperture radius, L_0 is the distance from the magnet edge to the aperture center, x_0 is the offset between the magnet edge and the beginning of the detector, and x is the position along the detector face. The magnetic field, B, was modeled as a constant within the magnet block. Determination of the field strength and offset was based on a calibration procedure using the position of maximum intensity from a CR strip measurement compared to the most probably energy predicted based on Equation (1.4). Uncertainties in the E_{p0} value were not included in this calibration. The calibration curve is shown in Figure 12.

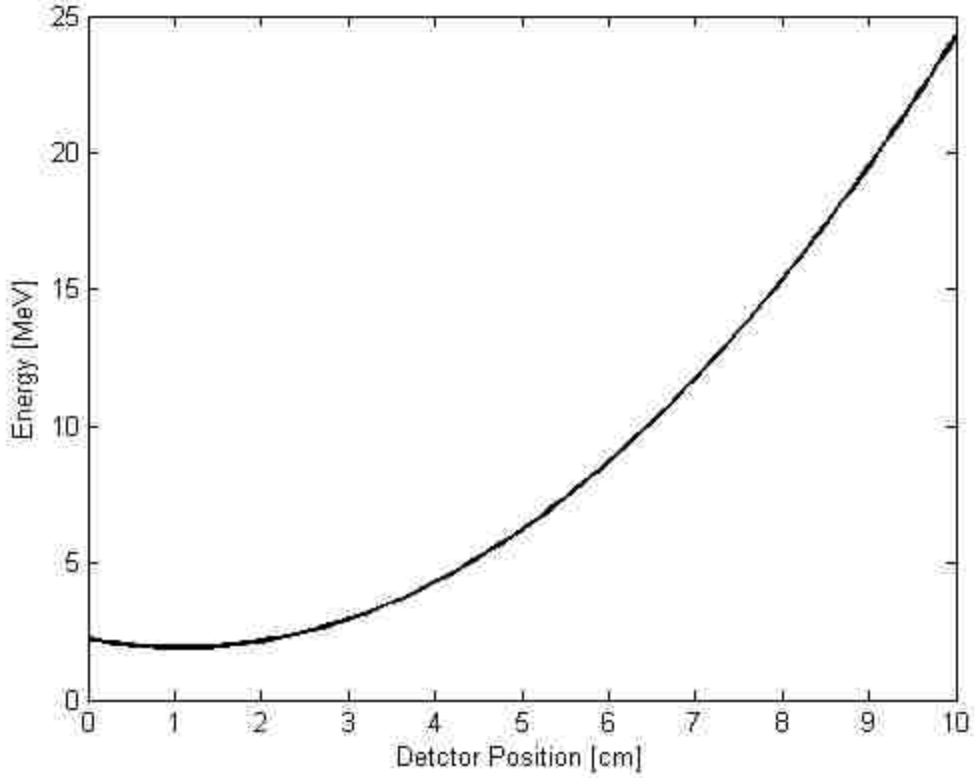

Figure 12. Position to energy relation determined based on the geometry in McLaughlin et al.[40] with a constant magnetic field strength of 0.5424 T and an offset of 1.066 cm between the magnetic field edge and the detector edge.

1.7.3. Spectral Unfolding Method

An iterative reconstruction method transformed the data to an energy spectrum based on

$$D(x) = \int_{E_{\min}(x)}^{E_{\max}(x)} \left(S/\rho \right) \bullet DRF(E,x) \bullet \phi(E,x) dE \tag{1.12}$$

where $D(x)$ is the dose (proportional to signal in the CR plate), $E_{\min}(x)$ and $E_{\max}(x)$ are the energy bounds for a specific x in the detector plane, S/ρ is the mass stopping power, $DRF(E,x)$ is defined in (1.10), and $\phi(E,x)$ is the particle fluence at x with energy E. The analysis method estimated a solution to $\phi(E,x)$, computed the resulting $D(x)$, and iterated to minimize the difference between the computed $D(x)$ and the measured $D(x)$. User input was

required to select the peak region for background subtraction and to select the appropriate smoothing parameters before the iterative fitting method was performed.

This analysis relied on two assumptions: 1) that the input beam defined by the dual pinholes was a parallel beam with no angular divergence and 2) the magnetic field was completely described by a constant value with a relative offset between the detector edge and the edge of the field. These assumptions were reasonable for the small aperture size and thin, high resolution CR plate. The real-time spectrometer of the present work did not use these assumptions, as described in Chapter 4.

1.8. Gap in Knowledge

There is currently no quick method to fully determine the energy spectrum of an electron beam, though several methods provide partial data. For example, Sun Nuclear's IC PROFILER (Sun Nuclear Corporation) has an accessory that provides an electron energy verification measurement as a surrogate for the entire spectrum. This method uses four metal wedges made of either copper or aluminum, and analyzes the change in R_{50} values[43]. Studies have attempted to determine the initial electron energy spectra by matching Monte Carlo simulations with measured depth-dose curves[10,44-49], but this is not a direct determination of the actual energy spectra produced by the linac.

Knowledge of the electron energy spectrum is valuable for both treatment planning and QA. Due to increases in computational power, radiotherapy treatment planning has been trending towards the use of Monte Carlo algorithms for dosimetry calculations. Monte Carlo simulations can fully model the physical processes involved in radiation transport. This can provide more accurate dose distributions than simplified analytic methods, especially in the presence of heterogeneities. However, Monte Carlo data is strongly dependent on the input parameters of the

simulation. The AAPM TG-105 report outlines the issues associated with the clinical use of Monte Carlo[50], stating that "the incident electron energy is the primary tuning parameter for electron beam simulations."

Magnetic spectrometers are a well established tool for measuring the energy of charged particles[37]. Previous spectrometers built for radiotherapy applications[38,40,41] have not operated in real-time due to the use of passive detectors, or scintillation detectors and swept magnetic field strengths to measure multiple narrow energy bands.

We have constructed a real-time spectrometer using a permanent magnet and an active integrating detector. This spectrometer design was initially proposed by Gahn et al.[51] for use in high intensity laser plasma studies.

1.9. Goal

The goal of this project was to create a real-time magnetic electron energy spectrometer for use with medical linear accelerators. The desired outcome was a clinical tool for commissioning, quality assurance, and accelerator tuning, as well as a tool for research.

1.10. Hypothesis

The real-time electron energy spectrometer system will provide an energy resolution of 0.3 MeV, a minimum readout rate of 1 Hz, and a usable energy range from 4 MeV to 25 MeV.

1.11. Specific Aims

We used the following specific aims to test the above hypothesis:

1.11.1. Implement and Characterize Acquisition Hardware

This aim is involves radiation detector selection, spectrometer assembly, and device characterization. The detector measures signal versus position after the electron beam is

dispersed spatially by the magnet as a function of energy. The detector size and spatial dispersion within the magnet must be capable of acquiring the 4 MeV to 25 MeV energy range.

1.11.2. Develop and Characterize Analysis Software

The software unfolds the fiber signal into an energy spectrum. The software also predicts the percent depth dose (PDD) curve. The software must be able to calculate and report the relevant descriptive quantities for the energy spectrum and the PDD curve within the desired 1 Hz readout rate.

1.11.3. Applications of the Spectrometer

This aim investigates the feasibility and utility of using the spectrometer as a quality assurance device for radiotherapy applications. The primary focus is measuring energy spectra for use as a constancy check, and comparing generated PDD curves based on the spectra to measured data. The spectrometer's ability to provide insight into the operation of a linac, and assist in the commissioning or tuning process is also investigated.

2. SPECTROMETER COMPONENT SELECTION, CHARACTERIZATION AND ASSEMBLY

The key hardware components of the real-time spectrometer are the magnet block, the radiation detector, and collimation system as shown generically in Figure 13. This chapter focuses on the individual hardware components of the spectrometer, while Chapter 3 assess the spectrometer as whole device.

The magnet block is described in section 2.1, and its magnetic field is characterized in Section 2.2. Section 2.3 surveys possible position sensitive radiation detectors; scintillating fibers and a CCD camera were chosen as the radiation detector for this device. Section 2.4 addresses fiber characterization and modifications. Camera characterization is discussed in section 2.6. Discussion of the collimation is in Section 2.7.

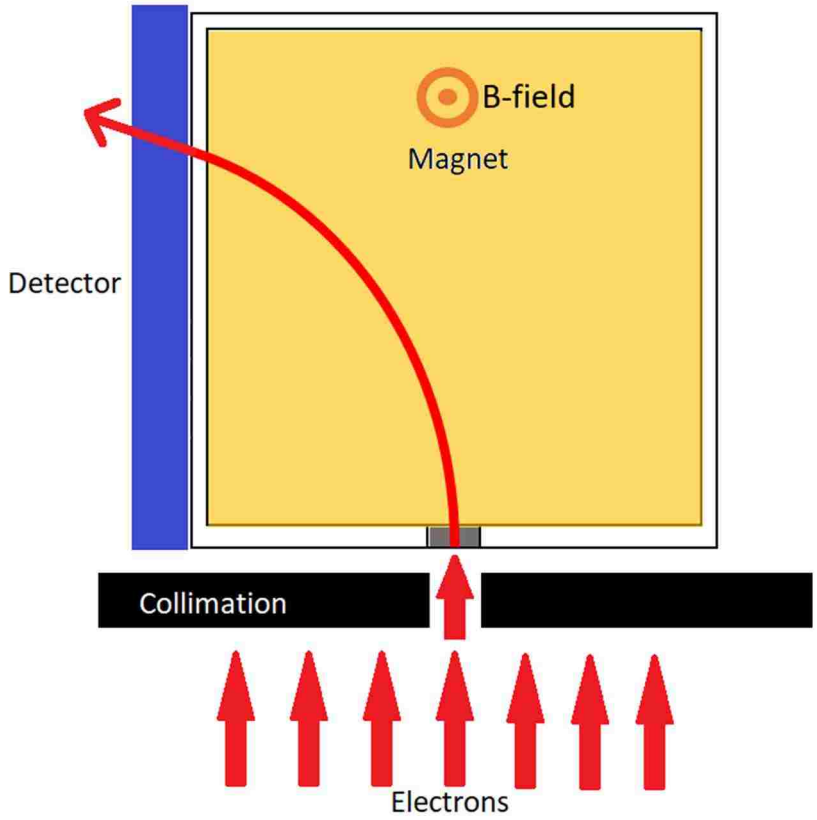

Figure 13. Diagram of a generic spectrometer.

2.1. Magnet Block

The magnet block for this project was the same magnet blocked used in the passive-detector spectrometer[14,40]. The individual magnet poles (Model NB085-5, Applied Magnets, Plano, TX) measured 15.24 cm x 5.08 cm x 2.54 cm. The poles are held apart with a 1.43 cm separation by a steel and aluminum frame (Figure 14). The electron beam after collimation (section 2.7) enters the magnet block through a 6.35 mm diameter aperture in the steel mounting face. The electrons exit the magnet block at the detector plane, which is the face lateral to the entrance face.

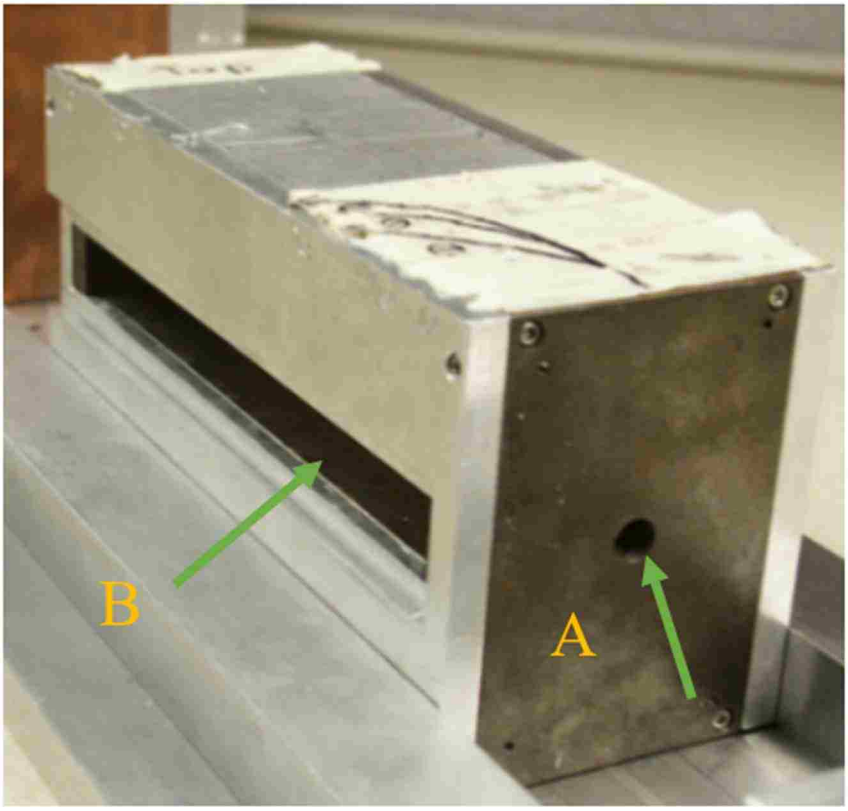

Figure 14. Photograph of magnet block showing the entrance aperture (A) and exit window (B).

2.2. Determination of the Magnetic Field and Calibration

The strength and shape of the magnet block determine its dispersion characteristics as a function of energy. The magnetic field model determines the position to energy relation at the detector plane, as well as the angle that electrons cross the detector plane. For McLaughlin[14,40],

with a high resolution thin detector located at the physical edge of the magnet, the assumption of a constant field strength was acceptable because the analysis was relatively insensitive to detector crossing-angle errors. Because of the active detector system used in this work (Section 2.4), we choose to implement a magnetic field map rather than assume a constant value for the magnetic field strength.

As shown in Figure 15, the use of a constant effective field value is only accurate at the physical edge of the magnet, and loses accuracy the farther a particle travels. The fiber ribbon in this spectrometer was located 6.4 mm beyond the physical edge of the magnet, where the effective value approximation loses accuracy. Additionally, the fibers were a comparatively thick detector, which increased uncertainties due to crossing angle effects. Because of these issues, we chose to implement a magnetic field map rather than assuming a constant value.

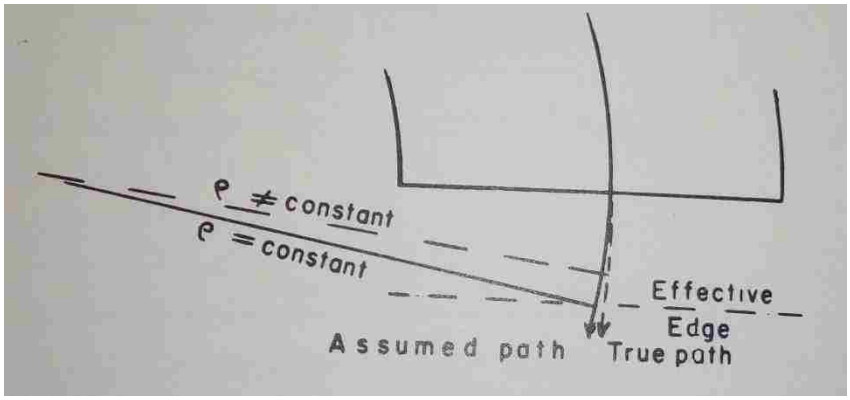

Figure 15. The effective edge concept introduces a small lateral displacement of the orbit. ρ is the radius of curvature of the electron. From Livingood[52].

2.2.1. Measured Versus Computational Field Models

We compared two approaches to create the magnetic field map: (1) field measurements (personal communication, Edison Long, Rice University), and (2) finite element modeling using COMSOL Multiphysics (AltaSim Technologies, Columbus, OH) with the magnet specifications provided (Model NB085-5, Applied Magnets, Plano, TX).

Measurements of the field strength were taken in quarter inch increments in the plane transverse to the main magnetic field. These measurements were only in the area bounded by the magnets, and did not include fringe fields where the fiber ribbon is located. The measured data included an apparent asymmetry in the measurements, noted as likely due to the probe being squished when performing measurements (personal communication, Edison Long, Rice University). The final measured field map is shown in Figure 16A.

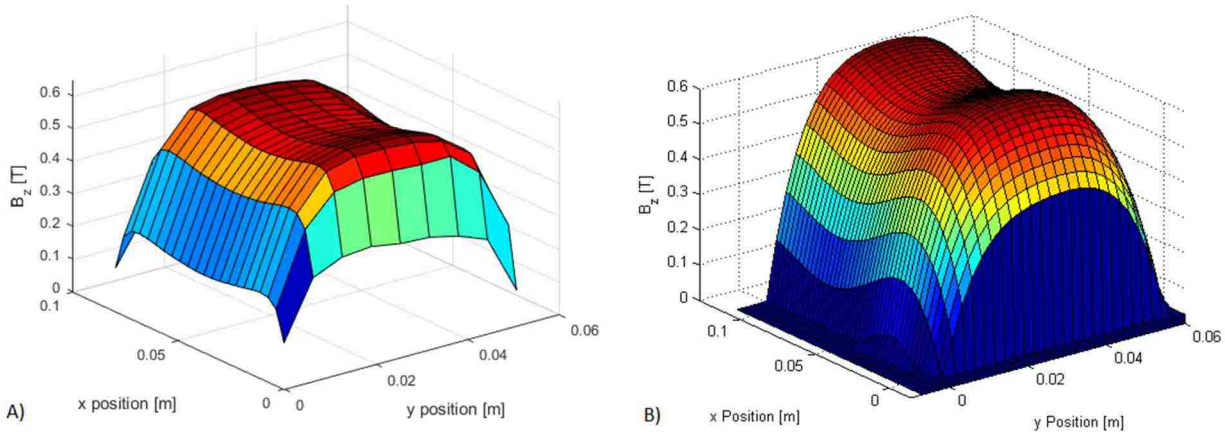

Figure 16. Surface plot of the two field maps. A) is the measured map. Note some asymmetry when comparing the left side to the right side, attributed to measurement bias. B) is the COMSOL map. The perspective for the field is the same orientation as Figure 14.

For the COMSOL model, we recreated the magnet geometry including the aluminum and steel frame (Figure 17). To model the magnets, we used a peak magnetization value of 13050 gauss, the middle of the vendor specified range of 12900-13200 gauss. The COMSOL field map is shown in Figure 16B.

To compare the field maps presented in Figure 16, we did a time-step propagation of electrons starting from the center of the magnet aperture (y = 0.02875 m) to the detector plane (y = -0.003675 m). We simulated electrons with energies between 4 and 25 MeV, in 1 MeV steps. We compared the predicted crossing locations and crossing angles of electrons as a function of energy (Figure 18). Additionally, we plotted the locations (Section 2.5.1) of the

maximum fiber signal acquired from the fully assembled device (Section 3.1) and their expected energy value based on equation (1.4). We assumed that the fiber with the maximum signal corresponded to the most probably energy, E_{p0}, and R_p values were referenced from the MBPCC clinical data book. This PDD based calibration method was used in McLaughlin[14,40].

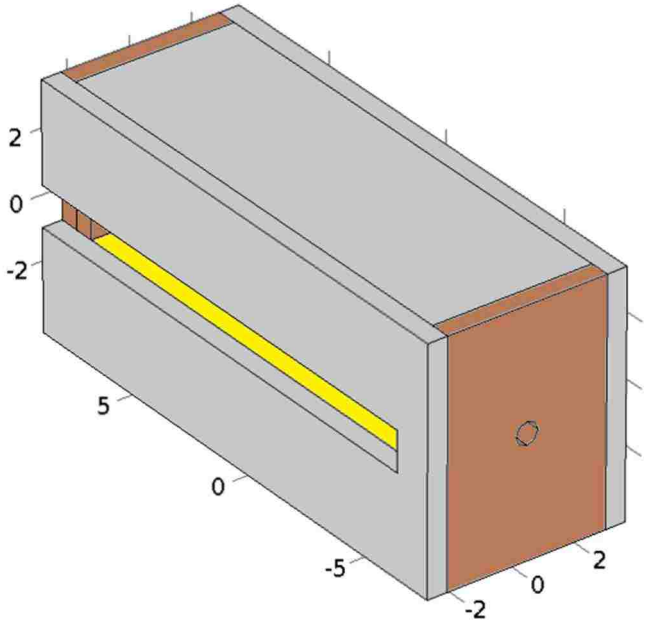

Figure 17. COMSOL model of the magnet block. The rust color indicates steel, the light grey indicates aluminum, and the yellow in the center is the top surface of the lower magnet. The units are cm.

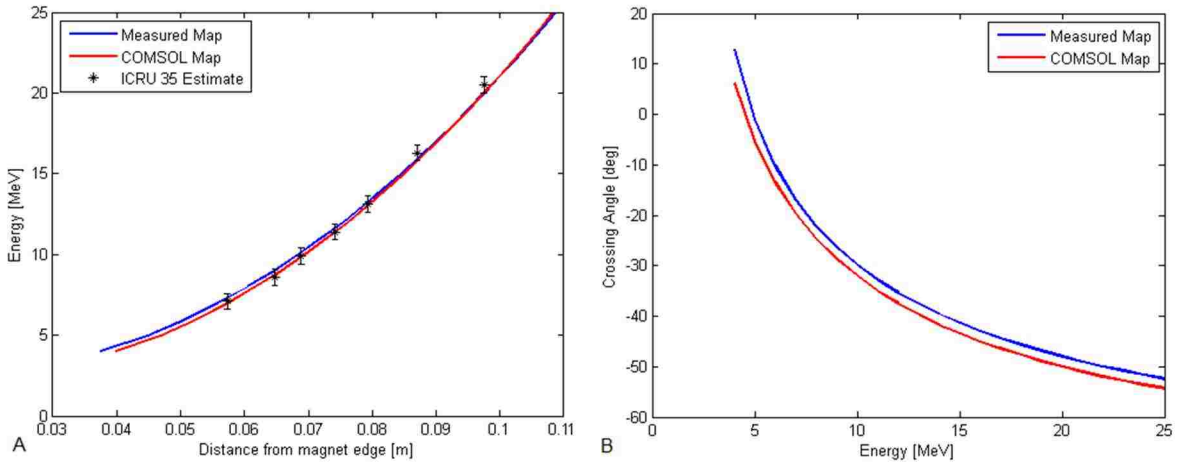

Figure 18. Comparisons of crossing locations (A) and crossing angles (B) for the measured field map and the COMSOL field map.

The average difference between the crossing locations was 0.6 ± 0.8 mm, with better agreement at higher energies. The two curves cross each other at slightly less than 10 cm/20 MeV. The crossing angles were shifted by approximately 5º. The close agreement between the two field maps suggest that either model is acceptable. Both field models were consistent with the PDD based verification method. Due to the known asymmetry in the measured field map and its sparse sampling interval, we used the COMSOL map the remainder of this work.

2.2.2. Effect of Fringe Fields, and Variations in Other Planes

In the previous section, the field analysis focused only on the B_z field, which is parallel to the fibers, and only at the x-y plane at the center of the aperture/magnet block. This section briefly addresses the effect of fringe fields and fields at different heights between the magnet poles.

Assuming a perpendicular field for the interior area between the two magnet blocks is an acceptable approximation taught in most physics textbooks; however this assumption is incorrect for the fringe fields at the magnet edge. This is illustrated in Figure 19. The result of these fields is a focusing-defocusing effect for electrons entering or leaving the magnet block. The net result of the fringe fields is difficult to model because the electron beam entering the spectrometer has an initial angular distribution, and experiences scatter in air. Furthermore, the fringe fields only act perpendicular to the primary field used for dispersion (e.g. it only alters the z position), and the fibers integrate along the $\hat{z}$ direction, minimizing this effect. This effect was noted, but ultimately not modeled as it was likely a small contribution to the overall uncertainty.

From the COMSOL model, there is a 2% average field strength difference for electrons at 3.18 mm above (or below) the center line between the magnet poles. When integrating over the total area of the aperture, field strength variations with height introduce a 1.8% uncertainty in B_z

compared to assuming a constant vertical field approximation. This 1.8% uncertainty is only correct for electrons with no velocity in the $\hat{z}$ direction (i.e. they do not change the x-y plane they're on and do not scatter). As mentioned above, the electrons in the magnet block experience scatter in air and start with an initial angular distribution, creating an averaging effect in the $\hat{z}$ direction. Fully modeling the fringe fields and vertical B_z variations would require detailed Monte Carlo simulations beyond the scope of this project.

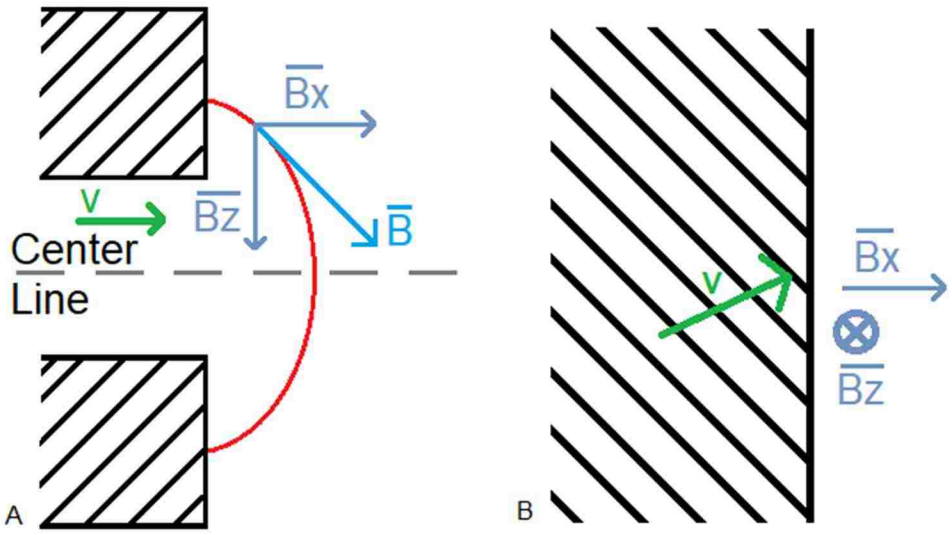

Figure 19. Depiction of fringing fields in two planes, elevation (A) and axial (B). The electron with velocity v (in green) exiting the magnet block experiences a magnetic field both in the x and $\hat{z}$ direction.

2.3. Radiation Detector Hardware Selection

This section investigates how the detector hardware affects the data acquisition and usability of the spectrometer. Based on the dispersion characteristics of magnet block (Figure 18), an ideal detector should be at least 60 mm long to span the exit points of electrons in the therapeutic energy range of 4-25 MeV. A scintillator plate with a camera imaging the plate either directly or via a mirror assembly or tapered light guide would be a straightforward solution. This schema of radiation detection has been historically used in radiation therapy for electronic portal imaging before the development of solid-state detectors53. However, for a 60 mm length scintillator, this

would require significant engineering of a tapered light guide, or it would need cumbersome, long focal length lenses for the camera.

Table 2 summarizes the detectors considered for use with this spectrometer. Other criteria for detector selection were:

1) Refresh rate: Refresh rate is determined by the detector readout speed due to the electronics, the detector radiation sensitivity, and integration time to achieve acceptable signal magnitude. Software data processing speed will also impact refresh rate. The desired refresh rate is 1 Hz.
2) Ease of use: Ease of use affects practical usability of the spectrometer as a clinical QA tool. It accounts for setup time, additional equipment needed for detector operation, and setup variability or complexity. Adequacy in this category is referenced to current clinical tools. For example, setting up a water-tank for PDD measurements would receive a poor rating (setup and use time >20 minutes); solid-water for dose measurements at R_{50} would receive an adequate rating (setup and use time of 10-20 minutes when factoring in data collection); and using an I.C. profiler would receive a very good rating (<5 minutes setup and use time).
3) Position sensitivity: Position sensitivity is important in the unfolding step of the spectrometer operation. In general, a higher position sensitivity (i.e. small detector elements) will result in a higher unfolded energy resolution. Adequate performance is the ability to discriminate between spectra shifted by 0.3 MeV, which corresponds to a change of R_{50} by ~1 mm.
4) Reliability/other: Reliability/other is an assessment of the detector's radiation hardness and ability to operate in a high RF noise environment of the linac vault.
5) Cost: Cost for a $\geq$ 60 mm active length detector.

A scintillator plate with a camera imaging the plate either directly or via a mirror assembly or tapered light guide would be a straightforward solution. This schema of radiation detection has been historically used in radiation therapy for electronic portal imaging before the development of solid-state detectors[53]. However, for a 60 mm length scintillator, this would require significant engineering of a tapered light guide, or it would need cumbersome, long focal length lenses for the camera.

Table 2. Detector Selection Criteria. "++" means the detector is very good, "+" means adequate, "+/-" indicates possibly adequate, and "–" means deficient. Cost is estimated using "$", with more "$" indicating a higher cost.

	Readout Speed	Ease of Use	Position Sensitivity	Reliability/other	Cost
Scintillator Plate + Camera + Lens/Mirror System	+	-	+	+/-	$-$$
Scintillating Fibers + Camera	+	+	+	+	$
Scintillating Fibers + CCD Line-readout	++	+	+	+/-	$$
Scintillating Fibers + Multianode PMT or SiPM	++	-	+	-	$$
Large-area Solid-state Detector, e.g. amorphous silicon	+	++	++	+	$$$

* CCD = charge-coupled device
# PMT = photomultiplier tube
^ SiPM = silicon photomultiplier

A row of scintillating fibers arranged at the edge of the magnet block, brought into a bundle, and imaged by a CCD camera has seen use in laser-plasma interaction studies[51]. The fibers act as the position sensitive detector, and allow the radiation sensitive camera to be located out of the

primary radiation field. Readout speed and position sensitivity are inversely related because increasing fiber size (increased light yield) results in worse position sensitivity. When mounted to the magnet block, this detector system would provide a reproducible setup without the need for additional electronics.

Instead of using a fiber bundle imaged by a CCD camera, a CCD or CMOS line readout sensor, such as a Hamamatsu S9979 (Hamamatsu Photonics K.K, Hamamatsu City, Japan), could view the ends of a fiber ribbon. While these sensors offer high light sensitivity and excellent intrinsic position sensitivity (decreased fiber size due to increased detector sensitivity), an individual detector element large enough to read the desired 60 mm is costly ($3400+), and would require significant electronic development to use. Multiple, less expensive sensors such as the Fairchild Imaging CCD 143A (Fairchild Imaging, San Jose, CA) have a sensitive length of ~26 mm with a total package size of ~37 mm, could be used. Additionally, operating a CCD sensor near a strong magnetic field could affect device performance, though no literature was available quantifying potential effects.

Scintillating fibers coupled to a multi-anode PMT such as the Hamamatsu H12428-100 (Hamamatsu Photonics K.K, Hamamatsu City, Japan), an array of conventional PMTs, or multiple multichannel SiPMs such as the Hamamatsu S13361-3050NE-08 (Hamamatsu Photonics K.K, Hamamatsu City, Japan) would offer high readout speed and good position sensitivity at the cost of poor stability in a high-noise environment. Additionally, arrays of PMTs and SiPMs require additional electronics, power supplies, and amplifiers to operate, complicating setup and use, greatly increasing cost and bulkiness.

Direct detection of the electron beam by a solid-state detector meets most performance requirements. These have seen use in many high radiation environments[54]; however a large-area

detector is much more expensive than other options, and much of the large field of view would go unused.

We selected the scintillating fibers + CCD camera as the radiation detector, as it's adequate in performance parameters, good in cost, and required no additional supporting electronics besides a laptop for the readout. The solution was especially cost effective in this instance because we already had scintillating fibers on hand, and experience working with these fibers. This detector setup only required purchasing a camera and creating the mounting hardware to attach the detector components to the magnet block

2.4. Fiber Preparation and Characterization

The scintillating fibers were Saint Gobain BCF-20 general purpose fibers (Saint Gobain S.A., Courbevoie, France). The scintillation properties are presented in Table 3 and Figure 20.

Table 3. BCF-20 Scintillating Fiber Properties, from Sain-Goabin[55]

Emission Color	Emission Peak	Decay Time	1/e Length	# of Photons per MeV	Trapping Efficiency
Green	492 nm	2.7 ns	>3.5 m	~8000	4.4 %

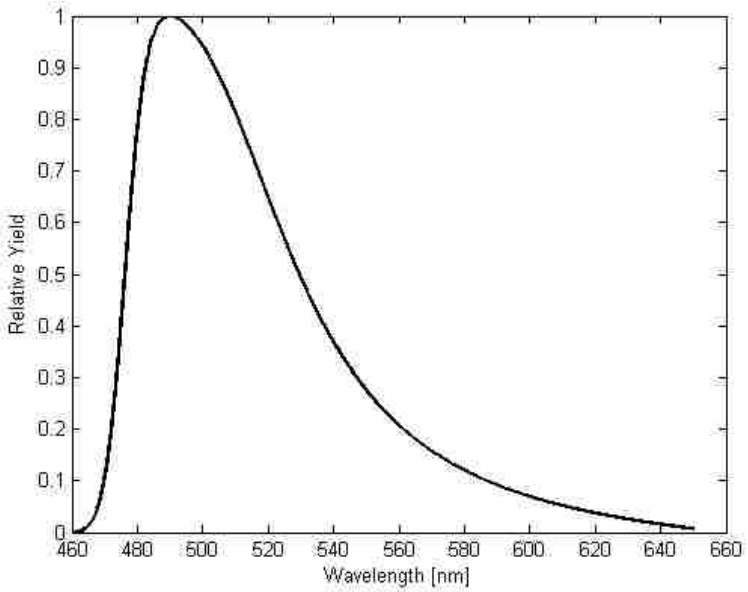

Figure 20. BCF-20 scintillating fiber emission spectra. From Saint-Goabin[55].

We used 1 mm square fibers, which have a size tolerance of 3% of the fiber width, with a standard deviation of approximately 0.5%. The fibers' ends were polished with successively finer sandpaper, ranging from #150 to #400 to #600 to #800 grit, concluding with white printer paper for a final polish. For a scintillation event, one expects half of the captured photons to be directed towards each end of a fiber.

The number of photons reaching the end of a fiber, N , is

$$N = Y \bullet E_{dep} \bullet \varepsilon \bullet \alpha \tag{2.1}$$

where Y is the number of photons produced per unit energy deposited, E_{dep} is the deposited energy, ε is the trapping efficiency of the fiber, and α is the 1/e attenuation due to the fiber length. Y , ε, and α are available from the vendor specifications[55]. For our application, E_{dep} is approximately the collisional stopping power, S, of an electron in polystyrene (the fiber core material), multiplied by its path length, l, through the fiber. As an example, a 10 MeV electron (S=2.03 MeV/cm in polystyrene) perpendicularly crossing of a 1 mm x 1 mm fiber (l = 0.1 cm) of length 25 cm at 5 cm from one end, should produce ~70 photons at the near end, and ~67 photons at the far end.

2.4.1. Fiber Profile Measurements

For quantifying fiber signal, we must determine how much light a fiber is emitting. The process of total internal reflection results in light being emitted as a Gaussian-like cone at the fiber end, with light extending beyond the physical edge of the fiber as shown in Figure 21. Approximately 45% of the light emitted by the fiber remains within the physical fiber edges. The remaining 55% of the light is spread to other areas. These light tails interfere with signal

quantification in nearby fibers; Section 3.2 describes our method for removing the effect of light spread to nearby fibers.

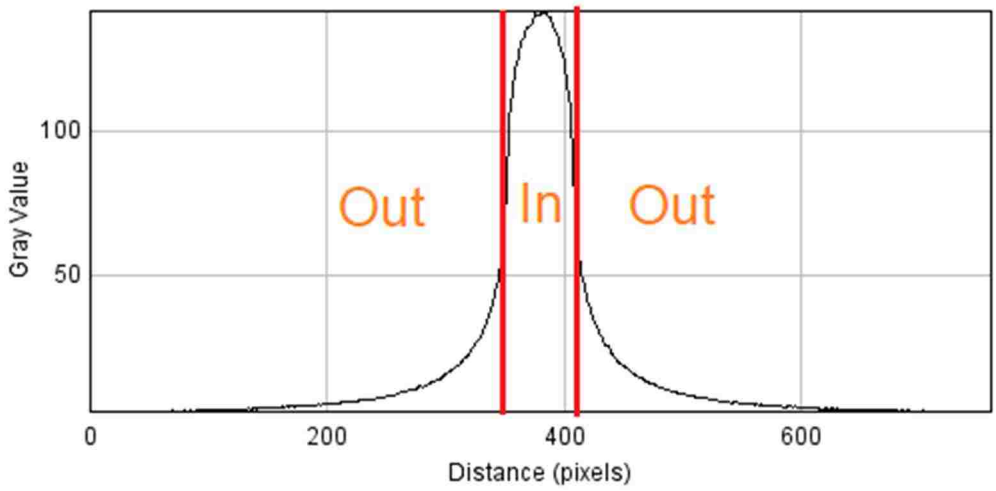

Figure 21. Light profile of a fiber through the center of the fiber. The vertical red line marks the physical fiber edge (labeled "In"). The profile area beyond the edge is labeled "Out."

2.4.2. Fiber Crosstalk Measurement

Fiber crosstalk is signal coupling between adjacent fibers resulting in a false signal appearing at the output of a fiber without an input[56]. It can result in a higher signal being measured than would otherwise be expected based on the input radiation.

The setup for the fiber crosstalk measurement is depicted in Figure 22. It used a photomultiplier tube (PMT, XP2202B, Photonis Technologies SAS, Mérignac, France) as the radiation detector and an green LED driven by a pulse generator as the light source. The PMT was powered by an ORTEC 556 High Voltage Supply (AMTEK ORTEC, Oak Ridge, TN) set to 600 V. The PMT output was fed into an ORTEC 572A Amplifier (AMTEK ORTEC, Oak Ridge, TN), set to a gain of 50, with a 0.5 μs shaping time and a unipolar output. The signal was measured using a Tektronix 5054 oscilloscope (Tektronix Inc, Beaverton, OR).

We placed two fibers, each 350 mm long, in physical contact, and varied the amount of overlap between them: 50 mm, 75 mm, and 100 mm. The fiber coupled to the LED passed

through a small hole in a piece of foam to ensure no light enter the "passive" fiber from the LED itself. Additionally, the fiber ends not at the PMT or LED were covered in black tape to further guarantee no stray light entered or exited these ends. Correction for variations in the 1/e attenuation in the fibers was neglected. The entire test setup was enclosed in a light-tight box.

Ideally to better simulate scintillation light production, we would have liked to conduct this test with a radioisotope source. However, preliminary tests showed we were not getting detectable signal using any of the available radiation sources. This was likely due to the low activity of our sources, the low radiation sensitivity of the fibers, and minimal crosstalk.

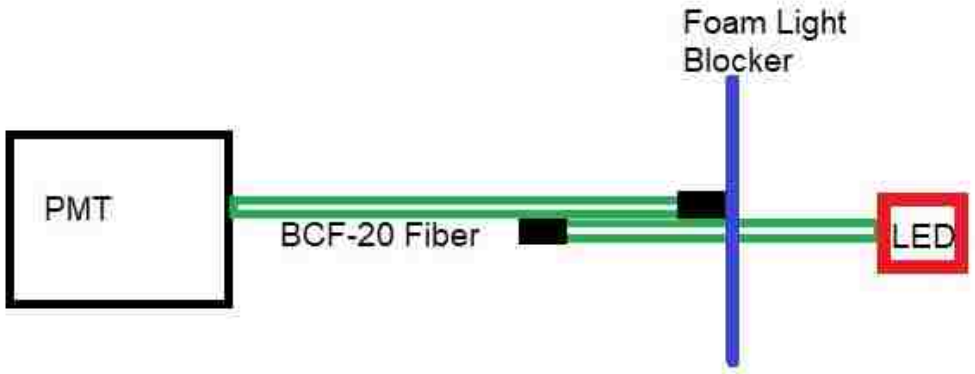

Figure 22. Setup of fiber crosstalk measurement.

The LED was driven by a 2.1 V (0 to 2.1 V) square wave at 10 kHz, and a 1% duty cycle from a Tektronix AFG 3021 function generator (Tektronix Inc, Beaverton, OR). Using a single 700 mm long fiber, the peak signal amplitude for light transmitted through a fiber, as determined by using the oscilloscope averaging function for 64 acquisitions, was 1.81 V; this value was used as our reference voltage for calculating crosstalk. The test results from the oscilloscope averaging function are summarized in Table 4.

Table 4. Crosstalk Measurement Results

	50 mm overlap	75 mm overlap	100 mm overlap
Measured Signal [V]	0.063	0.092	0.131
Crosstalk [%/mm]	0.0070	0.0068	0.0072

This gave an average signal sharing of 0.007±0.0002 %/mm, meaning if the ~220 mm fibers used to construct the detector were in continuous contact along their entire length, the crosstalk through the fiber cladding would be 1.54%. This source of signal sharing was neglected in all future studies.

2.4.3. Effect of Fiber End Coating

To increase the signal coming from the fiber, we investigated the effect of coating the fiber ends opposed to the camera with white reflective paint (Saint Gobain BC-620, Saint Gobain S.A., Courbevoie, France) as shown in Figure 23.

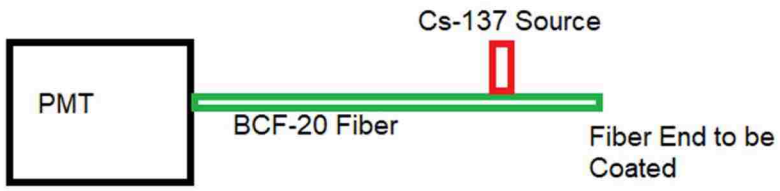

Figure 23. Setup of fiber signal enhancement due to end coating test.

We tested 1 m long, 2 mm square scintillating fibers coupled to a photomultiplier tube PMT (XP2202B, Photonis Technologies SAS, Mérignac, France) at one end, with a Cs-137 source located 5 cm from the opposing end. The PMT was powered by an Ortec 556 High Voltage Supply set to 1 kV. The PMT output was fed into an ORTEC 572A Amplifier (AMTEK ORTEC, Oak Ridge, TN), set to a gain of 50, with a 0.5 μs shaping time and a unipolar output. This was recorded with an ORTEC 551 (AMTEK ORTEC, Oak Ridge, TN) Counting and Timing Single Channel Analyzer (SCA), with a threshold of 200 mV. The signal acquisition time was 15 minutes. We measured background signal (e.g. no source at the fiber end), fiber signal pre-coating, and fiber signal after coating. The PMT, fiber, and source were enclosed in a

light tight box, and we waited 15 minutes between tests to let any residual noise caused by exposing the PMT to light dissipate.

Table 5. Effect of Coating Fiber Ends, SCA Counts in 15 Minutes.

	Background	No Coating	With Coating
Test 1	5699 ± 76	8921 ± 94	10417 ± 102
Test 2	5601 ± 75	8865 ± 94	10389 ± 102
Test 3	5662 ± 75	8929 ± 95	10314 ± 102
Average + Std Error	5654 ± 53	8905 ± 67	10373± 72

The average non-coated fiber signal after background subtraction was 3251 ± 85 counts; the average signal from the coated fibers after background subtraction was 4719 ± 89 counts. This give an average signal increase of 45% ± 4.8%. We used this coating method in our final version of the spectrometer (Figure 25). We assumed paint on the sides did not affect the resulting fiber signal.

2.5. Fiber Detector Assembly

60 scintillating fibers were arranged as a vertical ribbon at the exit face of the magnet block (Figure 24A). This created a 1-D position sensitive detector along the $\hat{x}$ direction (dispersion direction) that integrates signal over the $\hat{z}$ direction (parallel to magnetic). The fibers were held against the magnet block by an aluminum bracket. The bracket was designed and machined from multiple aluminum pieces. Design sketches for the bracket are provided in Appendix 1. This positions the center of the fiber ribbon 6.4 mm beyond the physical edge of the magnet block, which is in the fringes of the magnetic field.

To transform the 1-D detector at the exit face of the magnet block into a rectangle that was easily imaged by the CCD camera, we created a 2-D fiber bundle (Figure 24B). The bundle was created by arranging 6 groups of 10 scintillating fibers into a plastic “U” shaped holder. Each 10-fiber group was separated using a taped paper sheath. This grouping allowed easier

manipulation and arrangement of the fiber ribbon into a bundle. The fibers in the bundle were held in place by a plastic "T" with tightening screws through crossbar into the "U" arms. Two bundle arrangement variations are assessed in section 2.5.2.

The fiber order in the 1-D bundle was recorded during assembly and used when sorting and ordering the 2-D array (section 3.1.1). The performance of the CCD camera is addressed in Section 2.6. Section 2.5.1 discusses fiber location indexing, and Section 2.5.2 discusses bundling. Consistent position of the fiber bundle and camera was maintained by attaching the camera and bundle to a vertical plastic arm. This arm was mounted to the top of the magnet block using two square "U" brackets and tightening screws.

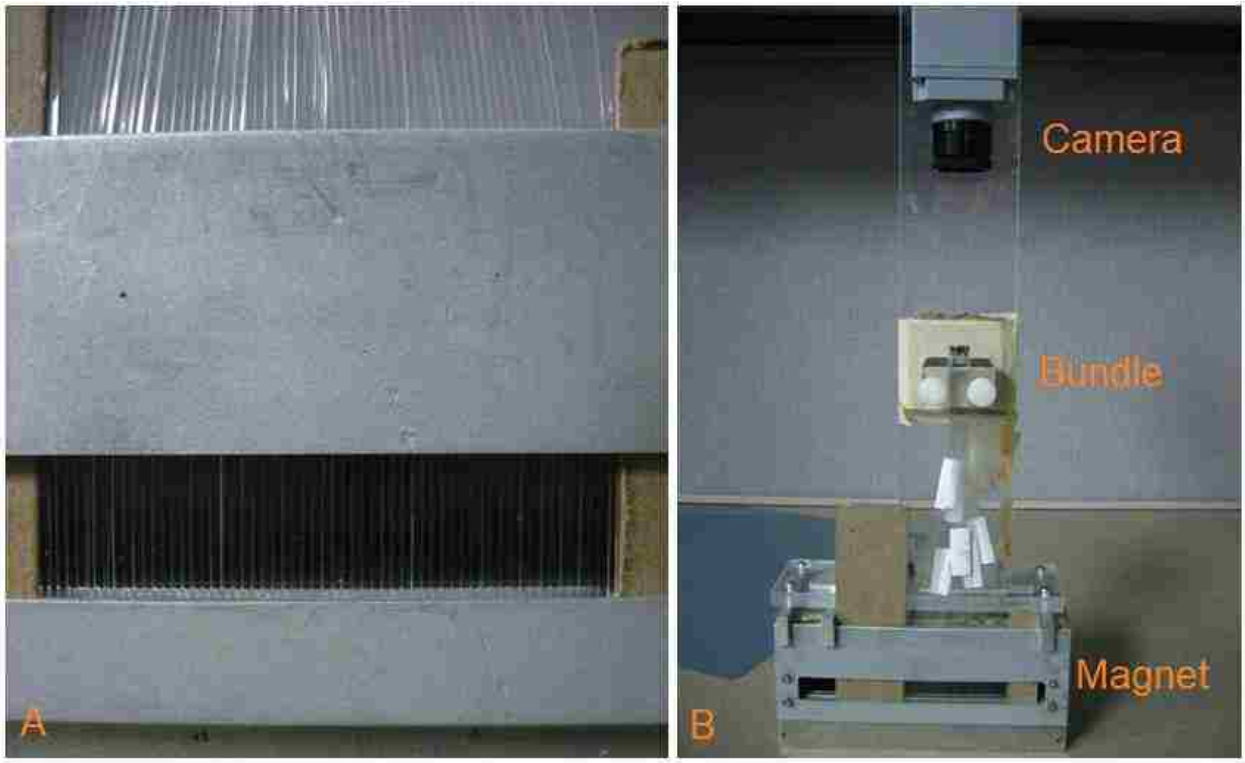

Figure 24. A) 1-D fiber array on the exit face of the magnet block. B) Geometry of spectrometer showing the magnet, fiber bundle, mounting hardware, and camera.

2.5.1. Fiber Location Indexing

Knowledge of the fiber locations with respect to the edge of the magnet block is crucial to the data unfolding process (Section 4.1). We indexed the fibers by taking high resolution photos of the assembled fiber ribbon (Figure 25) and measuring the fiber centers. To reduce camera lens distortions near the image edges, multiple images were acquired, and only the central regions were used for analysis. We overlapped a portion of the images to reduce data combination errors. We could not use assume the fiber centers were equally spaced with the interval total distance divided by the number of fibers because there were small gaps present every 10 fibers resulting from the bundling grouping method.

Figure 25. Example of an image used for final fiber location indexing showing the fiber ribbon at the exit face of the magnet block.

We determined the fiber centers using two methods: manual, visual selection using ImageJ [57]; and custom image analysis code that found the midpoint between the fiber edges. The image analysis code plotted a pixel intensity along the dispersion direction (left to right in Figure 25) to find the bright fiber edges relative to the darkened background (Figure 26). The pixel to distance conversion was created using the distance scale from the ruler. The results are summarized in Figure 27.

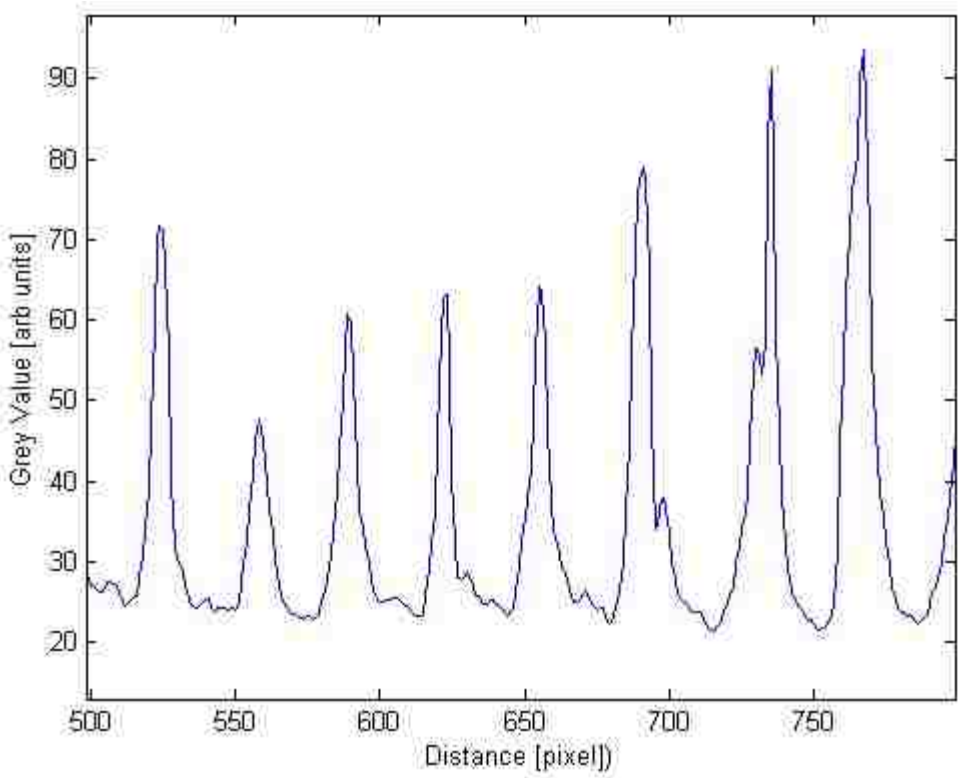

Figure 26. Grey value profile of 7 fibers. The midpoint between two peaks was used as the location of the fiber center.

The average difference between the two measurements was 0.06 ± 0.09 mm. We used average of the two methods as the location of the fiber center. The positions were known accurately so any residual uncertainty is unchanging, and should have little effect on the unfolded spectra.

2.5.2. Fiber Bundle Arrangement at Camera

We investigated two bundle arrangements: linearly packed, and checkerboard. Each bundle included both scintillating fibers, and non-scintillating, blackened fiber spacers. Both fiber arrangements were on a 12 fiber x 10 fiber grid (120 total fibers, 60 scintillating, 60 spacers). The bundle performance was assessed by analyzing profile measurements as they relate to fiber indexing, and what fiber signal corrections are easily achievable. The method for performing fiber indexing and signal correction is discussed in Chapter 3. The fibers used to create the bundle were approximately 22 cm in length (20 cm min, 25 cm max).

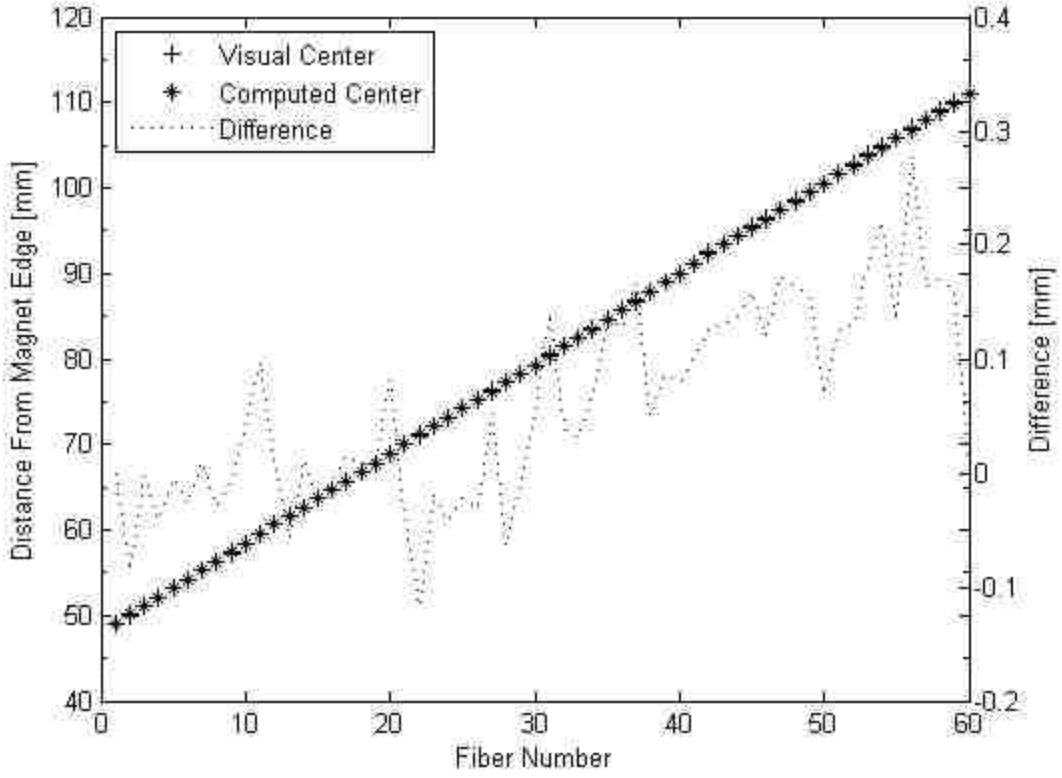

Figure 27. Fiber center indexing results comparing two methods of determining fiber centers.

2.5.2.1. Linearly Packed Bundle

This arrangement used 6 continuous rows of 10 scintillating fibers separated by a row of non-active 1 mm x 1 mm fibers as shown in Figure 28, with representative profiles shown in Figure

29-Figure 31. The 1-D ribbon in Figure 28A was directly irradiated using the flood acquisition procedure described in section 3.1.1. Figure 28B was acquired using spectrometry acquisition procedure described in 3.1.2.

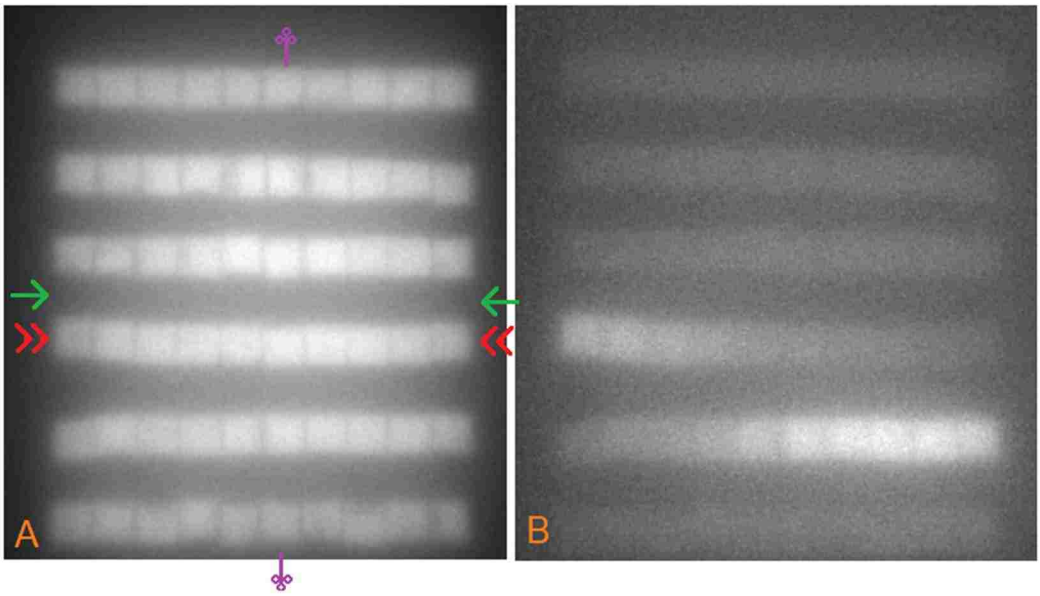

Figure 28. Linearly packed fiber bundle. A) Flood image taken by directly irradiating the 1-D ribbon with a uniform 20 MeV electron beam. The colored symbols mark the representative profiles in Figure 29-Figure 31. B) Spectrometer output with the bundle attached to the exit window of the magnet block, and irradiated through the spectrometer with a 20 MeV electron beam.

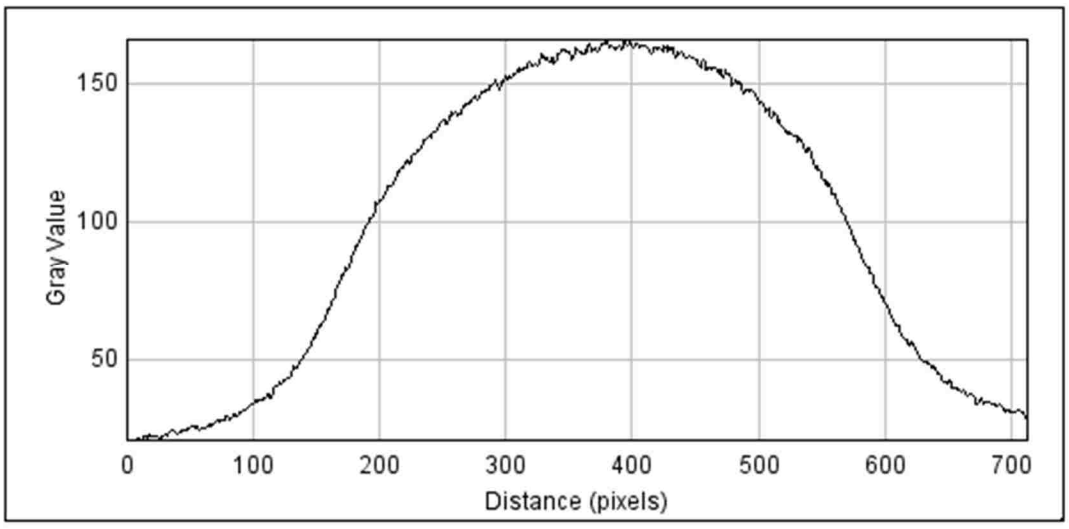

Figure 29. Horizontal signal profile near the center of the bundle across a row of space; profile location is marked by the green "→" in Figure 28A.

The effect of overlapping fiber light was clearly evident. As will be discussed later in Chapter 3, the first analysis step was to index the locations and bounds of each fiber. In Figure 30, the signal profile through a row of fibers showed that the individual fibers were poorly differentiated. In the vertical profile of Figure 31, the advantage of separating fibers with spacers was apparent, as individual fibers were more recognizable.

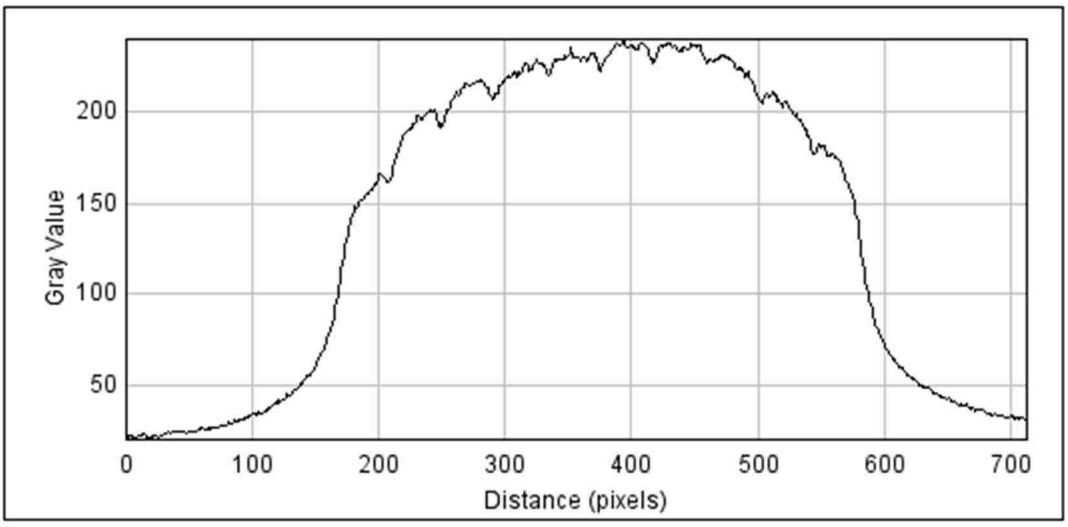

Figure 30. Horizontal signal profile across a row of fibers near the center of the bundle; profile location is marked by the red "»" in Figure 28A.

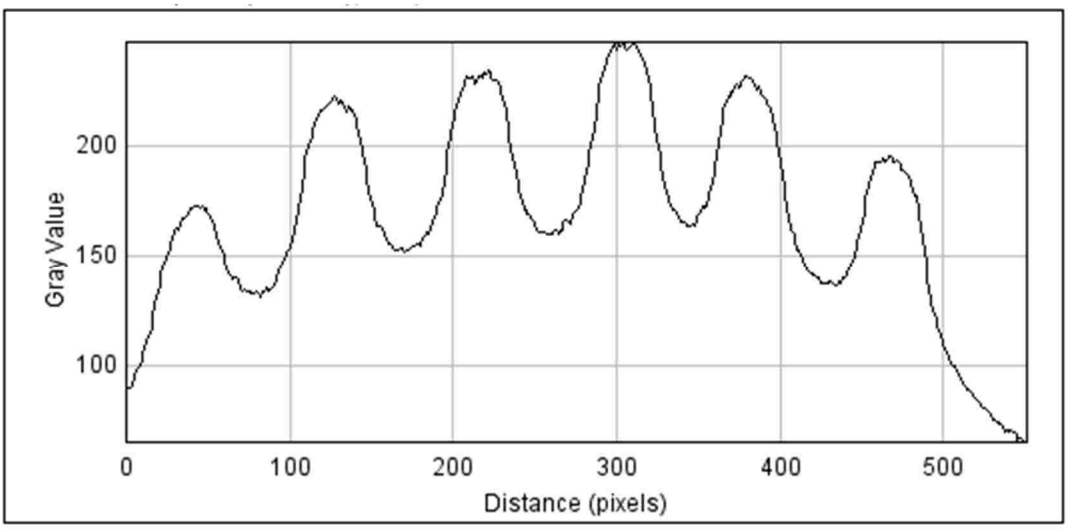

Figure 31. Vertical signal profile near the center of the bundle; profile location is marked by purple "↓" in Figure 28A.

The shape of the light sharing "wash" is clearly visible in Figure 29; this bundling pattern would allow for a simple subtraction based light sharing correction (Figure 32). However, this can only be accurately modeled in the horizontal direction and still does not fully differentiation fiber edges.

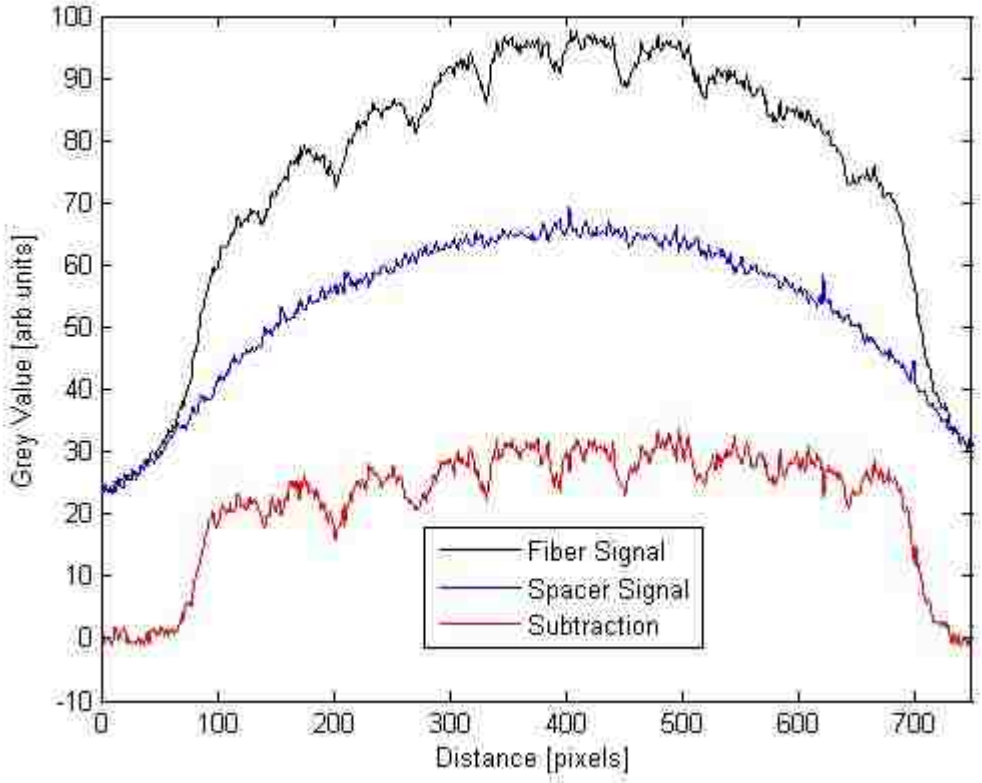

Figure 32. Light sharing correction by subtraction. The profiles for the space and fiber signal are from Figure 29 and Figure 30 respectively.

2.5.2.2. Checkerboard Bundle

This arrangement alternated scintillating fiber with 1 mm x 1 mm spacers to create a checkerboard pattern (Figure 33). The 1-D ribbon in Figure 33A was directly irradiated using the flood acquisition procedure described in section 3.1.1. Figure 33B was acquired using spectrometry acquisition procedure described in 3.1.2. Representative light profiles are shown in Figure 34-Figure 35.

Similar to the vertical profile of the linearly packed bundle (Figure 31), both the horizontal and vertical fiber profiles exhibited less overlap because of the spacers. The signal over the spacers can be used to create a surface representing the light sharing between fibers. This surface can then be subtracted from the fiber signal to correct for this effect. This method is described in Section 3.2. The checkerboard pattern was used for the final assembly of the fiber bundle at the camera.

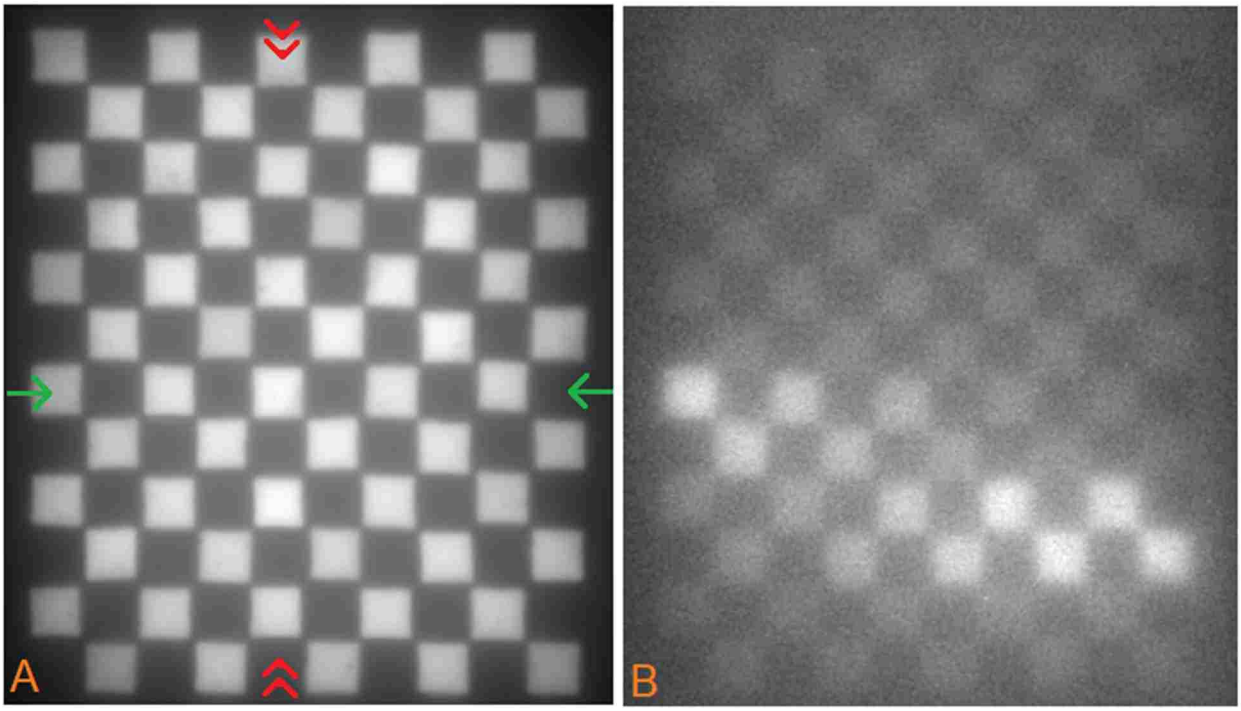

Figure 33. Checkerboard fiber bundle. A) Flood image taken by directly irradiating the 1-D ribbon with a uniform 20 MeV electron beam. The symbols mark the representative profiles in Figure 34 and Figure 35. B) Spectrometer output with the bundle attached to the exit window of the magnet block, and irradiated through the spectrometer with a 20 MeV electron beam.

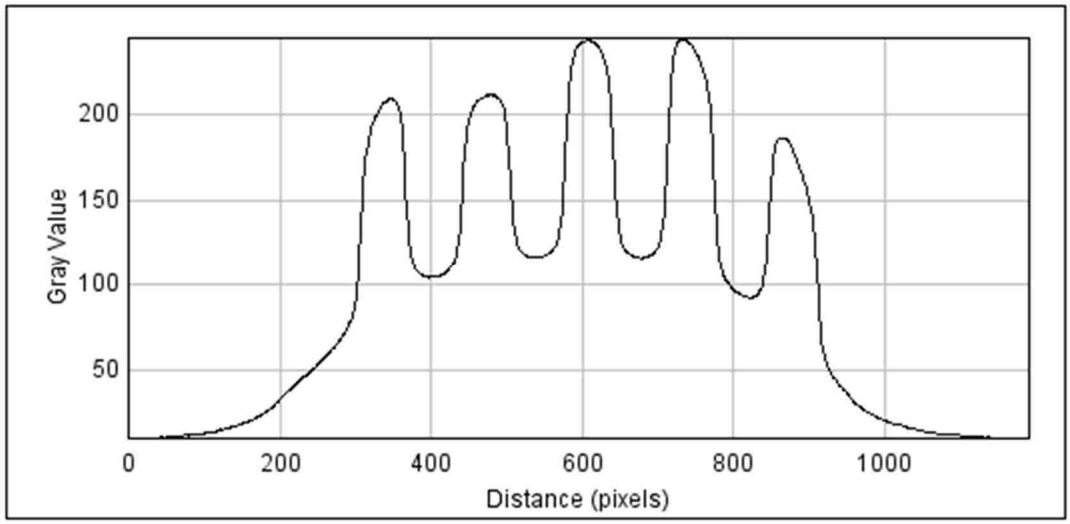

Figure 34. Horizontal signal profile near the center of the bundle across a row of space; profile location is marked by the green "→" in Figure 33A.

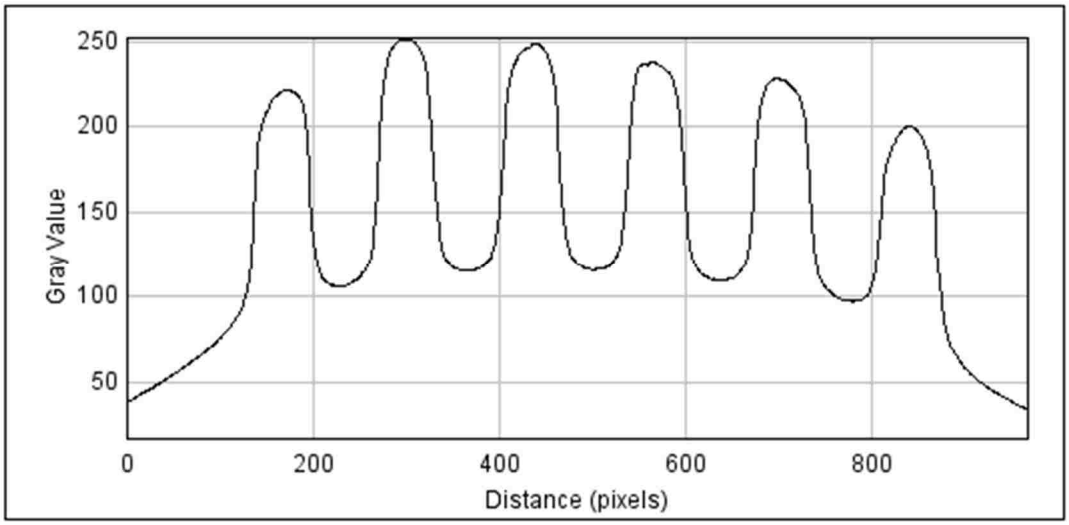

Figure 35. Vertical signal profile near the center of the bundle; profile location is marked by red "»" in Figure 33A.

2.6. Camera Characterization

The camera used in this project was a PixeLINK PL-B955 monochromatic CCD camera (PixeLINK, Gloucester, ON, Canada) with a single lens. The lens (Edmund Optics #65-484, Edmund Optics Inc., Barrington, NJ) was a 25.0 mm diameter, 25.0 mm effective focal length plano-convex lens with a 532 nm laser line coating (<0.25% reflectance at design wavelength). The camera was selected to be predominately sensitive (Figure 36) to the green light emitted

from the scintillating fibers (Figure 20). To facilitate interpretation of the fiber signals, we assessed the camera's performance in terms of focusing, camera acquisition settings, noise, and responsivity. A summary of the camera performance from the datasheet[58] is provided in Table 6 and Figure 36.

2.6.1. Flat-field and Dark-field Corrections

Ideally, if a camera is exposed to a uniform flood field it should produce an image that is uniform and at the correct signal value based on camera responsivity and the spectral quality of the incident light. For most digital camera applications, there are two sources of signal distortions: dark-field noise, and flat-field (pixel gain) variations The dark-field noise is the inherent signal added to all images due to leakage current in the camera pixels. This is measured by acquiring an image with no input light, such that the only recorded values are due to leakage currents. The flat-field measurement is an assessment of the gain variations between individual detector elements. Flat field is measured by collecting an image of a uniform light source. Dark-field noise and flat-field variations are corrected in each acquired image by

$$C = \frac{(R - D)G}{F - D} \tag{2.2}$$

where C is the corrected image, R is the raw image, D is the dark-field image, F is the flood (uniform) image, and G is the average value of (F-D). Typically, one measures dark-field noise and flat-field at each camera setting and brightness level that will be used. The PixeLINK camera and software came with a factory determined flat-field correction (FFC) option.

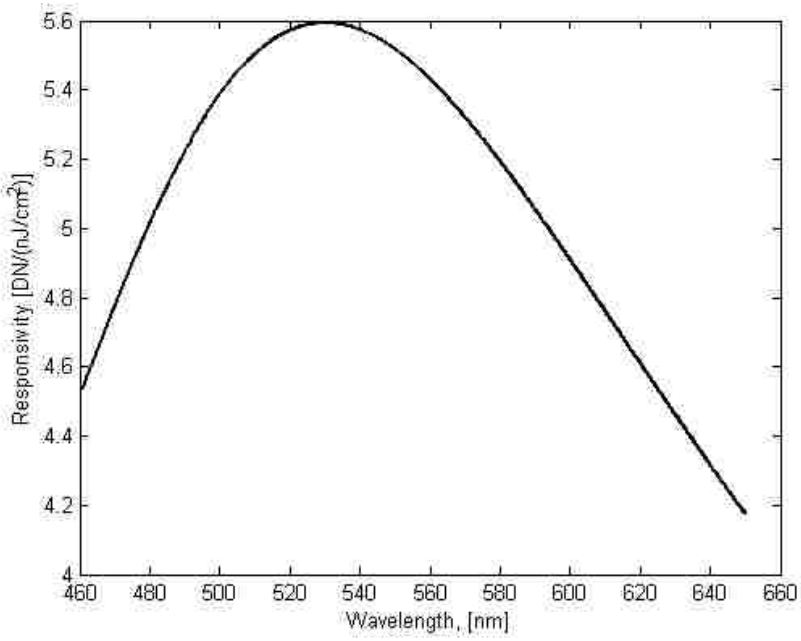

Figure 36. Camera responsivity curve at 0 dB gain, 8-bit data. Modified from PixeLINK[58].

Table 6. Summary of Camera Performance at 40 ms exposure time, 8-bit mode. Modified from PixeLINK[58].

Resolution	1392 (H) x 1040 (V)
Pixel Size	4.65 x 4.65 [μm x μm]
Read Noise	0.23 [DN]
Dynamic Range	60.9 [dB]
Exposure	40 – 10000 [ms]
Gain	0 – 24.57 [dB]

* DN = Digital Number corresponding to 1 bit.

2.6.2. Signal Quantification and Noise

The purpose of the camera was to digitize the fiber light output. The PixeLINK camera records pixel data as digital number (DN), a relative value that must be converted to electron fluence. Light output (number of emitted photons from a fiber) was used as a surrogate for electron fluence through the fiber; these two quantities are linearly related by the physics of electron interactions, scintillating light generator, and light trapping and propagation in the fiber.

The DN value represents a fixed amount of energy deposited in the pixel based on responsivity (DN/(nJ/cm^2)) at a given wavelength. Responsivity (Figure 36) can be recast as

sensitivity (Figure 37), in units of number of photons (N) of a given wavelength that must be absorbed in a pixel to cause a change of 1 DN.

As presented in section 2.4, the fibers emit a spectrum of light (Figure 20). An average, single valued conversion from DN to N, is computed by combining sensitivity with the emission spectrum, give by

$$D = \int \Delta(\lambda)\, p(\lambda) d\lambda \tag{2.3}$$

where D is the conversion factor, Δ(λ) is the camera sensitivity (Figure 37), and p(λ) is the relative emission spectrum (Figure 20).

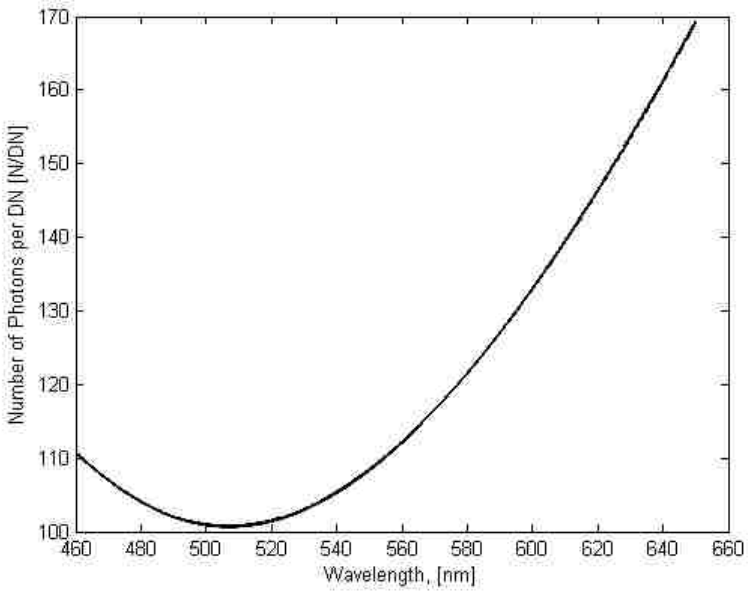

Figure 37. Camera sensitivity, given in number of photons needed per digital number increment.

This yielded a value of D=105.3 [N/DN] at gain = 0 dB, and D=20.9 [N/DN] at gain = 14.04 dB. These conversion factors were used when processing all images to convert the DN of each pixel light output (proportional to electron fluence). Poisson statics were used as the uncertainty for the light output (calculated number of photons).

In addition to Poisson fluctuations, we needed to assess the effect of read noise on the fiber signal. Read noise, or digitization noise is random noise added by the electronics and digitization

process, and results in the camera software misreporting the DN value. As the data sheet reports, this noise is 0.23 DN at 40 ms exposure time and 0 dB gain; this value was not assumed to be constant with exposure or gain.

We illuminated the camera with a flood field and acquired images at multiple exposures, and two different gain settings to assess this effect. We calculated the average pixel value and the standard deviation based on all pixels in the image. We tested four exposure times, 400, 600, 800, and 1000 ms and two gain settings 0 dB and 14.04 dB (linear gain of 5.04).

Table 7. Quantification of Intrinsic Camera Noise. Exposure values are listed along the top.

	400 ms	600 ms	800 ms	1000 ms
0 dB Gain	4.00 ± 0.04 DN	6.00 ± 0.07 DN	7.99 ± 0.09 DN	9.9 ± 0.2 DN
14.04 dB Gain	20.7 ± 0.7 DN	33.6 ± 0.9 DN	39.6 ± 0.9 DN	49 ± 1 DN

The average values scaled as expected based on gain and exposure changes for all tests except 600 ms. The read noise did not scale by the gain. We assumed that these measured values are representative of the behavior of individual pixels. When quantifying fiber signal, we sum over the central region of a fiber (approximately 2000 pixels), and scale the sum by the DN to N conversion factor. Using the number of pixels in a fiber multiplied by the error given above as the intrinsic uncertainty for that fiber vastly overestimates the observed fluctuations in fiber signal. This was because we are more concerned with the average behavior of pixels in the summation region, not the value of individual pixels within the fiber region. The randomly distributed read-noise was effectively averaged out upon summation, becoming negligible.

2.6.3. Camera Operation

The camera was connected by USB to a laptop computer, providing both power to the camera and a data connection for camera control. Image acquisition is controlled by PixeLINK Capture OEM software (Figure 38) running on the laptop. The software controls all settings

related to image acquisition, such as exposure, gain, look-up-table (LUT), image pre-filtering, number of images to acquire, and file type and location. We used a linear LUT and 8-bit bitmap file format; this produced greyscale images with DN values from 0 (black) to 255 (white). While the camera allowed for median pre-filtering during image acquisition, we chose to implement median filtering in MATLAB during our analysis (section 3.1) because it provided better control over the filter size. The factory determined FFC was enabled. We selected an exposure and gain setting to provide adequate signal levels for analysis. Addition details about the using the camera for our spectrometer system are provided in Section 4.4

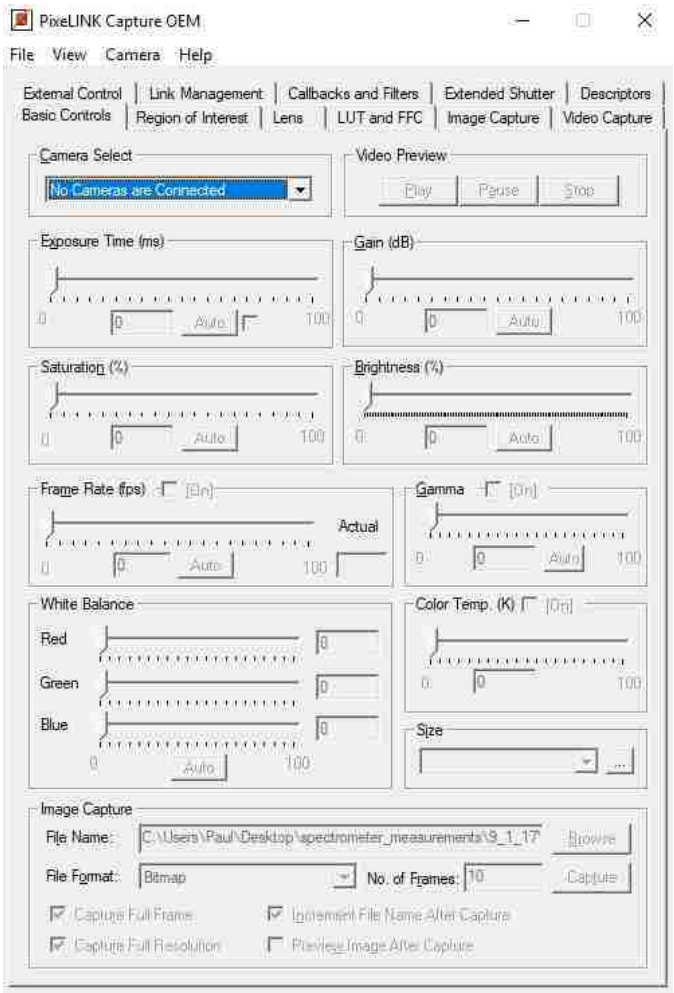

Figure 38. PixeLINK Capture OEM Software used to control the camera acquisition.

2.7. Electron Collimation

Unlike the dual aperture collimator of the passive spectrometer[14,40], the collimation for the real-time version of the spectrometer was a single 6.35 mm diameter circular aperture drilled through the center of a 10 cm x 10 cm Cerrobend insert (Figure 39), thickens 1.6 cm. The Cerrobend aperture was aligned to the steel entrance aperture of the magnet block. A single aperture was used because the scintillating fibers were much less sensitive to radiation as compared to a CR plate. The single aperture increased the electron fluence entering the spectrometer because of its larger size relative to the pinhole used in the passive spectrometer, and its allowance of electrons with an initial angular distribution (i.e. it did not preferentially select only the forward directed electrons). The angular distribution was accounted for during unfolding (section 4.1)

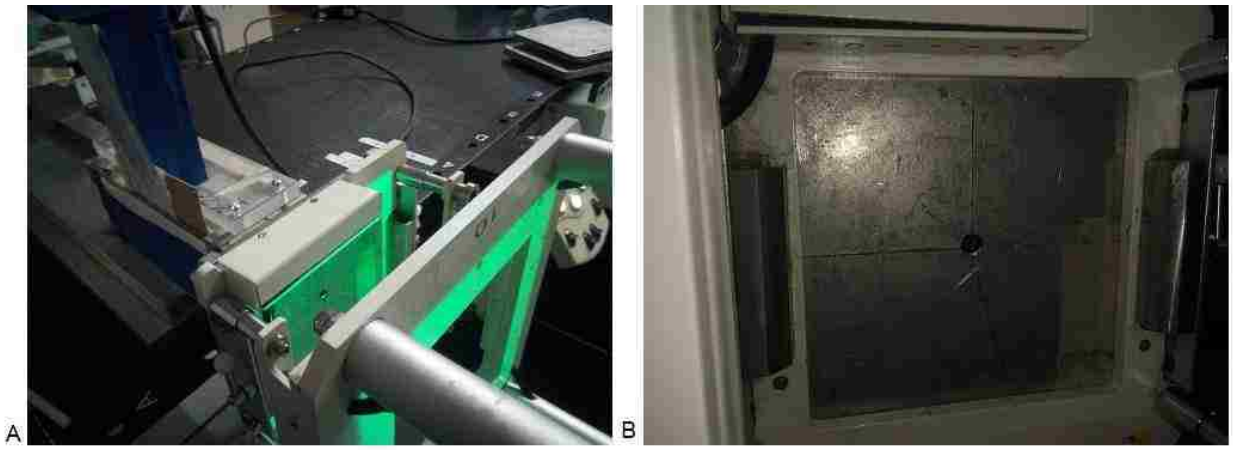

Figure 39. Spectrometer collimation. A is an angled view looking downstream away from the linac head towards the spectrometer. B is a view from within the electron applicator looking towards the 6.35 mm aperture in the Cerrobend insert. For the overall geometry, reference Figure 45.

3. FULL SPECTROMETER SETUP AND CHARACTERIZATION

This chapter describes end-to-end assessment of the spectrometer. In Section 3.1 we provide an overview of the setup geometry, signal acquisition, and signal analysis steps. In later sections, we characterized the interplay between the different components, and how setup variations affect the overall performance of the spectrometer.

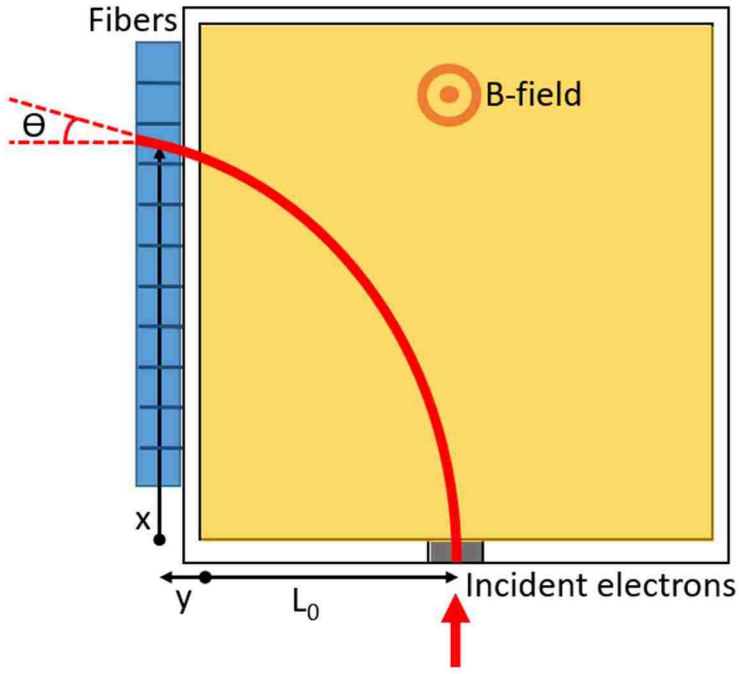

Figure 40. Spatial geometry of the spectrometer. x is the distance along the detector with respect to the physical edge of the magnet block; y is the distance from the physical edge of the magnet block to the center of the detector plane; L_0 is the distance from the physical edge of the magnet block to the center of the entrance aperture; and Θ is the crossing angle of the electrons at the center of the fiber plane. A positive crossing angle is towards the center of rotation (counter clockwise).

3.1. Overview of Spectrometer Setup and Data Acquisition

This section contains the practical aspects of setting up and using the spectrometer. It addresses the flood acquisition used to determine the detector (fiber + camera) response, and the setup process for spectrometry data acquisitions. The camera was controlled using the PixeLINK Capture software (Section 4.4.1); the camera was connected to a laptop computer located outside

the vault next to the linac control console. All image analysis was performed using in-house code written and executed using MATLAB version R2012a (MathWorks Inc., Natick, MA). The linac was controlled in service mode, using the quick beam function. Quick beam allows for the setup and delivery of simple irradiations (no linac gantry or couch movement) at a single energy and dose rate. For all measurements, the linac gantry was rotate to the 9 o'clock position.

3.1.1. Flood Acquisition Setup

After spectrometer assembly, before being able to acquire spectra, we first acquired a flood image to index the fiber positions, size, and response of each fiber. To acquire a flood image, the magnet block was rotated so that the electron beam was directly incident on the fiber ribbon that the exit face of the block (Figure 41). We used a 10 cm x 10 cm Cerrobend insert, thickness 1.6 cm, placed in the 10 cm x 10 cm electron applicator, with a 10 cm x 3 cm rectangular cutout to provide a nearly uniform incident beam that was a similar size to the exit window. The collimator angle was set to -45º. The ribbon was irradiated using a 20 MeV electron beam, and image acquisition parameters of 500 ms exposure time and 14.04 dB gain.

To measure photon contamination from linac head leakage and bremsstrahlung production in the Cerrobend, the insert with the rectangular opening was then replaced with a solid Cerrobend insert; the solid insert blocked the electrons from reaching the fiber ribbon, and the measured signal was used for flood image background subtraction.

The flood image (after flood background subtraction) was used to position the region of interest (ROI) for each fiber. This was achieved by determining the light center of each fiber, then outwardly expanding a rectangle from this point until the edge of the fiber (approximately 50 x 50 pixels), and moving inward 5 pixels to reduce edge effects. The area within each rectangle was considered the active area of the fiber for determining the fiber response. After

indexing, the linear position order was sorted using prior knowledge from the ribbon setup to transform the 2-D fiber image to a 1-D intensity vs position graph.

Figure 41. Setup for flood shot acquisition setup. The spectrometer is rotated 90º from its normal orientation.

The flood image of a uniform input electron fluence was used to determine individual fiber response scaling factors. A correction factor for each fiber corrected for light loss in the fiber due to possible cladding damage or non-uniformities in fiber end polishing by scaling response values to produce a uniform input. This value was calculated after indexing the fibers and correcting for light sharing, and was the inverse of the measured fiber response (Figure 43); it was a multiplicative scaling applied after all other signal corrections (see Section 3.7).

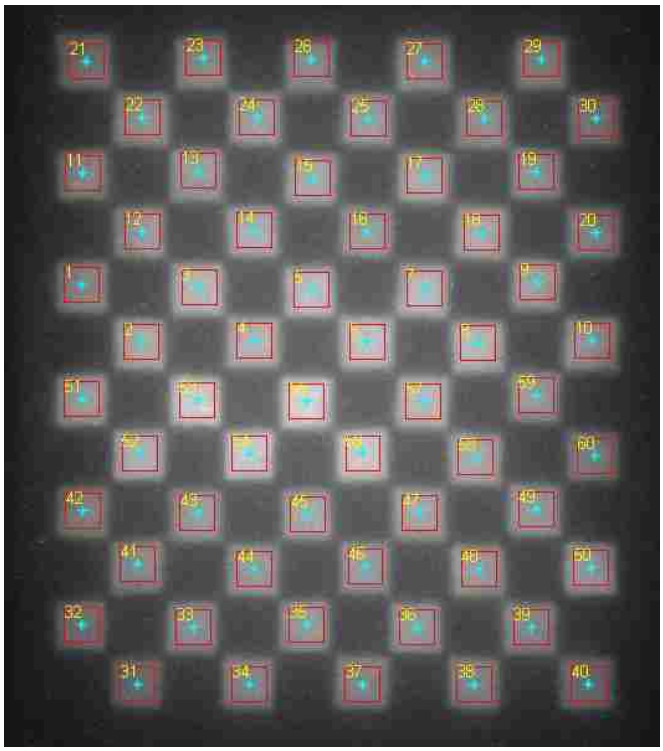

Figure 42. Image of the indexed flood shot. The red rectangles mark the active fiber area; the cyan '*' indicates that center of each fiber; and the numbers indicate what linear order the fibers are in, with "1" being the closest to the entrance aperture.

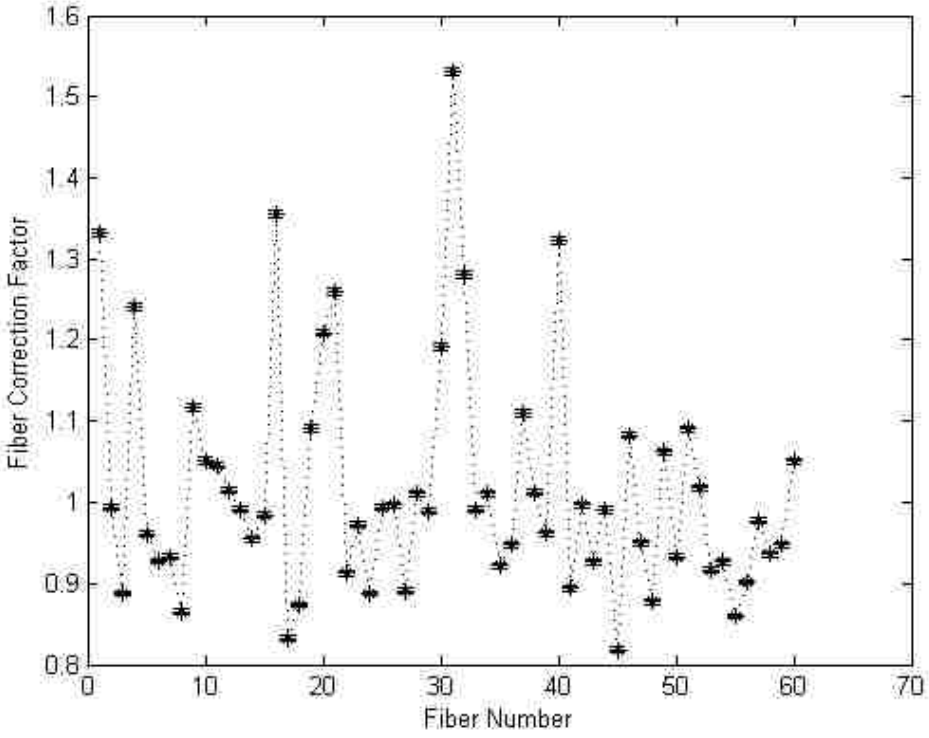

Figure 43. Fiber correction factors used for scaling corrected fiber response.

While it should be only necessary to acquire a new flood image and recompute the fiber centers, fiber bounds and fiber correction coefficients if the hardware was altered, we chose to acquire a new flood each time we used the spectrometer. This was to ensure repeatability and stability of the spectrometer assembly. Over a four month use period, the fiber centers fluctuated $\pm$2.2 pixels in X and $\pm$2.1 pixels in Y. The indexed fiber area did not change (42 pixels by 42 pixels). The fluctuations in the fiber correction coefficients were consistent to within the reported uncertainties.

3.1.2. Acquisition Setup for Spectrometry

This section describes the setup procedure for to acquire spectrometry data suitable for data analysis and processing (Chapter 4). The metal baseplate from the previous, CR-based spectrometer was placed on the treatment couch (0º couch kick), and aligned using the accessory mounting bar (Figure 44). The copper collimator (labeled 3 in Figure 44) from the previous spectrometer, and a pen inserted into a mounting hole (B in Figure 44) was used achieve reproducible setup in the beam-axis direction. The couch was moved in the vertical, longitudinal, and lateral directions using the couch controls to align the entrance aperture of the spectrometer to the central axis of the beam.

The broad electron field produced by the accelerator was collimated by a 10 cm x 10 cm Cerrobend insert placed in the electron applicator (Figure 45). The insert had a 6.35 mm circular hole drilled into the center. The Cerrobend aperture was aligned with the entrance aperture of the magnet block. Reproducible alignment between the two apertures was achieved by using consistent placement on the treatment couch and a 6.35 mm diameter plastic dowel inserted through the Cerrobend insert and into the aperture in the steel on the magnet block (Figure 46). The steel faceplate and the Cerrobend insert brought into contact, forming a single aperture.

After following this setup procedure, the Cerrobend insert with the aperture could be replaced with a solid insert for acquiring spectrometry background measurements. Background measurements were performed at each energy. These background acquisitions are not necessary to perform every time the spectrometer is used because they are mostly stable over time; however we chose to acquire them before each use to ensure accuracy and to continually verify stability.

Figure 44. Spectrometer setup and placement on patient treatment couch. 1 is a metal baseplate; 2 is the accessory mounting bar attached to the couch; 3 is a coper plate mounted to the baseplate; 4 is the spectrometer. A) shows the overall placement on the couch. B) Reproducible setup was achieved in the beam-axis direction by moving the baseplate back to make contact with a pen placed in one of the couch mounting holes.

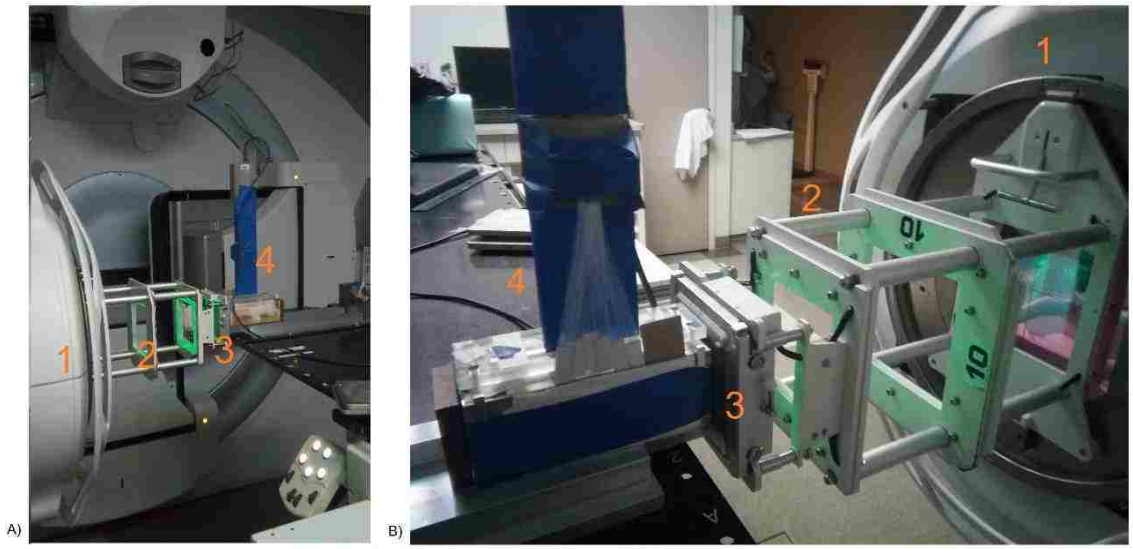

Figure 45. Irradiation Geometry. 1 is the linac gantry; 2 is the electron applicator; 3 is the Cerrobend insert; 4 is the spectrometer. View A is looking towards the linac; view B is looking away from the linac.

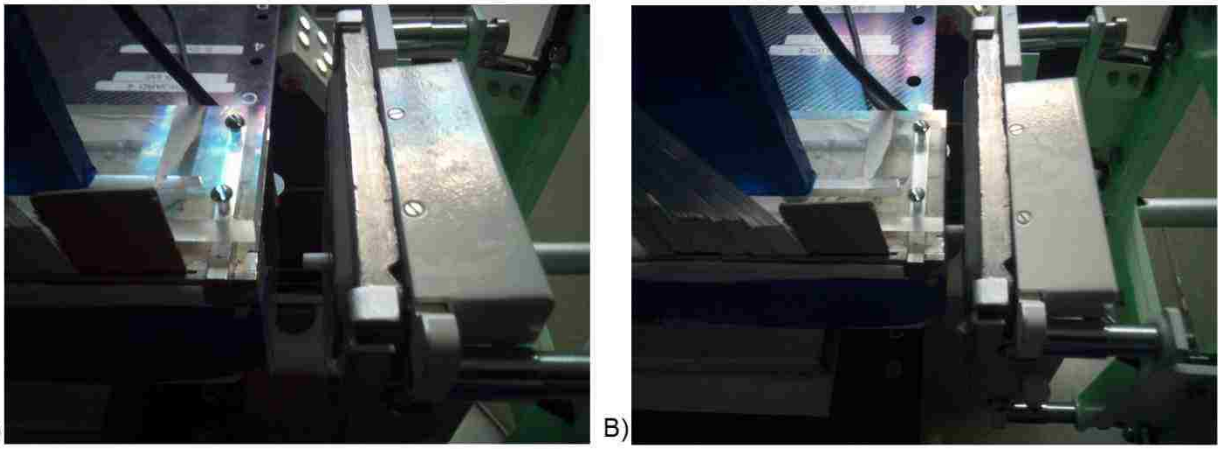

Figure 46. Aperture alignment using a plastic dowel. A) The plastic dowel is protruding from the Cerrobend insert. B) The dowel is providing partial docking between the Cerrobend aperture and the steel entrance aperture to the spectrometer.

3.1.3. Data Acquisition and Processing

The camera acquired images of the fiber bundle with an exposure time of 1000 ms and a 14.04 dB gain. These settings allowed for adequate signal accumulation while still allowing for near real-time data acquisition. All images were median filtered to remove salt and pepper noise that resulted from back pixels and the camera operating in a noisy RF environment.

One of two spectrometry backgrounds was used for the initial background subtraction: a current-setup background (described in section 3.1.2), or an average (reference) background for each energy. Reference background curves were produced by averaging 100 background images during a single setup. The user can choose to have the software use the reference background, or check for a current-setup background, and use it if it was statistically significantly different than the reference ($p=0.32$). The background was scaled so the ratio of the total signal from the spectrometry acquisition to the total signal from the blocked, background image was the same for each run at a given energy (see Section 3.5.1); this reduces the effect of dose rate fluctuations between the background signal and the beam-on signal. This background scaling factor was conservative, meaning we did not attempt to subtract all of the background signal during this

initial step; this was done to ensure we were not aggressively setting the signal in the low-energy tail section to 0, allowing for more accurate fitting.

After spectrometry image acquisition and initial background subtraction (example shown in Figure 47), the first step in the analysis was summing the pixel (DN) values within the ROI of each fiber. Total DN values for each ROI were multiplied by 20.91 (Section 2.6.2) to covert to the number of scintillation photons within the ROI. Next, the raw signal was corrected for light sharing and fiber sensitivity variations, resulting in a fiber signals like that shown in Figure 47. Both the background signal and the signal from the open pinhole were corrected for light sharing effects (Section 3.2).

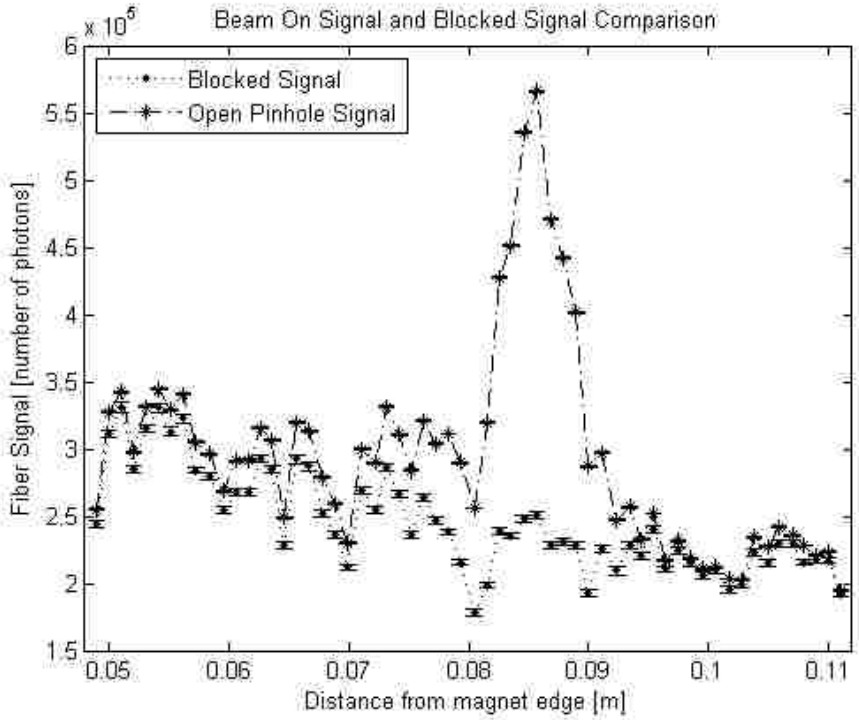

Figure 47. Example of fiber signal and background, after light sharing correction, for a 13 MeV beam.

The last correction was a residual background subtraction that resulted from our conservative initial background subtraction. For all beam energies other than 20 MeV, there were fibers past the peak that contained only residual background noise. These residual background value was

determined as the mean of the values beyond the first zero crossing in the first derivative of the fiber signal (Figure 48). The mean value was subtracted from all signals; both the original residual background values and any values less than zero were set to zero.

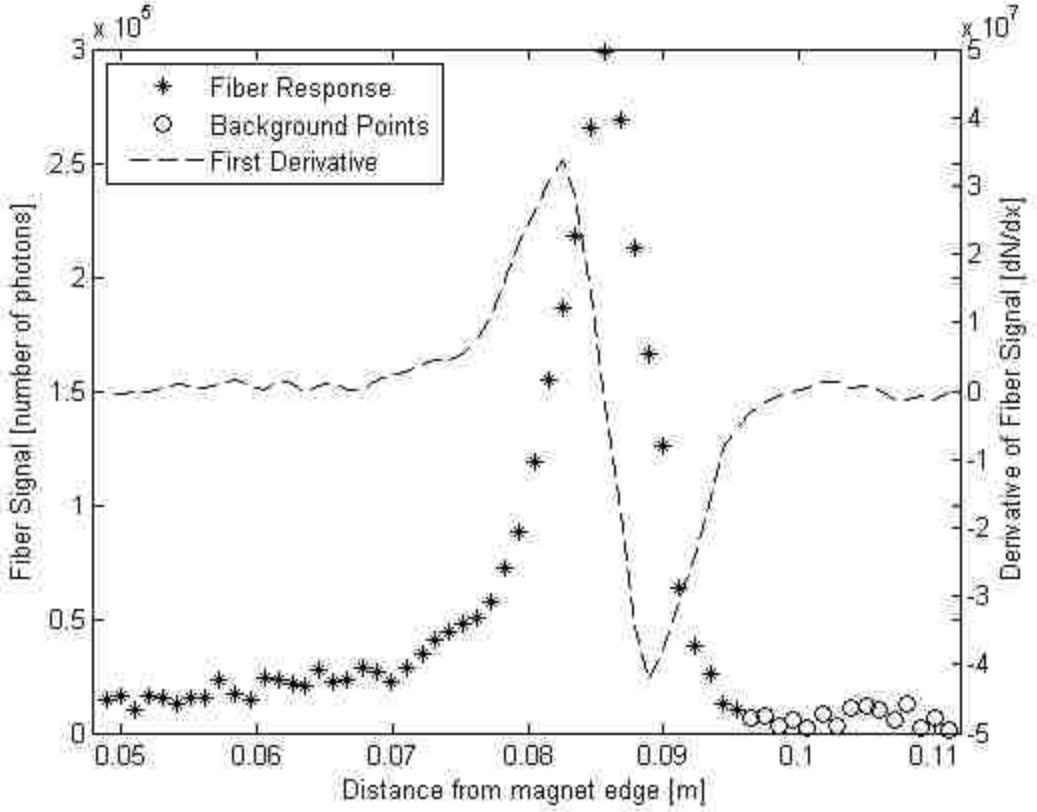

Figure 48. Determination of additional residual background signal. The background points are the fiber signal values past the zero-crossing of the first derivative to the right of the main peak.

This corrected fiber response, Figure 49, was unfolded into the energy spectrum for the incident electron beam (Chapter 4).

3.2. Light Sharing Effect Correction

As show in section 2.4.1, the light from a fiber was not limited to the physical boundaries of the fiber, and instead spreads to nearby areas. The checkerboard bundle arrangement allowed correction for light sharing effects by modeling the surface defined by signals in the inter-fiber

regions (Figure 50). The spacers between fibers do not produce signal, therefore any apparent signal is the result of light spread from nearby fibers. First, we generated a set of ROIs in the blank areas that were matched to the fiber size, as to not introduce bias.

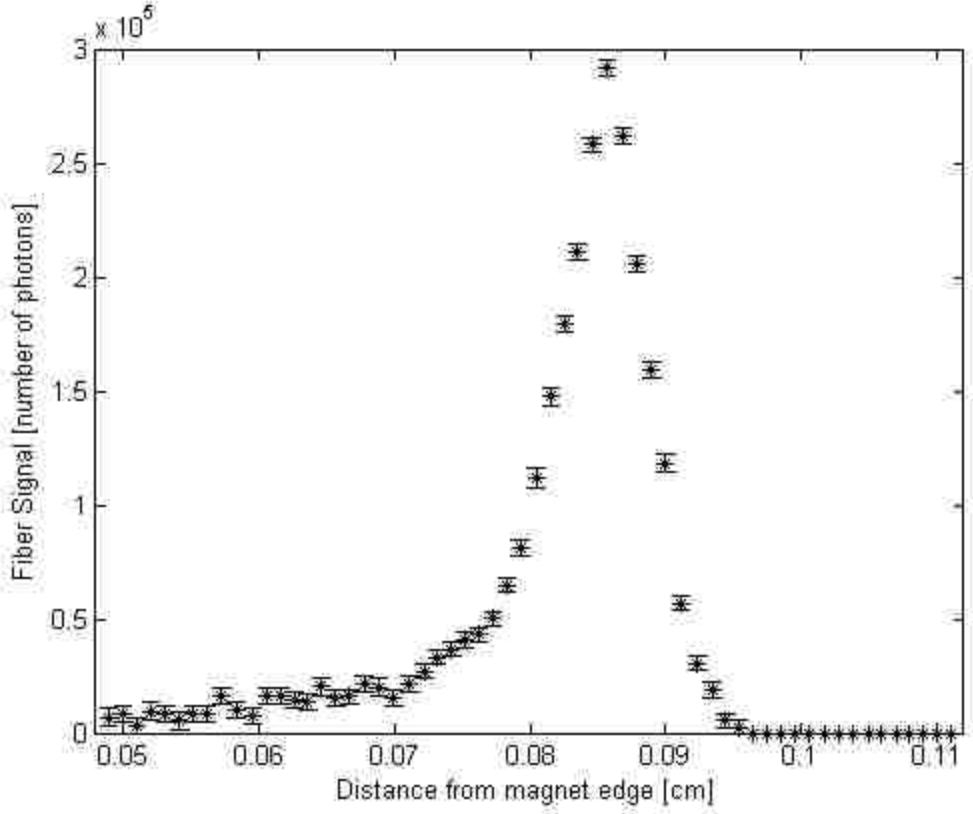

Figure 49. Fully corrected fiber signal for nominal beam energy of 13 MeV. The error bars depict the 1-sigma uncertainty bounds for each data point.

Next, we summed over these ROIs, and fit a surface to these points. (Figure 51). The surface values at the locations of the fiber centers were subtracted from the measured fiber signal (Figure 52). The single surface values at the fiber centers were accurate to within 0.1% compared to summing over same surface areas as the actual fiber areas. We used the single surface value for subtraction because it was accurate and computationally quicker.

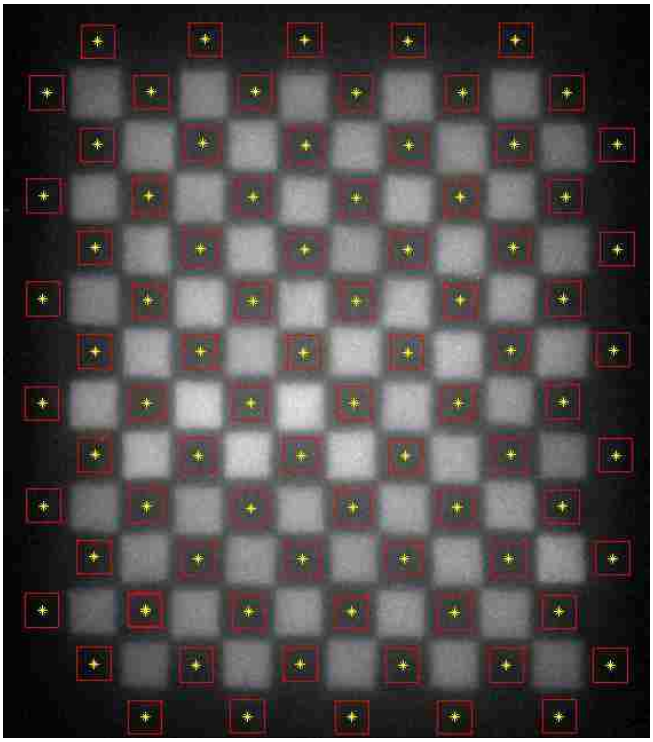

Figure 50. Blank bounds for fiber spacers (red), and the centers of spacers (yellow *).

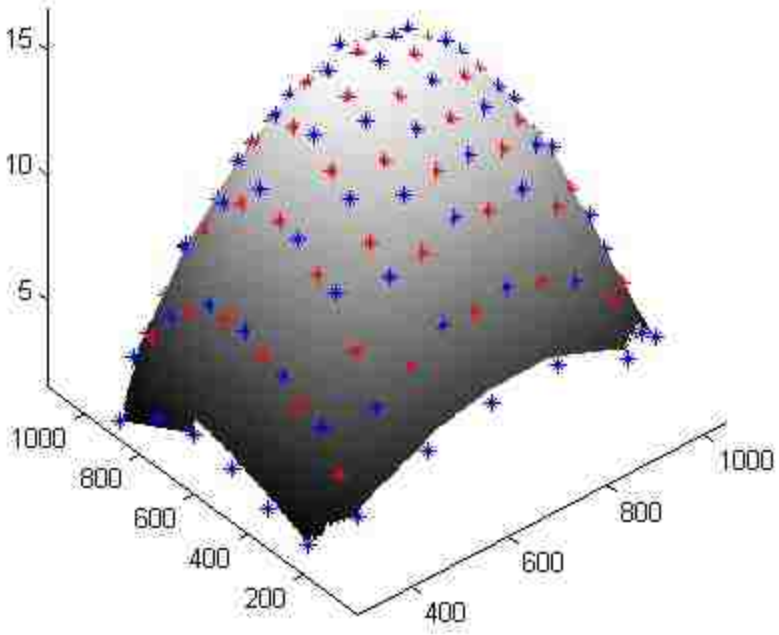

Figure 51. Surface fit to blank response (blue *). The red asterisks are the fiber centers.

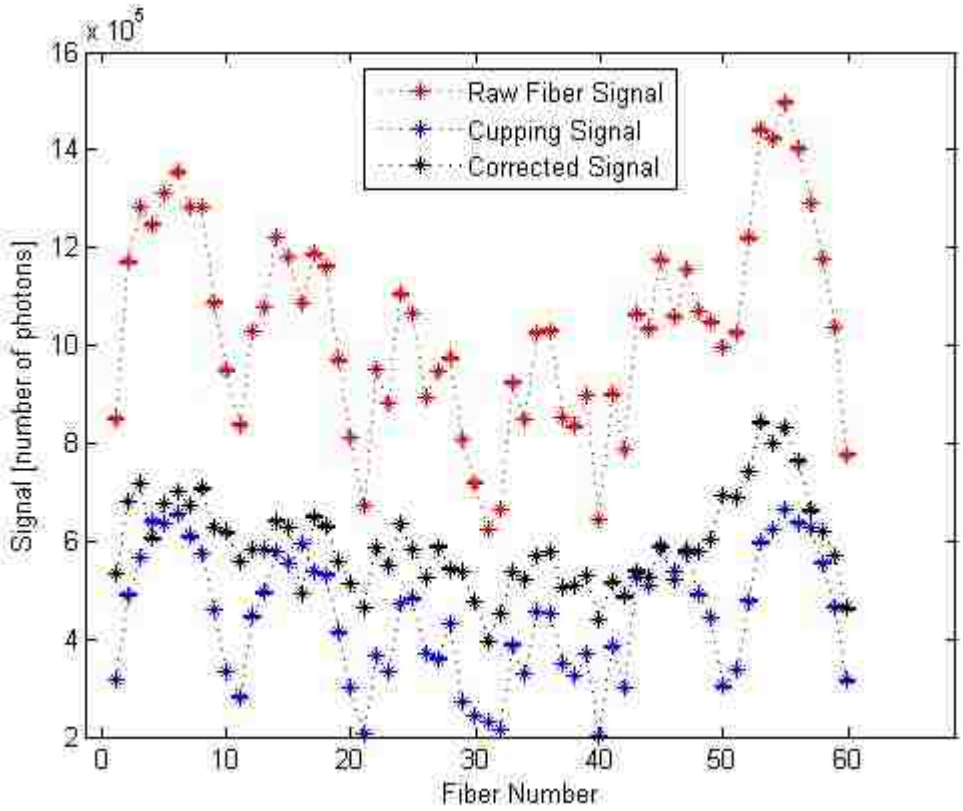

Figure 52. Effect of light sharing correction. Raw fiber signal does not include any corrections, including background subtraction. The dotted connecting lines are to improve clarity.

3.3. Effect of Camera Focus on Fiber Indexing and Signal Correction

To characterize the effect of the fiber and camera optics on fiber signal, calculated fiber ROIs, and light spread at different focal lengths, we shifted the camera vertically and calculated the fiber correction factors using the method discussed in Section 3.1.1. The fiber correction factors were an appropriate metric to use for performance assessment, because they depend on the entire detector (fiber + camera) system. A large change in the correction factor means there is a large change in one of the dependent quantities, possibly indicating poor stability of the analysis and correction methods.

We shifted the camera vertically between 12 cm and 13.5 cm (lens to bundle distance), in 1 mm steps; we did not perform any other setup changes, or move the spectrometer between settings. The results are summarized in Figure 53.

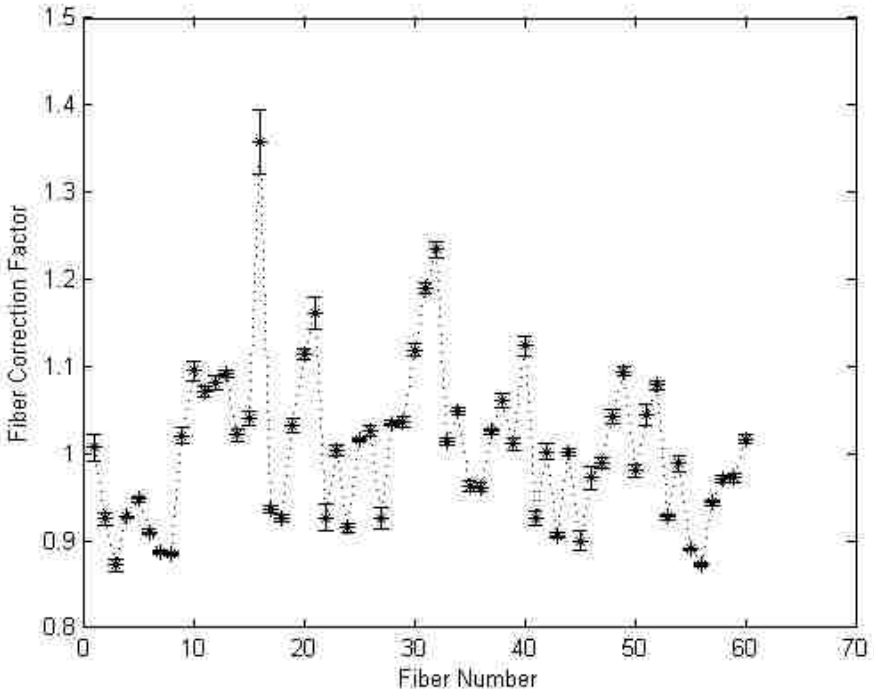

Figure 53. Average fiber correction factors for lens-bundle distances of 12 cm to 13.5 cm. Error bars represent one standard deviation. The dotted connecting lines are to improve clarity.

Aside from fiber number 16, all fibers showed only a small (<1.5%) variation in their correction factors, with an average of 0.7%. Upon inspection of the bundle, fiber 16 was determined to have damaged cladding and was slightly recessed within the fiber bundle. This altered the light spread behavior, and contributed to the high variability in the fiber correction factor. Stability of the fiber correction factors suggested the robustness of the correction method. A final vertical setting 13.0 cm was used for all future studies. We did not attempt to reposition or replace fiber 16 because its poor performance for a single setting (i.e. 13.0 cm) could be satisfactorily corrected.

3.4. Assessment of Spectrometer Setup Variation

In this section, we investigated the setup reproducibility, and the effect of collimator alignment with the entrance aperture of the magnet block.

3.4.1. Setup Reproducibility

The spectrometer was setup three times using the same procedure (see section 3.1.2), and full set of beam measurements (both background and spectrometry images, all 7 energies) was acquired for each setup. Between each setup, the spectrometer was removed from the treatment couch, the linac and couch were returned to their default positions, and all additional positioning equipment was removed. Representative results for partially corrected signals (background subtraction without dose rate correction, fiber correction factor, and light sharing correction) are shown in Figure 54.

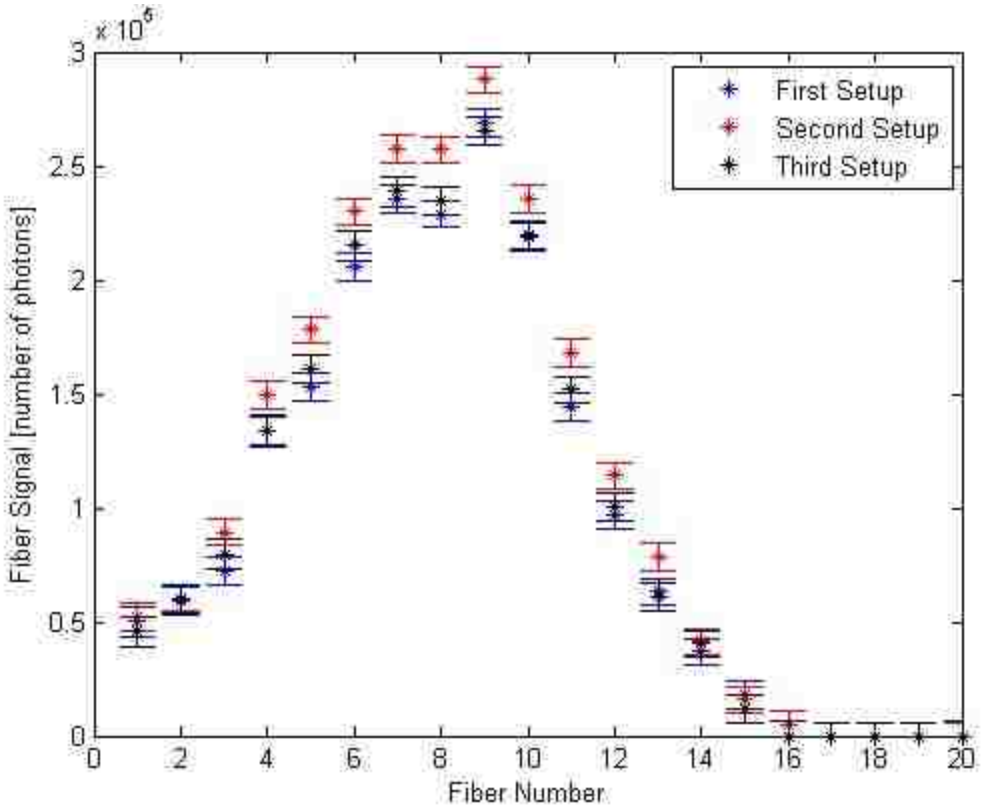

Figure 54. Assessment of setup variability for a 7 MeV beam.

The results showed variations that are consistent within the uncertainties of the individual data points and the fluctuations in linac output behavior. We concluded that we have a robust setup procedure.

3.4.2. Aperture Mismatch Assessment

To investigate the effect of aperture mismatch, we aligned the two apertures using the method in 3.1.2, and then introduced known shifts using the treatment couch. We shifted the spectrometer by 1 mm and 2 mm in both the lateral and vertical directions, as well as diagonally with 1 mm shifts simultaneously in both directions. Because of symmetry in the measurement locations, the results for only two representative shifts are shown in Figure 55.

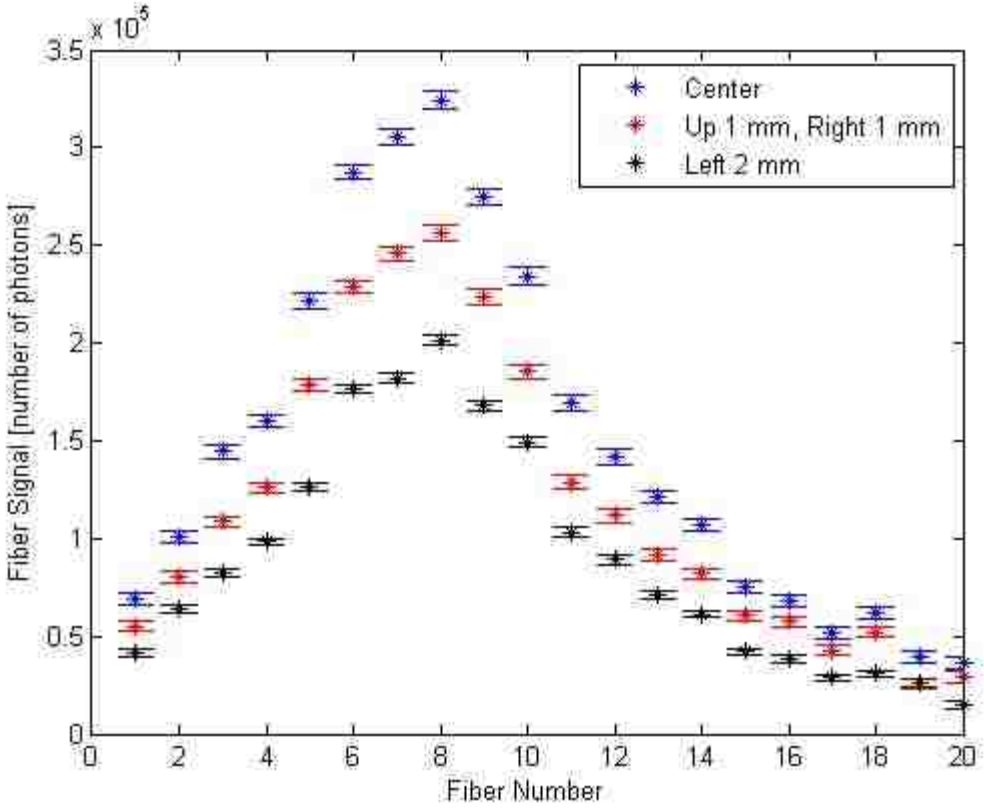

Figure 55. Effect of Cerrobend and steel aperture mismatch. Center indicates the two apertures are coaxial.

Vertical shifts reduce the effective size of the entrance aperture to the spectrometer, and therefore only reduce the total signal amplitude. This is due to a reduction in the total electron fluence entering the spectrometer. The signal reduction can be corrected for by signal renormalization/rescaling (Figure 56). Horizontal shifts modify the effective aperture size, as

well as introduce a small shift to the effective center (indicated by L_0 in Figure 40) of the aperture. This shift is equivalent to half of magnitude of the horizontal misalignment. At 2 mm (1 mm effective), this shift did not alter the shape of the signal distribution to a degree in excess of the measured signal uncertainties.

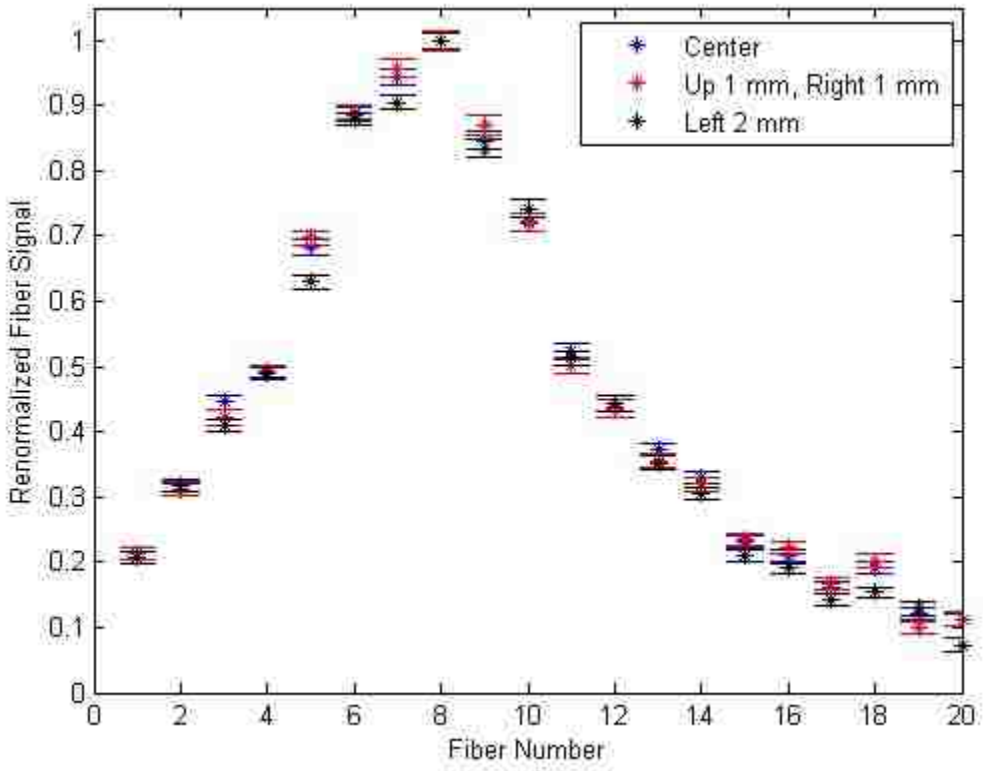

Figure 56. Fiber signals, after renormalization to the max value, under mismatched aperture conditions.

3.5. Sensitivity to Linac Output Rate Variations

The real-time spectrometer acquires data by integrating over 1000 ms intervals. The total signal in an interval is proportional to the integrated output of the linac over the interval. The linac output rate can vary by several percent over the duration of an irradiation. Additionally, not all beams exhibit the same output rate stability or temporal variation pattern. The real-time spectrometer was sensitive enough to measure these output rate fluctuations.

To assess this output rate sensitivity, we acquired 100 sequential spectrometry and 100 background measurements, at a 1000 ms exposure time, for each available electron energy. The total measured signal was calculated as the sum of all fiber signal values (representative data shown in Figure 57). The linac software's service graphing tools provided a real-time graph of the output rate, sampled at 4 Hz. Unfortunately, the service graphing data is only visually displayed and cannot be exported for further analysis. This prevented us from quantitatively assessing the agreement between the measured and reported data; however we can still qualitatively compare the two.

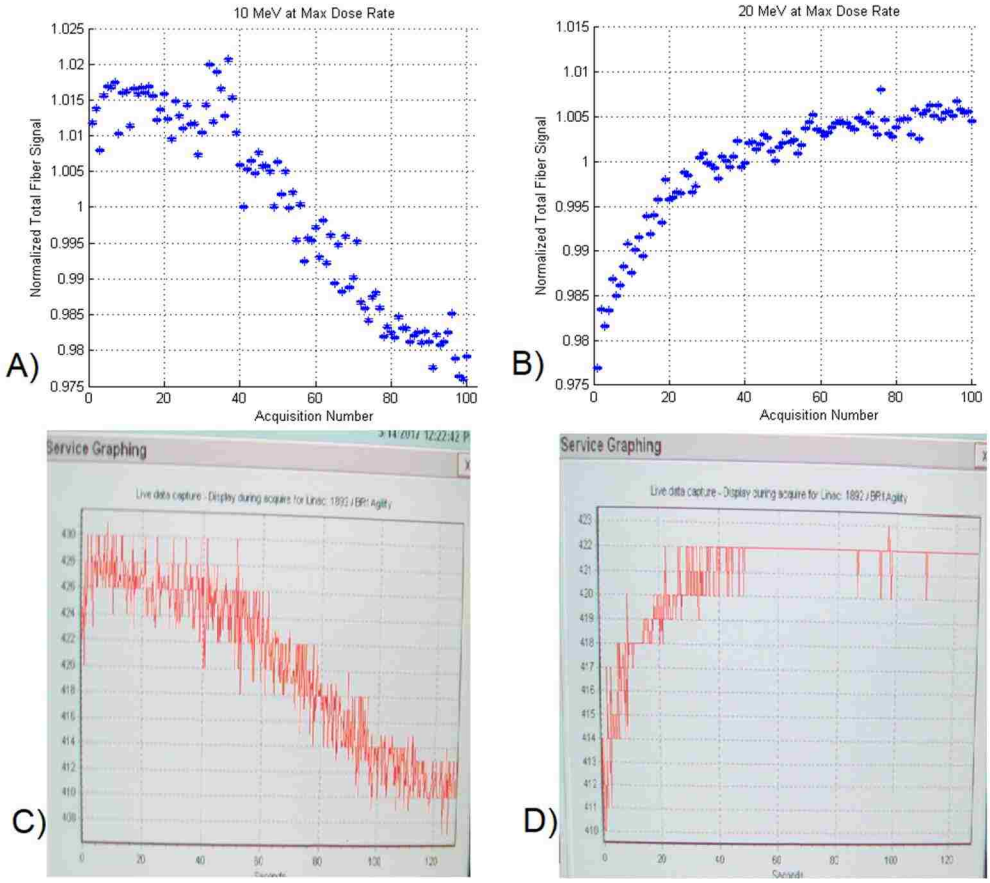

Figure 57. Comparison between measured total fiber signal in 1000 ms acquisitions to output rate as reported by the service graphing function of the linac control software. A and B are total fiber signals the 100 spectrometry acquisitions for 10 and 20 MeV, respectively. C and D are photographs of the service graphing report from the linac control software for the 10 and 20 MeV beams, respectively.

For the 10 MeV acquisitions, the average of the measured data from the spectrometer was approximately at the middle acquisition (~50); this corresponds to around the 65 s mark in the linac data, indicating two things: 1) due to disk write times and OS overhead, setting the camera for 1000 ms exposure and continuous acquisition does not result in acquisitions every 1000 ms, instead giving an effective readout of 0.77 Hz; 2) the average value from the service data is approximately 420 MU/min. The maximum reported value of ~428 MU/min is an increase of 1.9% above the average, and the minimum reported value of ~410 is a decrease of 2.4%. This range was consistent with the measured spread from the renormalized spectrometer data, ~1.75% increase, and ~2.5% decrease. This indicated that the spectrometer is sensitive to output rate measurements. For the 20 MeV beam, we acquired 100, 1000 ms frames in ~128 s, giving an effective acquisition rate of 0.77 Hz. The measured variation range was ~2.5%, which is consistent with the range reported by the service graphing software. The next section addresses how we corrected for this fluctuation.

3.5.1. Dose Rate Correction in Background Measurements

A key step in the fiber signal analysis chain was the initial background subtraction. As we discussed in the Section 3.1.3, the background measurements were acquired separately from the spectrometry data acquisition, with the assumption that the linac was performing consistently between background and data runs. However, as shown in the previous section, the spectrometer is sensitive to output rate fluctuations. Assuming a constant output dose rate can introduce errors up to 5% in the fiber signal values, as shown in Figure 57.

To correct for dose rate variation between background measurements and spectrometry data acquisition measurements, we acquired 100 images for both background, and spectrometry runs, while tracking the reported output rate using the two methods in the previous section. After data

acquisition, we matched background and spectrometry images taken at approximately the same dose rates, and determined the average ratio between the total fiber signal for a spectrometry acquisition to the total fiber signal for the background acquisition at the proper output rate. This procedure was repeated for all energies. This produced energy specific spectrometry to background ratios (Table 8) that were used to rescale the backgrounds before subtraction for all subsequent uses of the spectrometer.

Table 8. Spectrometry to Background Ratios for Background Renormalization

Energy [MeV]	7	9	10	11	13	16	20
Ratio	1.223 ± 0.006	1.212 ± 0.007	1.27 ± 0.04	1.225 ± 0.005	1.216 ± 0.007	1.188 ± 0.004	1.12 ± 0.01

3.6. Effect of Beam Energy on Fiber Correction Values and Background Response

This spectrometer is designed to assist in beam tuning and matching. As such, it needs to stably operate even when the accelerator is detuned or producing an energy that may be several MeV from its nominal value. To assess the effect of energy change on the spectrometer operation, we characterized the fiber correction factors and the structure of the measured background response at different nominal beam energies.

3.6.1. Energy Dependence of Fiber Correction Factors

We acquired flood images at the seven available energies, and compared fiber correction factors (Section 3.1.1). The results are shown in Figure 58. The percent standard deviation of the correction factors due to energy change was between 0.1-0.9%, with a mean value of 0.4%. This indicated minimal energy dependence of the fiber correction factors.

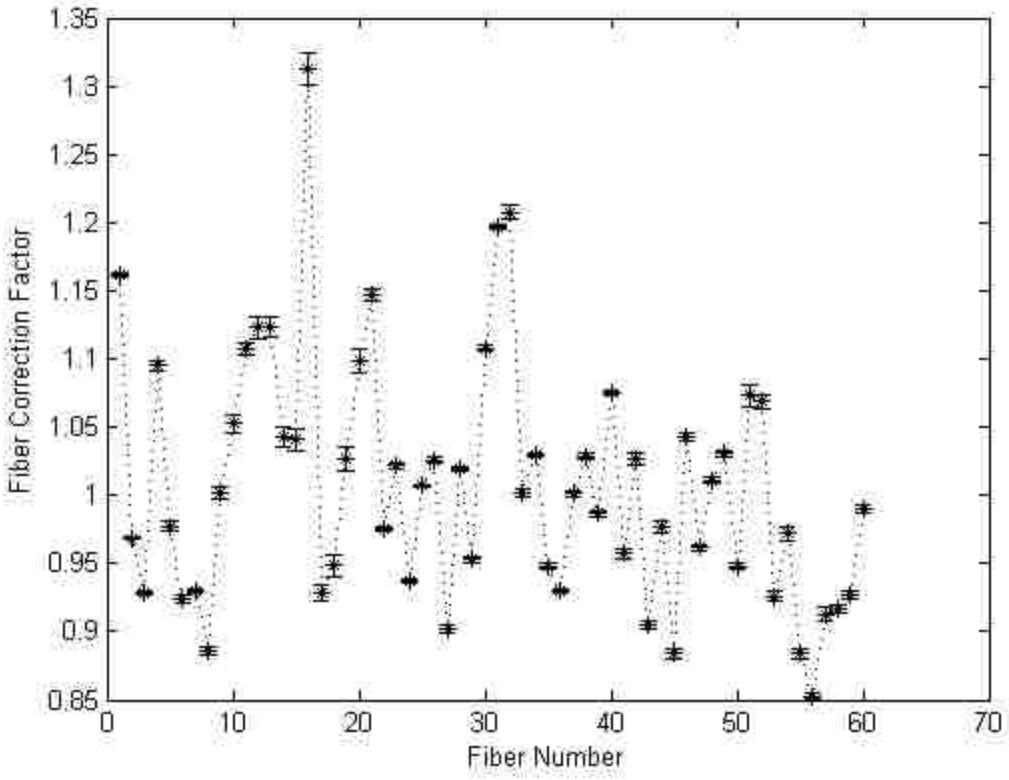

Figure 58. Energy dependence for fiber correction factor. The average value for each fiber across all energies and the standard deviation resulting from energy change are plotted. The dotted connecting lines are to improve clarity.

3.6.2. Energy Dependence of Background Response

Using a background acquired at a nominal energy as the appropriate background for a detuned energy requires that the background must either be constant in energy, or slowly varying about that energy. To determine the energy dependence on background measurements, we acquired background images at the seven available energies, and then computed the background response renormalized by their mean values. We performed renormalization because the absolute magnitude of the background changes with machine output variations and energy, as bremsstrahlung production scales as energy squared. The results are summarized in Figure 59.

The percent standard deviation of the background response due to energy change was between 0.2-5.5%, with an mean value of 1.5%. Most fibers did not exhibit a strong variation with energy, though several did (e.g. 21, 50-53). For these widely varying fibers, we investigated

if the second criteria, slowly varying with energy, was met. Figure 60 shows the variability with energy of the measured signal in fiber 21, which exhibited the largest variance; over a small (~1 MeV) range about any nominal energy, the expected variance in fiber signal should be <2%.

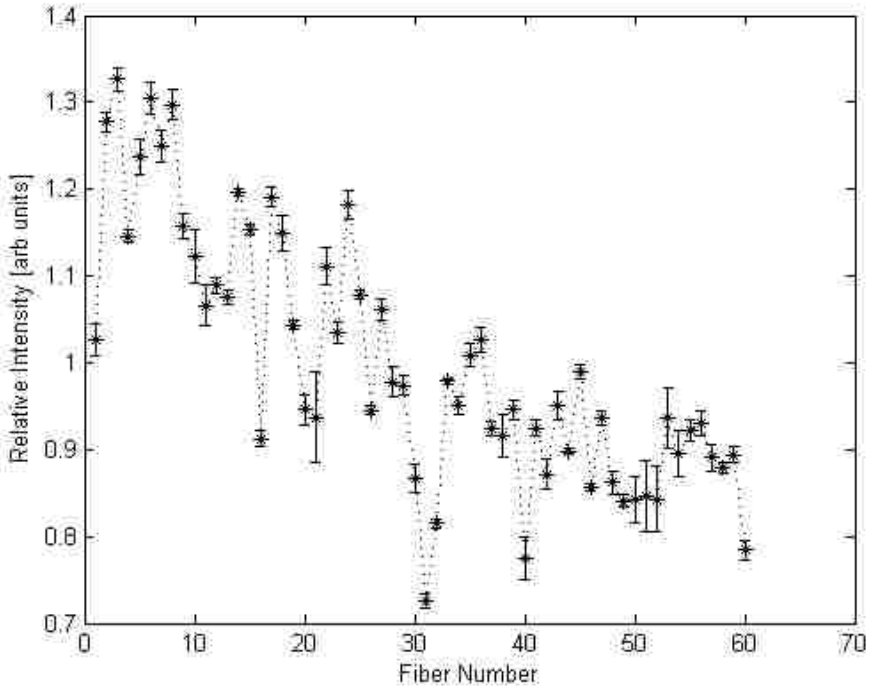

Figure 59. Energy dependence of the background response. The average value for each fiber and the standard deviation of the values are plotted. The dotted connecting lines are to improve clarity.

The other highly energy dependent fibers also exhibited a similar, slowly varying energy dependence. Therefore, we concluded that it was appropriate to use the background for the nominal beam energy when detuning by increasing the uncertainty in the background signal by the worst case 2% added in quadrature to the other uncertainties.

3.7. Final Signal Correction Chain and Error Sources

The equation that converts the raw fiber signal to the final corrected fiber signal is

$$R_C = s_{fib}[(R_{raw,spect} - R_{sharing,spect}) - s_{bkgd}(R_{raw,bkgd} - R_{sharing,bkgd})] - R_{resid} \quad (3.1)$$

where R_c is the corrected fiber signal; s_{fib} is the fiber correction factor determined by the flood shot; $R_{raw,spect}$ is the uncorrected fiber signal for a spectrometry acquisition; $R_{sharing,spect}$ is the light sharing signal for the spectrometry image; s_{bkgd} is the background scaling ratio for output rate corrections; $R_{raw,bkgd}$ is the raw background signal; $R_{sharing,bkgd}$ is the light sharing signal for the background image; and R_{resid} is the residual background subtraction. Each of these quantities has an associated uncertainty which were propagated accounting for correlations where appropriate (e.g. light sharing subtraction). The fully corrected fiber signal R_c was then unfolded into the energy spectrum. The unfolding method is addressed in the next chapter.

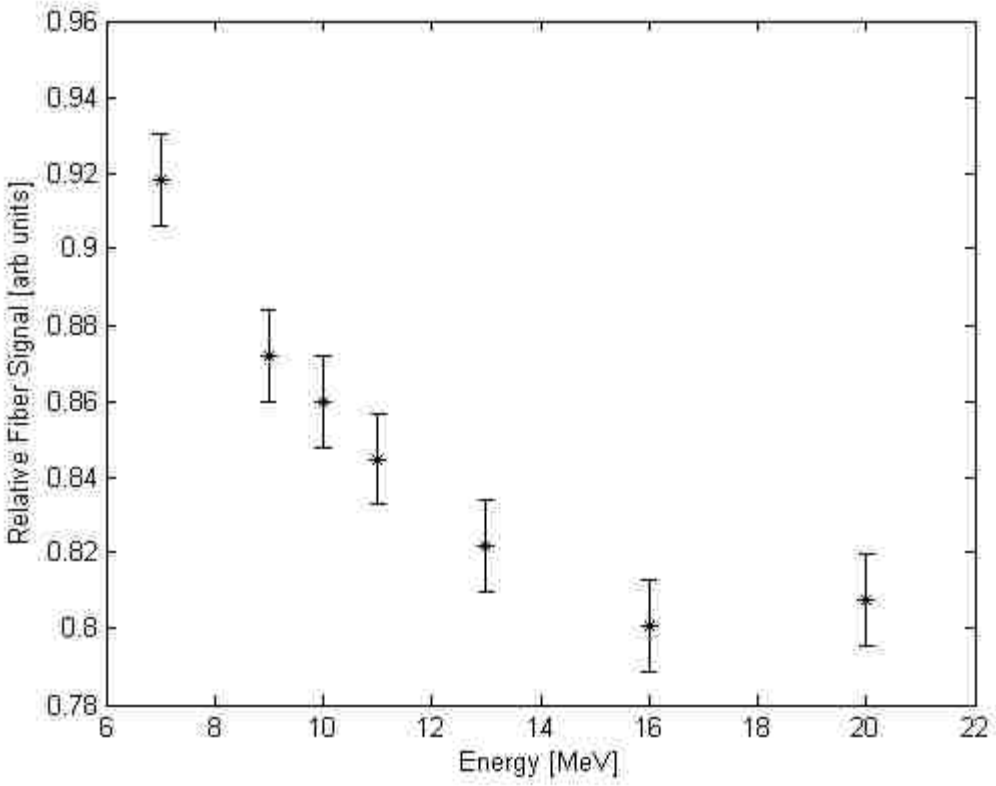

Figure 60. Fiber 21 background variations with energy. Measured background and one standard deviation uncertainty are plotted.

4. DEVELOPMENT AND CHARACTERIZATION OF THE SPECTRAL UNFOLDING SOFTWARE

The goal of the spectral unfolding software was to transform the fiber signal into the electron energy spectrum. An additional feature implemented in the software for convenience was generating a PDD curve from the reconstructed spectrum.

4.1. Energy Spectrum Unfolding Method Overview

A precomputed detector response function (DRF) matrix facilitated the rapid unfolding of the energy spectrum from the fiber signals. The DRF was determined using a simplified physics model of the spectrometer. The model accounted for:

- the angular distribution ($\sigma_{\theta x}$) of electrons due to in-air scatter, based on the method of Werner et al [59];
- the finite of the fibers with a range of electron incidence angles crossing path lengths;
- the inhomogeneous magnetic field within the magnet block;
- collisional stopping power variations at different energies.
- finite sized input aperture

As mentioned in section 2.2.1, we used COMSOL to model the magnetic field. Because Werner's equation only provides $\sigma_{\theta x}$ at a distance of 95 cm from the source, we estimated the additional in-air scatter within the spectrometer by scaling $\sigma_{\theta x}$ according to the method in ICRU 35 [5], where $\sigma_{\theta x}^2$ scales linearly with distance. The additional in-air distances for each energy was computed by propagating a forward-directed electron at the center of the aperture to the detector plane defined as the mid-depth of the fibers.

Simplifying assumptions included constant fluence within the entrance aperture, no magnetic field inhomogeneity or dispersion in the direction parallel to the fibers, and no electrons scattering in the fibers.

Due to our magnetic field and physics model, we were unable to construct a simple analytic formula relating the energy (E), initial angle (θ_i), and starting position (x) of an electron entering the aperture to its final position (y) and crossing angle (θ_f) at the midline of the detector plane. Instead we uniformly sampled electron initial conditions across the 100 aperture starting positions, 221 energies, and 100 initial angles out to $3\sigma_{\theta x}$, and propagated the electrons through the magnet block to the detector plane by performing a time-stepped solution of the kinematics equation and the Lorentz force. Least-squares fits to the sampled data were used to create a mapping function *M* that output the position and angle an electron crosses the midline of the fiber plane when given the initial condition. That is

$$M : (E, x, \theta_i) \rightarrow (y, \theta_f) \tag{4.1}$$

The *DRF(E,x,y,θ)* is now given by

$$DRF(E, x, y, \theta) = \left(S \big/ \rho \right) W(x, \theta_i) P(y, \theta_f) \Big|_{M:(E,x,\theta_i)\rightarrow(y,\theta_f)} \tag{4.2}$$

where *(S/ρ)* was mass collisional stopping power for electrons in polystyrene (the fiber core material); $P(y,\theta_f)$ was the path-length an electron traversed through the fiber ribbon calculated using *M* and knowledge of the fiber boundaries; and $W(x,\theta_i)$ was the probability of having an incoming electron starting at position x with initial angle θ_i.

For a continuous detector, the imaging equation is

$$R(y) = \int_{E_{\min}(y)}^{E_{\min}(y)} dE \int_{\theta_{\min}(E)}^{\theta_{\max}(E)} d\theta \int_{x_{ap,\min}}^{x_{ap,\max}} dx DRF(E,x,y,\theta)\Phi(E,x,\theta) \tag{4.3}$$

where *R(y)* is the detector signal at point *y*, and Φ is the differential electron fluence with energy *E*, deflection angle from the mean beam direction θ and starting position *x*. Since we are only concerned with the energy distribution of the electron beam, we can immediately integrate over θ and *x*. Adding in the discretization due to the fibers gives

$$R(y_k) = \int_y rect(\frac{y - y_k}{d_k}) dy \int_E DRF(E)\Phi(E) dE \tag{4.4}$$

where y_k is the center of the kth fiber and d_k is the width of the kth fiber.

Equation (4.4) was reformulated as a linear matrix equation

$$R = C\Phi \tag{4.5}$$

where *R* was the observed fiber signal vector, *C* was the pre-computed contribution matrix that determines how a given energy contributes signal to a fiber per unit fluence, and Φ was the energy spectrum. R has dimensions (Kx1), C is (KxM) and Φ is (Mx1). For our system, K is number of fibers (60), and M is the number of desired energy bins for the unfolded spectrum (221 bins, 4 MeV to 25 MeV in 0.1 MeV steps). The C matrix is represented graphically in Figure 61.

Since K<M, we have an under-determined system of equations that cannot be solved by matrix inversion. We used a custom feature-based solver that first fit the peak region of the fiber signal, and then fit the peak+tail. The solver computed a starting trial Φ for each feature (peak then peak+tail), and modified it using predetermined set of shifts and transforms (e.g. raised to exponential powers). The range of shifts and transforms were empirically determined and tuned

to produce acceptable fits in simulated data (see Section 4.2). The Φ that produced the minimum figure of merit was used as the best solution. The figure of merit was given by

$$FOM = \sum_{K} \frac{(R_k - G_k)^2}{\sigma_k^2} \tag{4.6}$$

where K was the total number of fibers. R_k was the kth fiber's measured signal, G_k was the kth calculated of the fiber signal for a given Φ, and σ_k was the uncertainty in the kth fiber's measured signal (from equation (3.1)). This method is graphically depicted in Figure 62 and Figure 63. This fitting method does not assume a known functional shape for the underlying energy spectrum, allowing for the generation of spectral shapes as guided by the measured fiber signals.

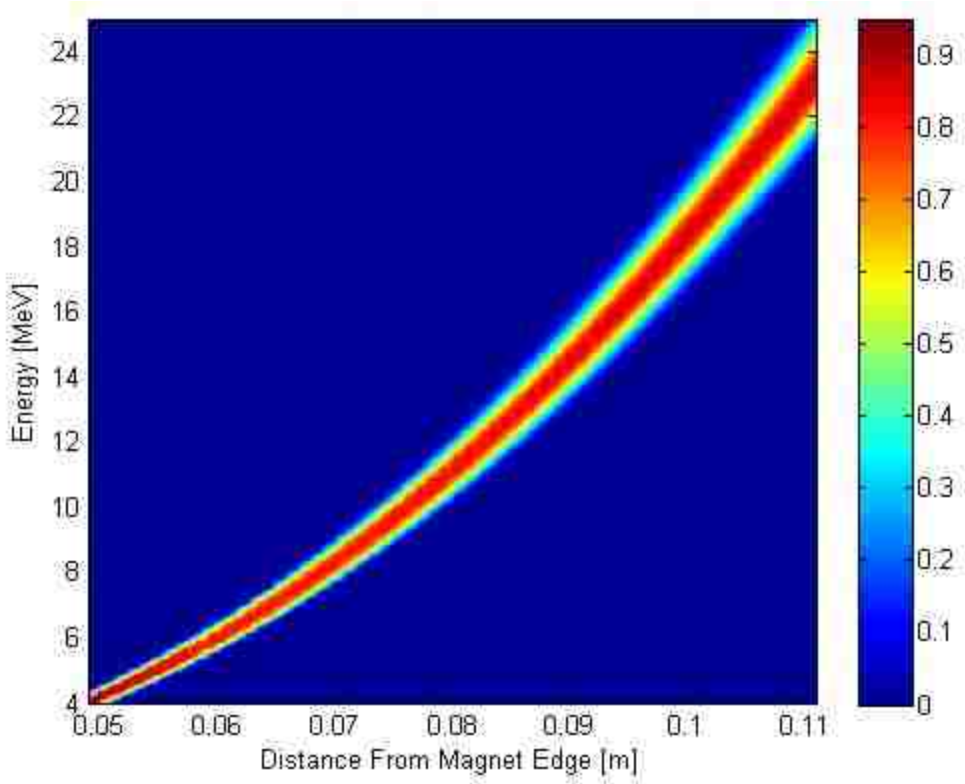

Figure 61. Graphical depiction of the contribution matrix, showing the relative contributions for an energy at a specific point in the detector.

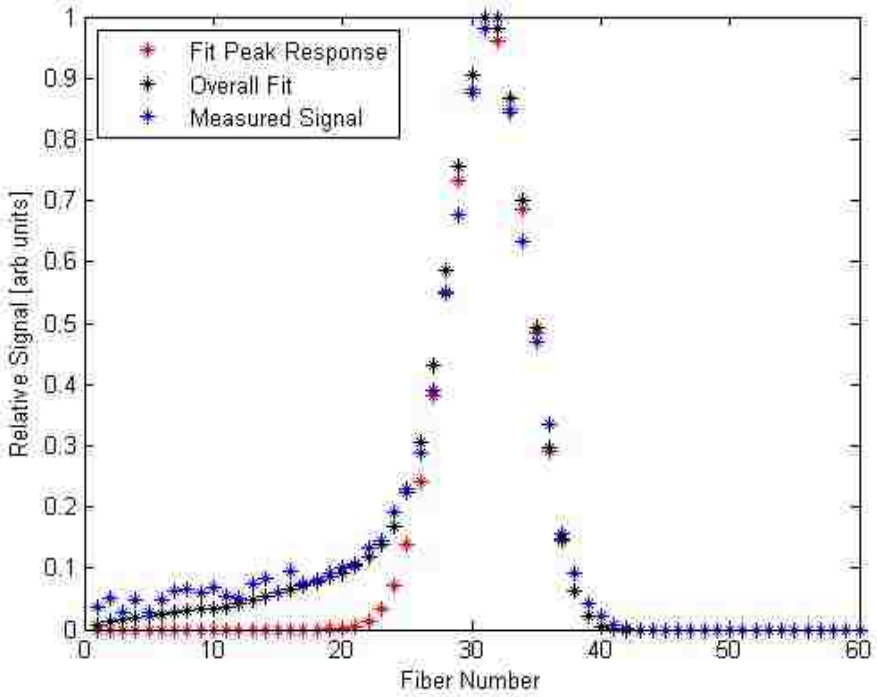

Figure 62. Fitting to the measured fiber response (blue) showing first the fit to the peak (red), and then the final fit (black).

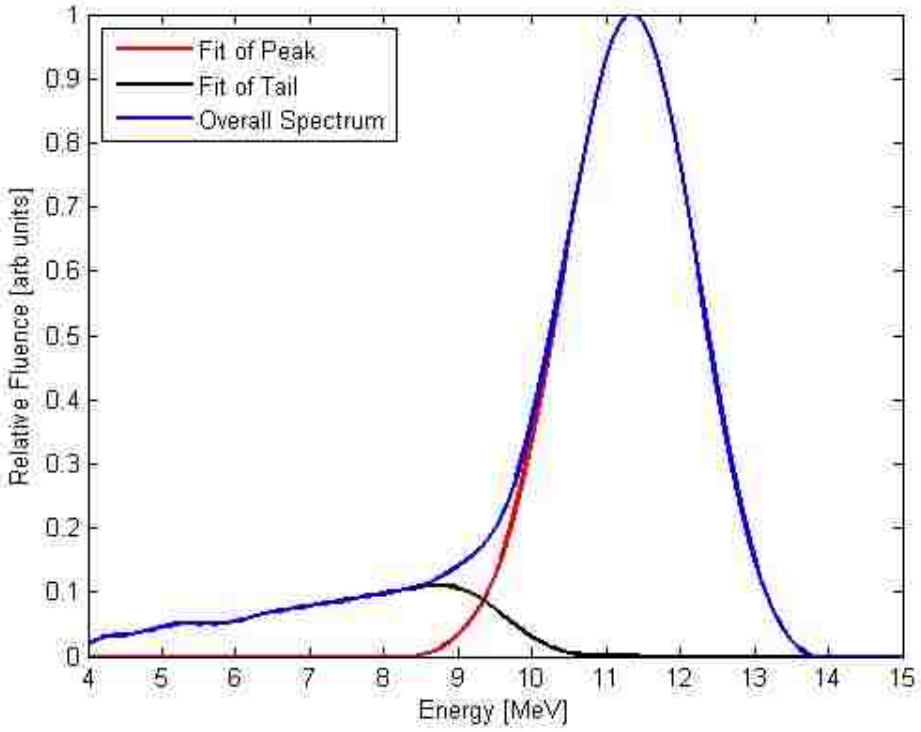

Figure 63. Resultant energy spectrum for the fit above.

4.2. Assessment of Fitting Accuracy

To test the unfolding method, we generated 1000 idealized Gaussian energy spectra with a low energy tail (shifted and scaled logarithm), with E_{p0} ranging between 6.5 and 20.5 MeV and FWHM values between 1 and 4 MeV. Using these ideal spectra and equation (4.4), we produced simulated fiber signals and then added uniform noise to each fiber ranging from 0-20%. We then performed the spectral unfolding on the noisy simulated fiber signals. The spectra were comparted to the ideal spectra to assess trends and biases, such as asymmetries in the peak region of the reconstructed data.

To test the unfolding method's ability to reproduce asymmetric spectra, we generated 1000 Landau distribution[60] shaped spectra using the same parameter ranges as above. These known input spectra were used to produce simulated fiber signals, with added noise, and were then unfolded into the estimated spectra.

The fitting accuracy of our unfolding method for both the Gaussian-peaked and Landau distribution tests is summarized in Table 9. The values presented are the average and standard deviation across all trials.

Table 9. Summary of Unfolding Accuracy. Δ indicates the difference between the ideal value and the unfolded value.

Peak Type	ΔEp0 [MeV]	$\Delta\bar{E}$ [MeV]	ΔFWHM [MeV]	Δ(HWHMR-HWHML) [MeV]
Gaussian	-0.04 ± 0.10	-0.11 ± 0.21	0.06 ± 0.28	0.06 ± 0.17
Landau	-0.26 ± 0.14	0.11 ± 0.27	0.03 ± 0.29	-0.31 ± 0.22

Inspection of the results revealed that:$|\Delta FWHM|$ was positively correlated with increased noise, with a partial correlation (controlling for E_{p0} and FWHM) of 0.42 ($p<0.001$) and 0.15 ($p<0.001$) for the symmetric and asymmetric cases respectively.$|\Delta FWHM|$ was also positively

correlated with E_{p0}, with partial correlations of 0.26 ($p<0.001$) and 0.28 ($p<0.001$) when controlling for both FWHM and noise.

Figure 64 and Figure 65 illustrate the effects of high and low noise at different E_{p0} for Gaussian peaked input spectra. The 95% confidence bounds on the unfolded energy spectra are produced by using the residuals from the fiber signal fit and the signal uncertainties. On average, for Gaussian peaked input spectra, the unfolding method reproduced the spectral quantities listed in Table 9 within the digitization resolution (0.1 MeV). This accuracy was severely degraded for spectra near the measurement bounds of our device (Figure 65), especially when there was a large degree of noise. This was because our method was no longer able to accurately define a peak region for fitting. However, in measured data we have not observed this level of noise and have always had a clearly defined peak.

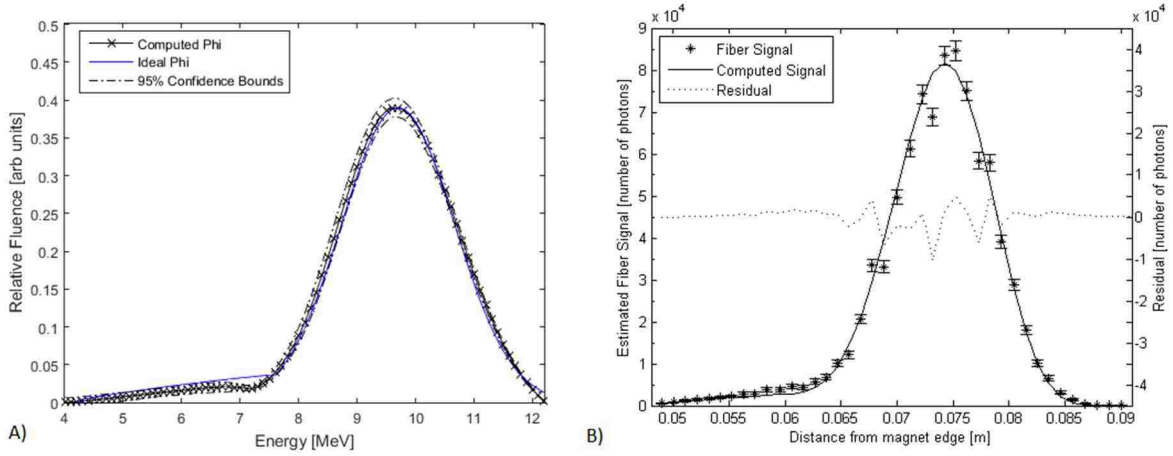

Figure 64. Simulated fitting of a Gaussian peaked input spectrum, typical fit; ideal E_{p0}: 9.7 MeV; ideal FWHM: 2.27 MeV; noise: 7.0% A) Unfolded spectrum and ideal input spectrum. ΔFWHM: 0.09 MeV; ΔE_{p0}: 0.05 MeV. B) Simulated fiber signal from ideal input spectrum, and resultant fiber signal curve from the unfolding method.

Figure 66 illustrates a sample Landau distribution fitting case. For these asymmetric spectra, the average energy and FWHM fitting accuracy and precision were comparable to the Gaussian

trials. However, the unfolding method was not able to correctly reproduce an asymmetric peak as seen by the bias in the E_{p0} position and the Δ(HWHMR-HWHML).

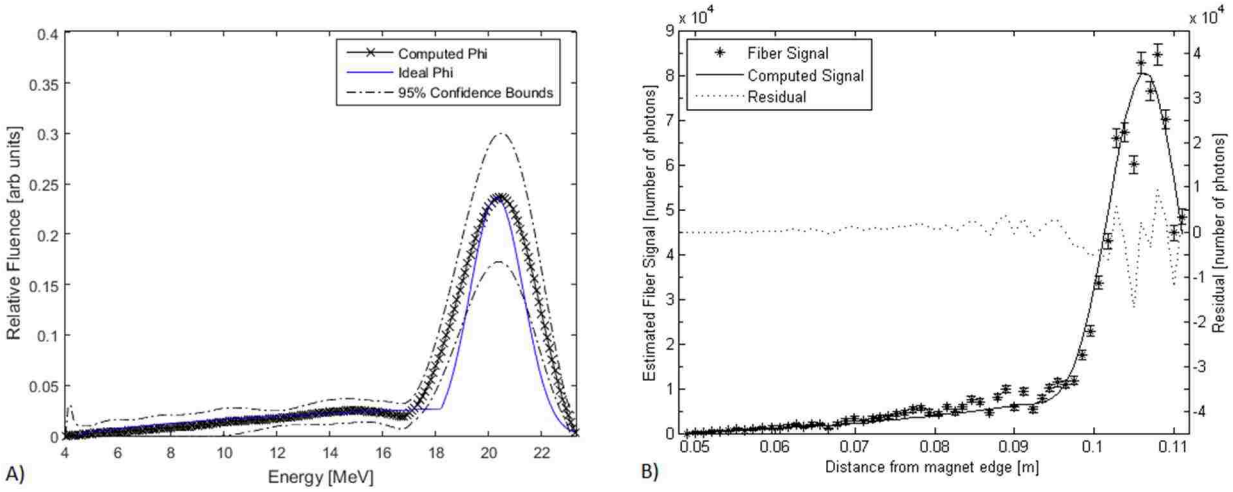

Figure 65. Simulated fitting of a Gaussian peaked input spectrum, worst-case fit; ideal E_{p0}: 20.3 MeV; ideal FWHM: 2.37 MeV; noise: 19.0%. A) Unfolded spectrum and ideal input spectrum; ΔFWHM: 1.05 MeV; ΔEp0: 0.15 MeV. B) Simulated fiber signal from ideal input spectrum, and resultant fiber signal curve from the unfolding method.

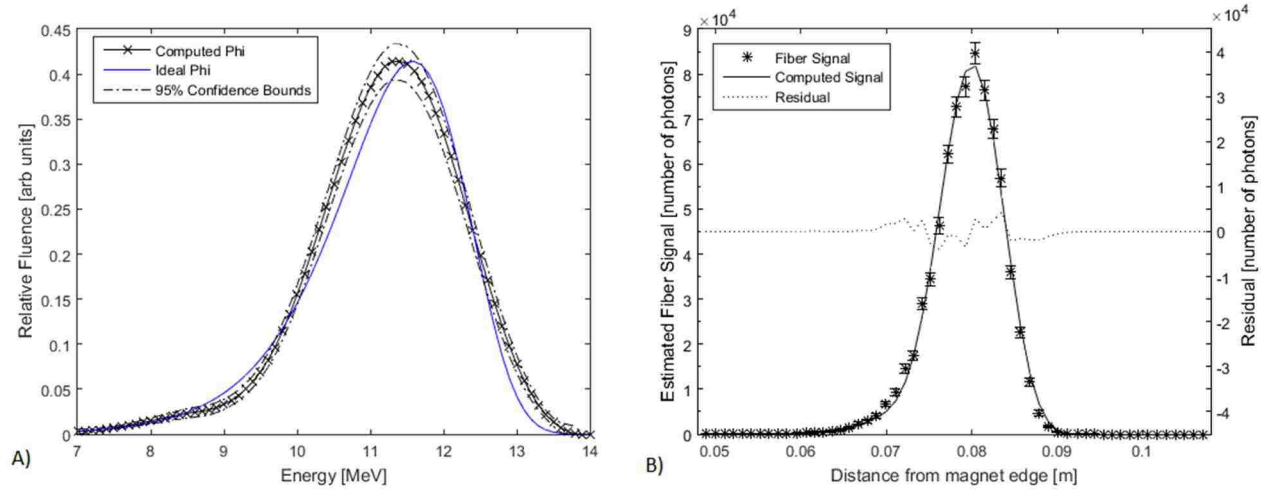

Figure 66. Simulated fitting of a Landau distribution input spectrum. Ideal E_{p0}: 11.58 MeV; FWHM: 2.09 MeV; $\bar{E}$: 11.17 MeV, $HWHM_L$-$HWHM_R$: 0.36 MeV; noise: 4.7%. A) Unfolded spectrum and ideal input spectrum. ΔE_{p0}: 0.23 MeV. $\Delta\bar{E}$: 0.05 MeV; Δ FWHM: 0.02 MeV, Δ($HWHM_L$-$HWHM_R$): 0.31 MeV. B) Simulated fiber signal from ideal input spectrum, and resultant fiber signal curve from the unfolding method.

.

The two primary limitations of the spectral unfolding method were the inherent degeneracy in our measurement system that results from having 60 sampling points in space while trying to

reconstruct 211 energy bins (4 to 25 MeV, 0.1 MeV steps). In addition, the large aperture size (6.35 mm diameter) needed to produce adequate fiber signal compared to the fiber size (1 mm) resulted in a each energy being smeared over many fibers, disallowing a simple position to energy conversion. This degeneracy resulted in a large variance in fitting accuracy, crucially with the decrease in fitting accuracy with increased noise. These issues can be addressed by choosing different detector hardware. For example, a high resolution solid state detector may provide an increased number of spatial sampling points at a higher sensitivity than the fiber + camera system used in the present study, allowing the aperture size to be decreased for comparable signal levels, while allowing a simpler, non-iterative unfolding method, similar to what was used with the previous, CR based spectrometer[40].

4.3. Generation of PDD Curve

While the energy spectrum of an electron beam provides a more detailed description of the electron beam from a physics perspective, clinical medical physicists are most accustomed to comparing PDD curves. We implemented an energy spectrum to PDD conversion function by taking a weighted sum of the energy spectrum and monoenergetic PDD kernels. The kernels were computed for monoenergetic electrons beams using the Geant4 Monte Carlo toolkit [61-63] by simulating a small (2 mm x 2 mm) monoenergetic electron source located 90 cm from the surface of a cube of water (50 cm side length).

The electrons were produced as an initial parallel beam. Scatter was modeled as the electrons propagated through the 90 cm of air from the production point to the water surface. We varied the energy from 4 to 25 MeV in 0.1 MeV steps to match the reconstruction spacing, and tabulated total dose deposited in water in 0.5 mm increments; summing the total dose at a given depth from a point-like source is equivalent to the point dose at the depth due to a broad field[64],

and is much more computationally efficient. Ten million source particles were generated for each energy. This resulted in maximum computational uncertainties less than ~2% depending on the energy. An example PDD result is shown in Figure 67. The PDDs produced by from the energy spectra are similar in shape to clinical PDDs (ref Figure 1).

We do not expect computed PDDs to exactly match PDDs acquired from a water tank because the simplistic PDD kernels were not fully analogous to the source and angular distribution of clinical beams (i.e. we did not model the full accelerator head, scatter foils, or bremsstrahlung background). Therefore, calculated PDDs should not be used as reference PDDs the treatment-planning software because the current simulation. However, the computed PDDs can still be used in conjunction with the energy spectrum for linac tuning and QA because the current QA tolerances and beam matching criteria are based on PDD values, not energy spectra.

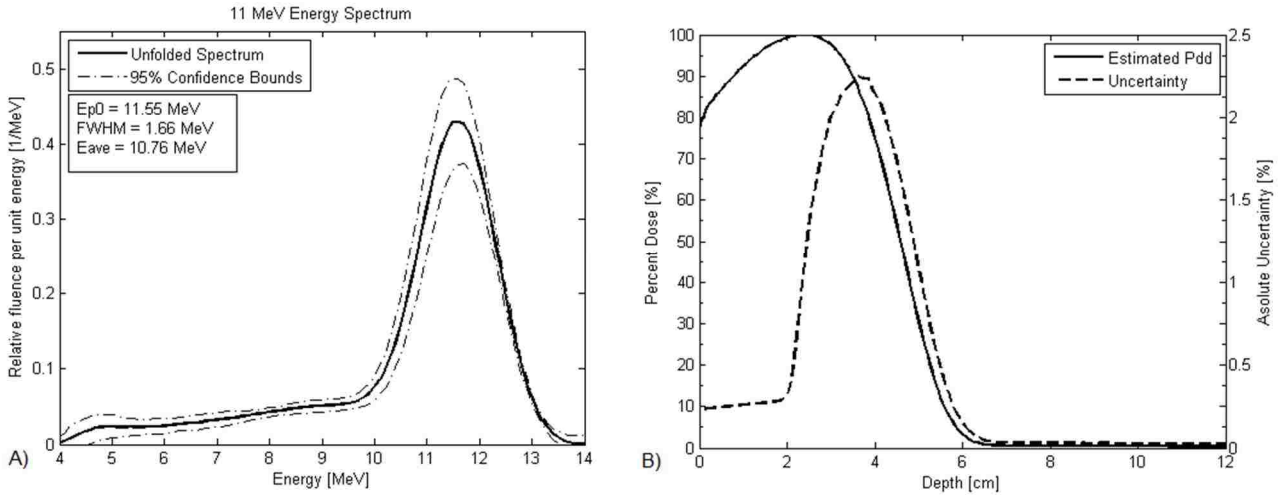

Figure 67. Measured energy spectrum at 11 MeV (A) and its calculated PDD (B). The uncertainty in the PDD only reported for the computational uncertainty in the Monte Carlo kernels.

4.4. Use of the Software for Data Acquisition and Analysis

As mentioned during the description of the spectrometer in Section 3.1, the acquisition was controlled by the PixeLINK Capture software, and the unfolding was performed using

MATLAB. This section describes the key features and settings of each piece of software, followed by a guide on how to operate the software to take spectrometry measurements.

4.4.1. Image Acquisition with PixeLINK Capture

The PixeLINK capture software (Figure 68) allows detailed control of the camera settings and acquisition methods. All images were exported as a bitmaps. The gain and exposure settings were adjusted using the "Basic Controls" window. No other image settings (e.g. brightness, saturation, gamma) were modified. For routine, single shot acquisitions, the "Capture" button on the "Basic Controls" tab was used. For multiple, repeated acquisitions, the functionality on the "Image Capture" tab was used. This allowed the user to select how many images (with the gain and exposure settings from the "Basic Controls" tab) to acquire, and at what interval.

For flood images, the naming format was "flood_[type][image number].bmp". [type] was either "rect" for flood images acquired with the rectangular insert, or "blocked" for flood images acquired using the solid insert. [image number] was a 4 digit numerical string indicating the acquisition number, ranging from "0001" to "9999". If the "Increment File Name After Capture" option was selected, the [image number] would be automatically incremented after each image capture.

For spectrometry acquisitions and spectrometry backgrounds, the file naming format was "[energy]_[acquisition type]_[exposure]_[gain]_[image number].bmp"; [energy] was the beam energy with units MeV, e.g. "10MeV"; [acquisition type] was either "beamOn" for spectrometry acquisitions or "blocked" for background acquisitions; [exposure] was the camera exposure setting with units ms, e.g. "1000ms"; [gain] was the gain setting in the format "[integer]dB[decimal], e.g. a gain of 14.04 dB would be "14dB04"; and [image number] as used

above. For example, a 13 MeV beam, spectrometry acquisition at 1000 ms exposure, 14.04dB gain, third image would be “13MeV_beamOn_1000ms_14dB04_0003.bmp”.

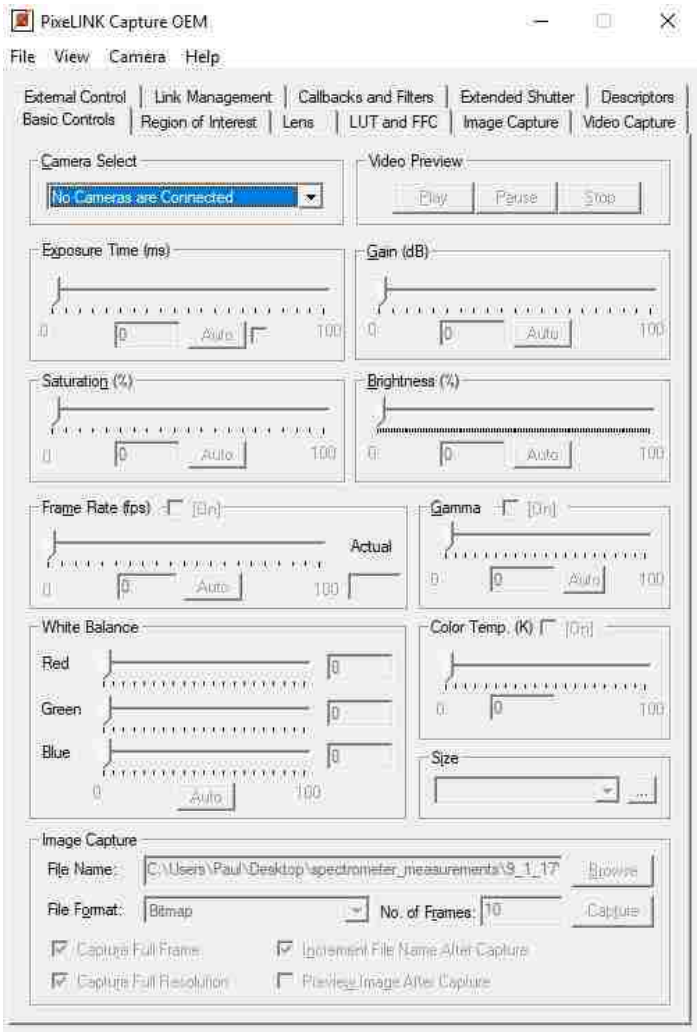

Figure 68. Screenshot of PixeLINK Capture software, showing the “Basic Controls” tab.

The file structure used for image storage was “~/spectrometer_measurements/[date]/[set]/”. [date] was in the form of “[month]_[day]_[year]”, e.g. “5_15_17” for May 5th, 2017. [set] is a subfolder, with the format of “setN” where “N” is an integer, e.g. “set1”. Flood images should be stored in the “~/[date]/” folder. The “~/[set]/” subfolder is where spectrometry data (both beamOn and blocked) should be stored. Sets was used when trying different setups or variations.

At least one ambient image (used to quantify light leakage from the environment) for both the flood acquisition setup and the spectrometry acquisition setup should be acquired, and placed in the "~/[date]/" folder. The ambient images should be acquired at the same camera settings as the flood or spectrometry acquisitions. The naming format is "ambient_flood[image number].bmp" and "ambient_[image number].bmp" for the flood and spectrometry acquisitions, respectively.

4.4.2. Spectral Unfolding and Data Processing using MATLAB

All functionality besides image acquisition (e.g. unfolding, plotting, storage, etc) was performed in MATLAB. Once the user provided the initial settings and desired functionality, all other steps were fully automated. A code snippet from the main control script that contains the important user-adjustable settings is shown in Figure 69. The two main portions of this snippet are the analysis variables (top of the image) and the user settings (bottom of the image). For brevity, the rest of the script is not shown.

For the analysis variables, the user may select the desired behavior by setting the variable to the appropriate binary (0 for disabled, or 1 for enabled) or integer value; the options are:

- numAcqs: total number of images to look for in each energy. Type: integer.
- plotPhis: plots the energy spectrum. If "showRef=0" then the 95% confidence interval is displayed with the spectra. Type: binary.
- plotResps: plots the measured fiber signal curve, and the estimated response due to the unfolding method. Type: binary.
- saveData: save all spectra, fiber signal curves, and relevant spectral descriptive parameters to temporary variables. Type: binary.

- checkBkgd: checks for a spectrometry background image taken on the same day at the same energy. Otherwise a reference background is used. Type: binary.
- showRef: if plotPhis or showPdd are enabled, overlays a reference spectra or PDD on the plots. Type: binary.
- showPdd: displays the PDD, computed from the energy spectrum. If "showRef=0" then the uncertainty of the PDD is displayed. Type: binary.
- startNum: acquisition start number; it does not have to be in 4 digit format. Type: integer.
- showQuants: if plotPhis is enabled, displays the spectral descriptive parameters (E_{p0}, FWHM, E_{ave}) on the spectrum plot. Type: binary.

```
%% the following flags are for plotting and data storage
numAcqs = 1;
plotPhis = 0;
plotResps = 0;
saveData = 1;
checkBkgd = 1;
showRef = 1;
showPdd = 0;
startNum = 1;
showQuants = 1;

%% image settings
codeLoc = 'C:\Users\Paul\Google Drive\LSU\Spectrometer Research\the code\new code\';
imgLoc = 'C:\Users\Paul\Desktop\spectrometer_measurements\';
dataDir = 'C:\Users\Paul\Google Drive\LSU\Spectrometer Research\Data\fiber_bounds_data\';

updateDelay = 0;
enesForLoop = [13];
addlOpts = 'setl';
testDate = '5_15_17';
expos = '_1000ms_';
gain = '14db04';
gainBkgd = '14db04';
picType = '.bmp'; %image type
```

Figure 69. Code snippet of the main spectrometer control code. The top section are binary user flags for analysis and plotting settings, and the lower potion is related to the image settings.

The lower portion of the screen snippet contains the image setting variables. These must be matched to the file format and naming structure as described in 4.4.1. The "codeLoc" variable is

the path to the location of the main script; the ".m" files for the other functions used in the main script should also be located in that folder. The "imgLoc" variable is the path to where the images are being stored. The "dataDir" variable specifies the data folder for placing fiber ROI data, fiber correction factors, and averaged ambient images. The software automatically creates a subfolder "~/[dataDir]/[date]/" to store this data. The expected folder structure should be the same as described in 4.4.1. "updateDelay" specifies the minimum total time in seconds between when the software begins analysis on a new image. An updateDelay value of "0" means the software automatically proceeds with analyzing the next image once it completes the current analysis and graphing task; a value greater than the time taken to perform analysis and graphing (usually ~0.8 s depending on the computer hardware) will cause the software to wait until the total amount of time since the beginning of analysis has elapsed before proceeding to the next image. The "enesForLoop" variable is a vector that contains the beam energies to be analyzed. For example, if one is acquiring 13 MeV data, they would set "enesForLoop" to be the value "13". For retrospective analysis on previously acquired images, multiple energies can be used, such as "enesForLoop = [13, 16, 20]"; the software will then analyze the specified range (from startNum to startNum+numAcqs) of images, and then loop through each energy.

4.4.3. Spectrometer Use Procedure

An flowchart of providing an overview of how a user would operate the spectrometer is shown in Figure 70.

The first step in using the spectrometer is acquiring the flood (both the rectangular field and the blocked, background field) as described in 3.1.1. If the user does not want to acquire flood images, they can either copy a previous flood image to a new "~/spectrometer_measurements/[date]/" folder, or copy previous fiber bounds and fiber

correction to the "~/[dataDir]/[date]/" subfolder. Next, the user should setup the spectrometer for spectrum acquisition (as described in 3.1.2), and acquire the spectrometry backgrounds and at least one ambient image. If multiple ambient images are acquired, they will be averaged by the software automatically, and the resultant image will be placed in the "~/[dataDir]/[date]/" subfolder.

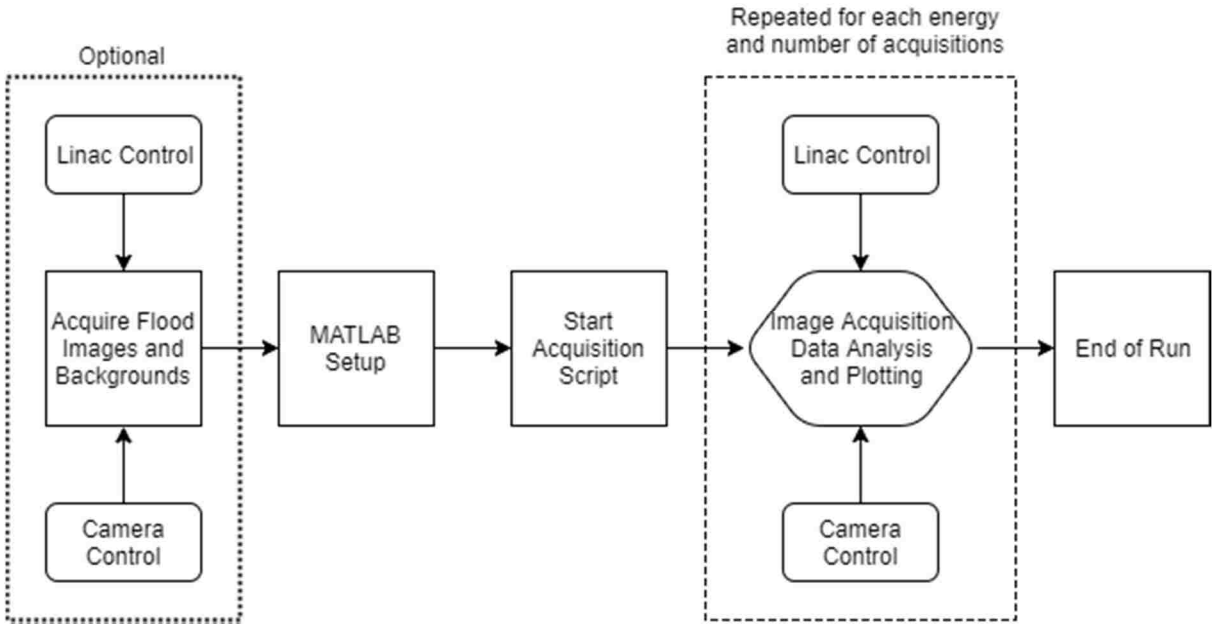

Figure 70. Flowchart of how to operate the spectrometer.

Once all the pre-spectrometry images have been acquired and the spectrometer is setup with the 6.35 mm aperture insert placed in the electron applicator, the user should select the desired software functionality as described in 4.4.2. Then the user should run the main script. An outline of the main script is shown in Figure 71. This will perform fiber ROI determinations, and calculate fiber correction factors if they are not present. Next, the user should use the linac service mode functions to produce the desired electron beam, and use the PixeLINK software to acquire images. The main script waits for an image with the proper file format at the first energy and image number. Once that image is acquired, it is automatically processed, and the user

selected plots are displayed. This process is repeated until the total number of acquisitions at a given energy is reached, and then is repeated for each energy as specified during setup.

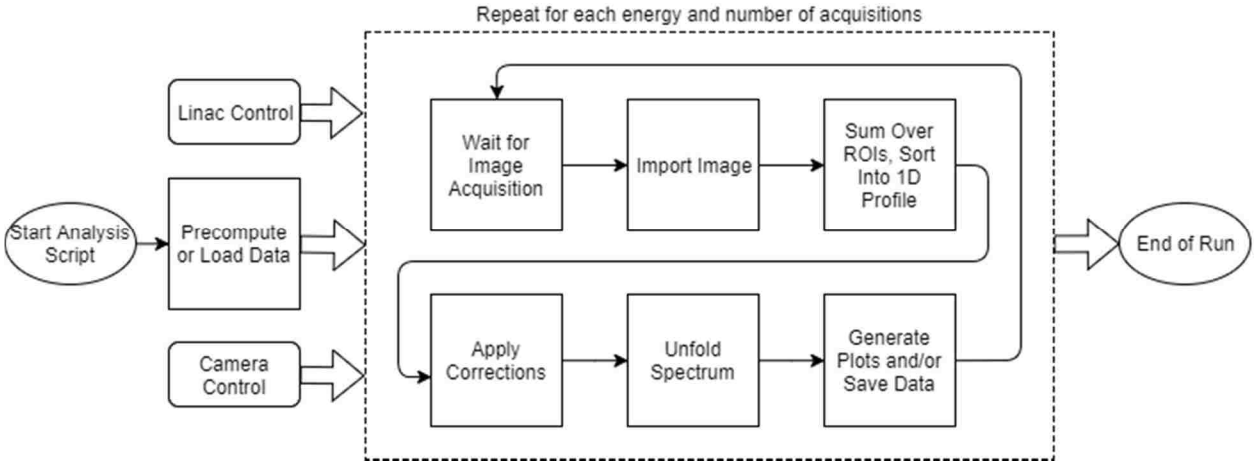

Figure 71. Flowchart of main MATLAB analysis script.

5. APPLICATIONS OF THE SPECTROMETER

This section addresses the use of the spectrometer as a clinical or research tool. The clinical utility of a real-time electron spectrometer is the rapid acquisition of energy spectra and computation of the PDD. This can facilitate commissioning, routine quality assurance, or linac characterization research. Research applications include characterization of aspects of linear accelerator operation that may not have immediate clinic impact, but may provide insight into the machine's performance to assist in future studies. For example, the acquired energy spectra could be used as the input file for a Monte Carlo treatment planning study.

Test were performed using an Elekta Infinity with the Agility head (Elekta, Stockholm, Sweden) or an Elekta Versa HD at the Mary Bird Perkins Cancer Center in Baton Rouge, with the linac running in service mode and the "quick beam" function.

5.1. Comparison to CR Plate-based Spectrometer

The real time spectrometer system was compared to the CR plate (Agfa MD-10, Agfa-Gevaert N.V., Belguim), passive spectrometer system[14,40]. Two full sets of spectra (energies 7, 9, 10, 11, 13, 16, 20 MeV) were first acquired for the passive spectrometer following the procedure outlined in McLaughlin[14]. The only modification to this acquisition method was, because the real-time detector system was already mounted on the magnet block, the CR plates were placed on the magnet exit-face opposite the real-time detector system and the magnet was rotated 180º from its usual orientation (Figure 72).

The steel and aluminum mounting hardware holding the two individual magnets apart was symmetric at both ends (i.e. two entrance apertures) aside from a small aluminum extension at one end (q.v. Figure 14 and Figure 17); we assumed the magnetic field inside the magnet block was unchanged by this rotation. This allowed a quick transition from the passive system to the

real-time system because we did not need to reinstall the real-time detector. Each spectrum took 2-3 minutes to acquire, for a total acquisition time of approximately 40 minutes.

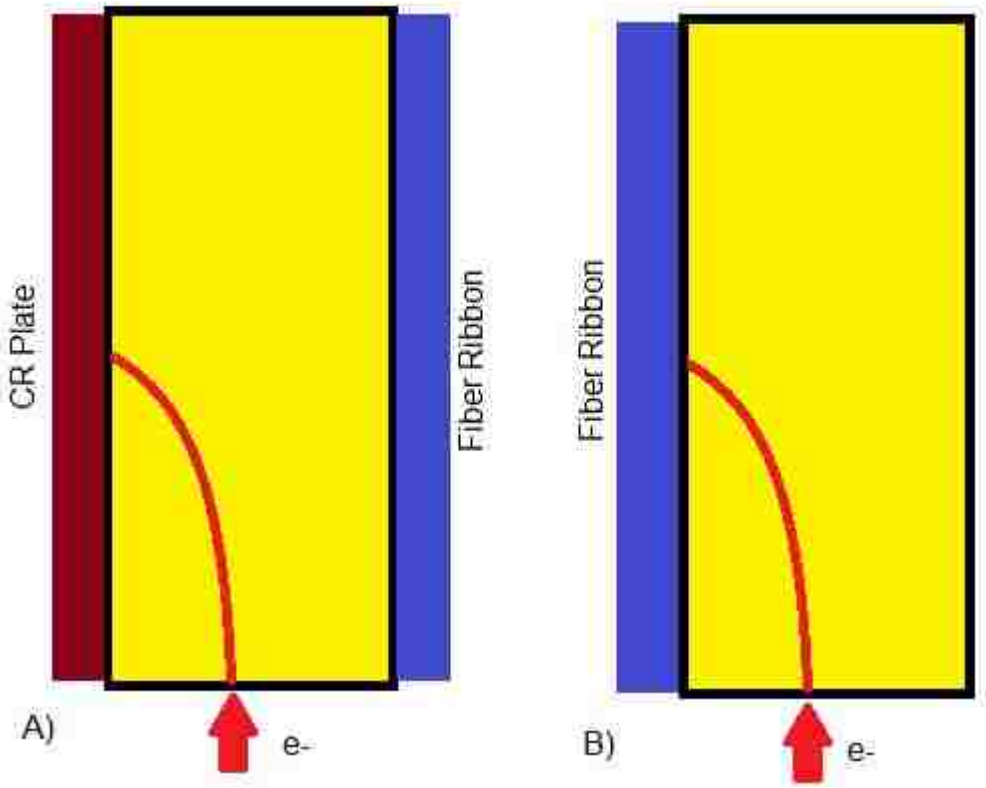

Figure 72. Spectrometer setup for CR plate based acquisitions (A) and real-time acquisitions (B). The red indicates electron paths in the magnetic field (yellow). The blue area indicates the fiber ribbon (real-time detector), and the brown area represents the CR plates (passive detector).

Once all passive spectra were acquired, the spectrometer was setup in the configuration given in Section 3.1.2. Background measurements and flood images had been acquired prior to the passive acquisitions. Three full sets of spectra were acquired taking a total time of approximately 10 minutes. The total time to complete all acquisitions for both the passive and real-time spectrometer versions was less than one hour, and the accelerator performance was assumed to be constant between the passive and real-time acquisitions. After all acquisitions were completed, the CR plates were read out using a C431200 Cyclone Plus Storage Phosphor System

(PerkinElmer, Waltham, MA) and analyzed using the method from McLaughlin[14]; the CR plate readout and analysis took an additional two hours.

The spectra are presented in Figure 73-Figure 79. The overall spectral shapes between the passive and real-time spectrometers were consistent to within the 95% confidence bounds of the real-time spectrometer, except for 10 MeV. However, the peak positions (E_{p0}) were not consistent. This was because the passive spectrometer used a constant valued magnetic field model with an field edge offset parameter; these values were tuned to produce spectra that matched measured PDD curves (q.v. Figure 12) based on the ICRU 35 relationship. This resulted in different effective position to energy relationships between the passive and real-time spectrometer, creating a shift in energy between the two systems. In order to compare spectra, the spectra produced from the passive device were shifted to provide the same E_{p0} values as the real-time spectrometer.

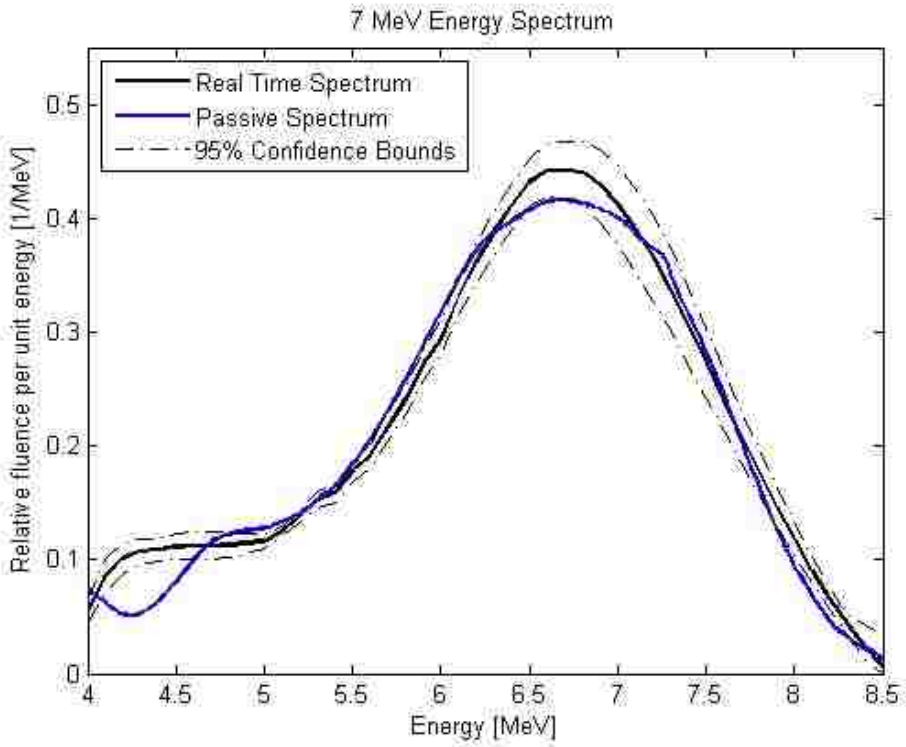

Figure 73. Comparison of passive versus real-time spectrometer results; 7 MeV beam.

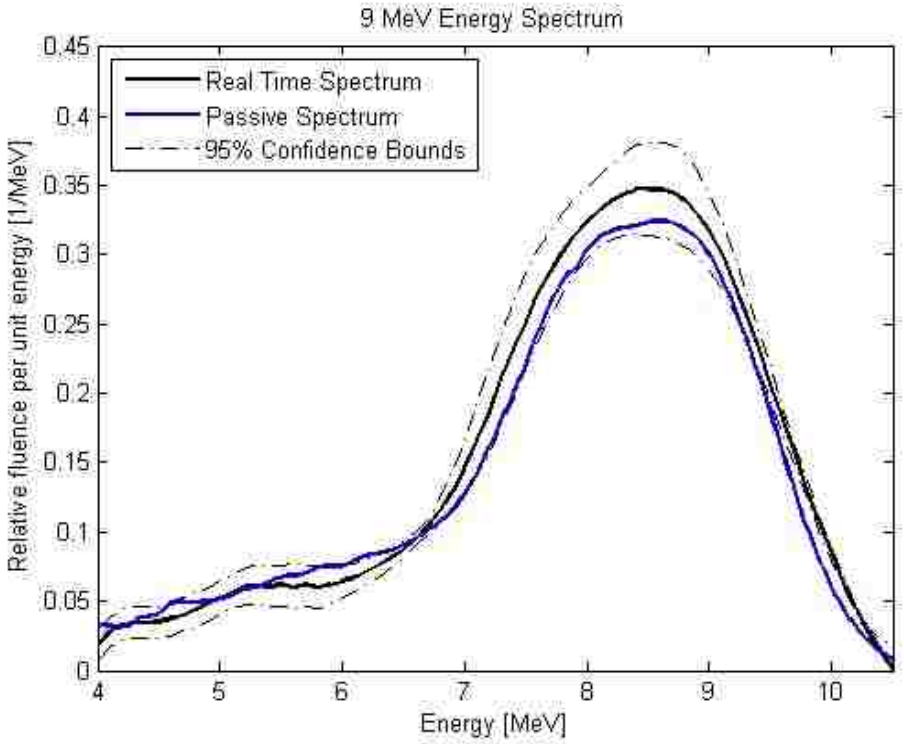

Figure 74. Comparison of passive versus real-time spectrometer results; 9 MeV beam.

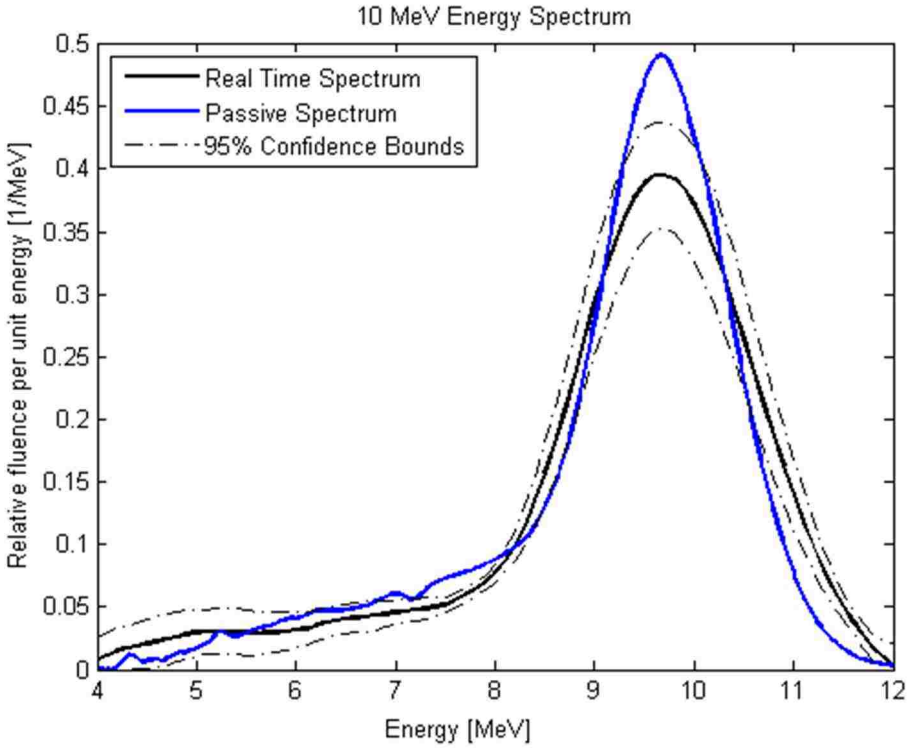

Figure 75. Comparison of passive versus real-time spectrometer results; 10 MeV beam.

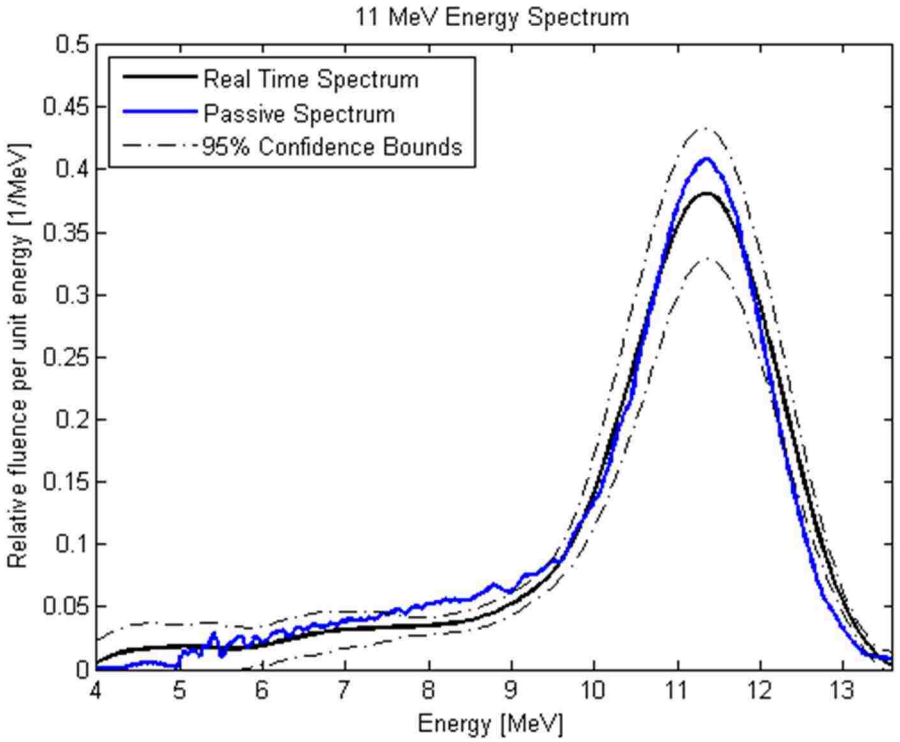

Figure 76. Comparison of passive versus real-time spectrometer results; 11 MeV beam.

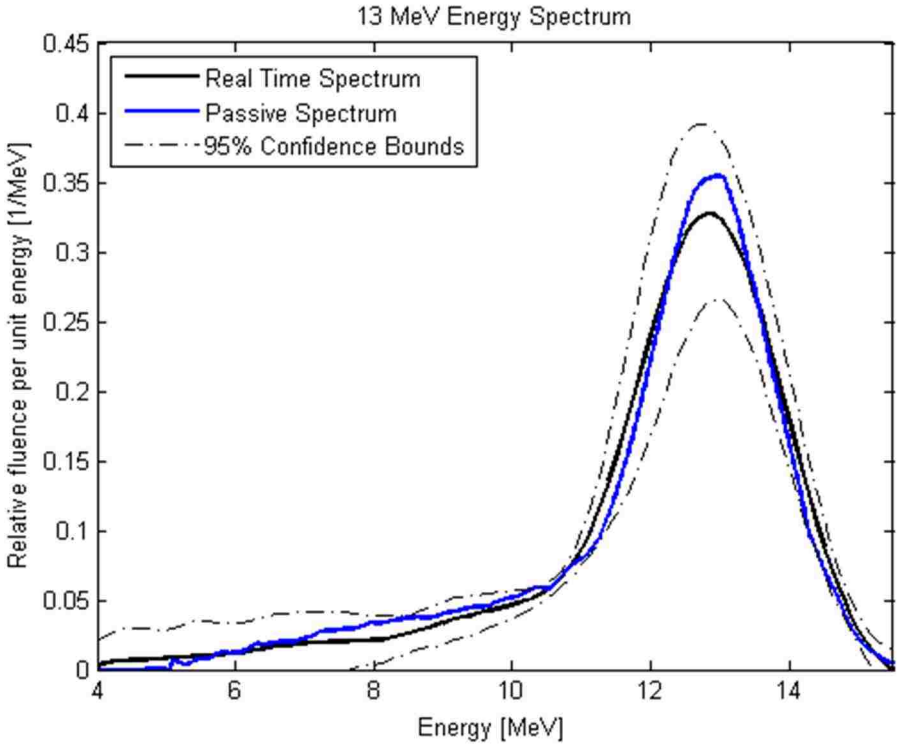

Figure 77. Comparison of passive versus real-time spectrometer results; 13 MeV beam.

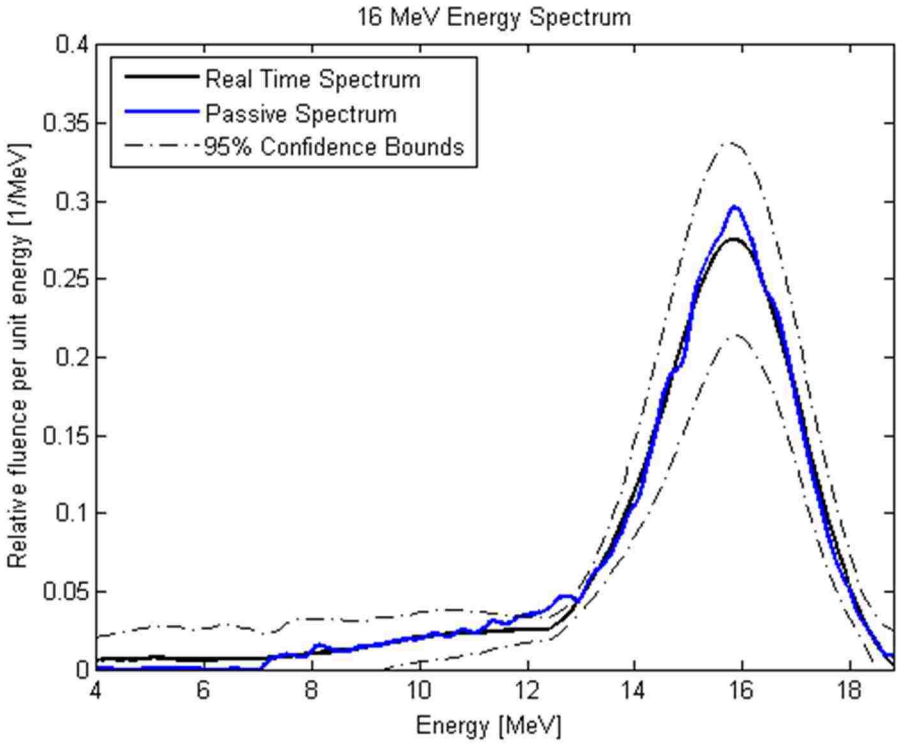

Figure 78. Comparison of passive versus real-time spectrometer results; 16 MeV beam.

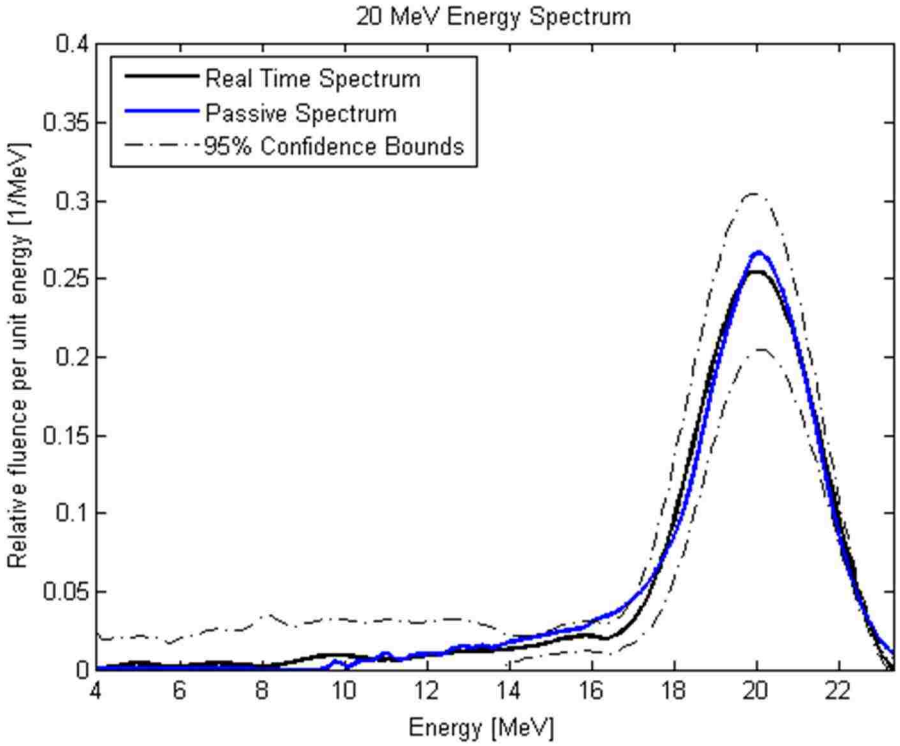

Figure 79. Comparison of passive versus real-time spectrometer results; 20 MeV beam.

The agreement between the passive and real-time spectrometers provided confidence in the general accuracy of the measured spectra. However, without an externally calibrated source, we cannot know which spectra is "more correct." Furthermore, the analysis method for the passive spectrometer was reliant on user input when selecting the signal background and parameters for signal fitting and smoothing; this could introduce inconsistent artifacts in the spectra measured with the passive device (e.g. the low energy upturn at 7 MeV, Figure 73, or the ripple in the low energy tail at 11 MeV, Figure 76) as compared to the automatic method used with the real-time device.

5.2. Many Acquisitions at Two Dose Rates

We acquired 100 spectra at a nominal 400 MU/min dose rate (actual dose rate between 400-450 MU/min) for electron beam energies of 7, 9, 10, 11, 13, 16, 20 MeV and 50 spectra at a nominal 200 MU/min (actual 210-225 MU/min) for energies of 7, 13, and 20 MeV. For the lower dose rate acquisitions, the camera exposure time was increased from 1000 ms to 2000 ms to have comparable signal levels to the higher dose rate. Each set of spectra was acquired during a single beam delivery instance to assess the energy stability during prolonged operation of the linac. Spectra acquisition started at 20 MU into the delivery and ran continuously until the desired number of spectra were acquired. The spectrometer was not moved between acquisitions. E_{p0}, FWHM and $\bar{E}$ were calculated for each acquisition.

Table 10 summarizes calculated descriptive parameters for the acquired spectra. Averages and the standard deviations were calculated from all 100 (400 MU/min dose rate) or 50 (200 MU/min dose rate) spectra at each energy. The standard deviation reflects only the measurement variance. Figure 80 plots the mean spectra for each energy.

Table 10. Measured energy spectral parameters on Elekta Infinity, acquired at two dose rates. The values listed are the average and standard deviation of the measurements.

Nominal Energy [MeV]	E_{p0} [MeV]		FWHM [MeV]		$\bar{E}$ [MeV]	
	400 MU/min Dose Rate	200 MU/min Dose Rate	400 MU/min Dose Rate	200 MU/min Dose Rate	400 MU/min Dose Rate	200 MU/min Dose Rate
7	7.15 ± <0.01	7.15 ± <0.01	1.88 ± 0.11	1.79 ± 0.05	6.87 ± 0.02	6.90 ± 0.02
9	8.94 ± 0.03	-	2.14 ± 0.06	-	8.40 ± 0.02	-
10	9.98 ± 0.05	-	1.58 ± 0.10	-	9.39 ± 0.07	-
11	11.55 ± <0.01	-	1.72 ± 0.06	-	10.73 ± 0.03	-
13	12.97 ± 0.04	12.96 ± 0.03	1.94 ± 0.09	1.98 ± 0.10	12.09 ± 0.05	12.21 ± 0.04
16	15.62 ± 0.05	-	2.40 ± 0.07	-	14.51 ± 0.11	-
20	19.52 ± 0.05	19.55 ± <0.01	2.58 ± 0.06	2.90 ± 0.06	18.22 ± 0.06	18.17 ±0.06

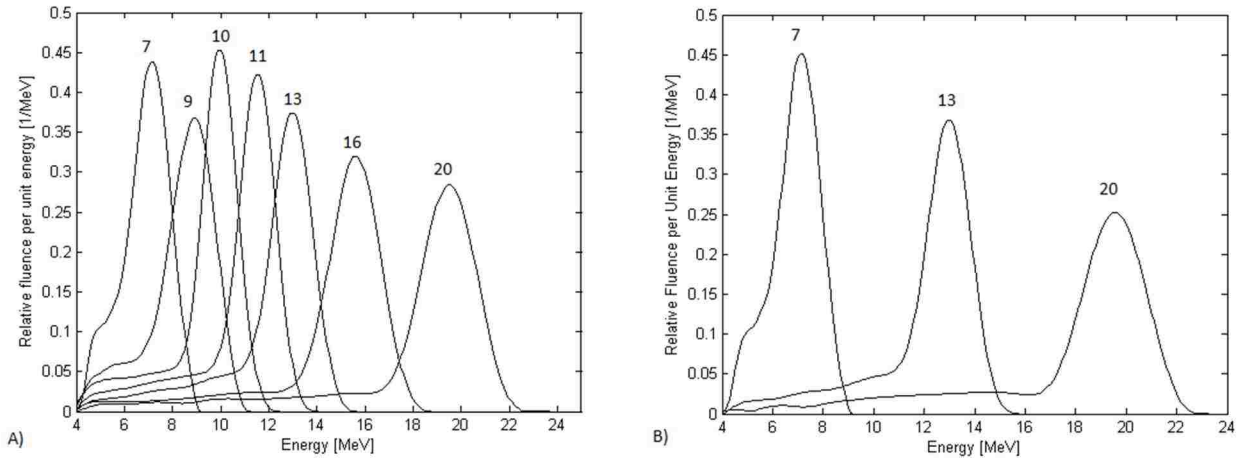

Figure 80. Electron energy spectra from an Elekta Infinity. A) Mean spectra with linac operating at nominal 400 MU/min dose rate. B) Mean spectra with linac operating at nominal 200 MU/min dose rate. Each spectrum is labelled with the nominal beam energy.

The 7 MeV and the 13 MeV beams were consistent between the two dose rates when comparing E_{p0}, FWHM, and $\bar{E}$. For the 20 MeV beam, E_{p0} and $\bar{E}$ values were consistent at both dose rates, though the FWHM value was statistically significantly different ($p<0.001$). The 20 MeV, low dose rate spectra were shorter and broader than the high dose rate spectra (Figure 81).

These results demonstrate the spectrometer's ability to characterize linac performance at different energies, dose rates, and variations during prolonged operation. We have demonstrated the spectrometer's ability to detector linac performance variations by measuring a 9.4% difference in the mean FWHM values for the 20 MeV beam at different dose rates. The modification of the spectra FWHM was likely due to a combined effect of reduced beam loading in the accelerator at the lower dose rate, and the response time of the feedback controls of the linac.

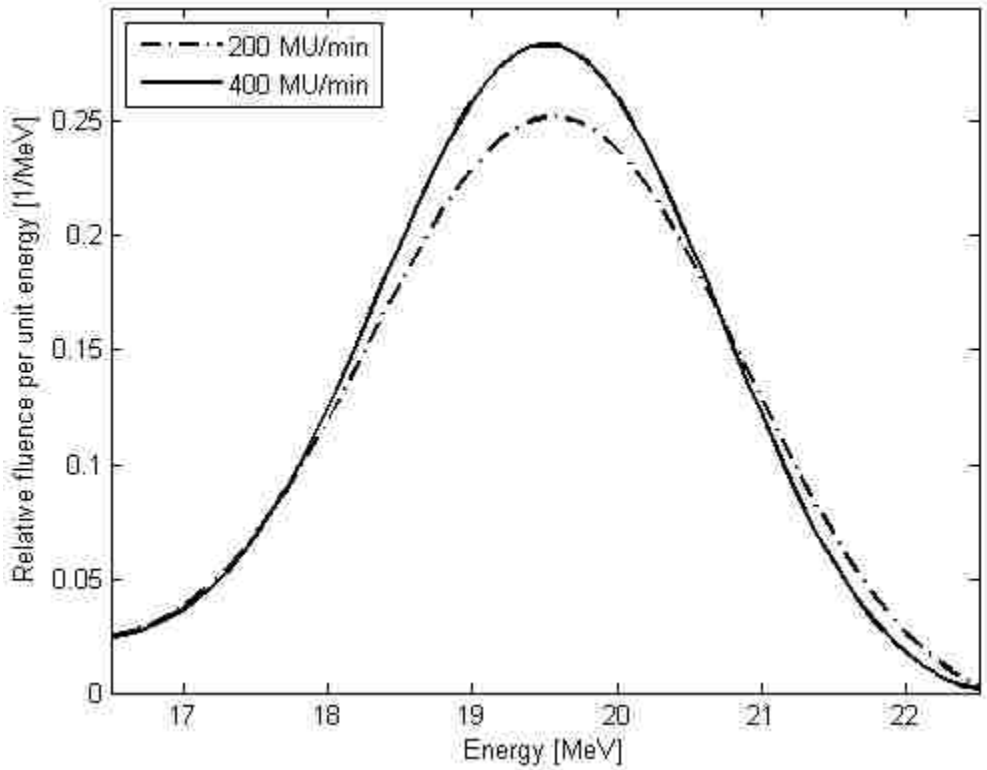

Figure 81. Comparison on 20 MeV spectra at two dose rates.

5.3. Energy Spectral Changes with Known Variations in Linac Tuning Parameters

The ability of the real-time spectrometer to detect changes in the electron energy spectrum due to modifications of the linac settings, primarily the bending coarse/fine magnet currents and the high power phase shifter (HPph) position was assessed by spectral measurements on the Versa HD Linac at MBPCC. The goal was to determine if the spectrometer could be used to

assist in beam tuning and matching. Changes to the bending magnet currents were assessed at 7 MeV because a small (~1-2 A) change in current should result in the largest percentage change of the spectral parameters. The effect of variations to the high power phase shifter were assessed at 13 MeV because it was the highest available energy on the Versa HD, and should therefore rely more on the high power phase shifter. Detector images were acquired at a 1.25 second interval, with 1000 ms exposure time.

5.3.1. Bending Magnet Changes at 7 MeV

Using the 7 MeV beam, we increased or decreased the fine/coarse current ratio (F/C) of the bending magnets, with the anticipated result of shifting the energy spectrum without significantly modifying the spectral shape. The F/C ratio is used by Elekta service engineers as the primary energy tuning metric (private communications, Paul Kairdolf, Elekta Service Engineer). Increasing the coarse current (decreasing the F/C ratio) should result in shifting the spectra to a higher energy; decreasing the coarse current should shift the spectra to lower energies. Table 11 lists the bending magnet parameters that were evaluated.

Table 11. Bending Magnet Ratio Settings for 7 MeV

Settings	Coarse Current [A]	Fine Current [A]	F/C [%]
Initial Values	48.5	2.5	5.1 %
F/C Ratio 1	50.0	2.5	5.0 %
F/C Ratio 2	53.0	2.3	4.3 %
F/C Ratio 3	47.0	2.5	5.3 %

Multiple spectra were acquired at each set of bending magnet parameters. The calculated energy spectrum parameters are summarized in Table 2, along with their change from the starting value. Representative spectra for each setting are presented in Figure 82.

Table 12. Results of Bending Magnet Ratio Changes. Δ is the change from the initial values.

Settings	N	E_{p0} [MeV]		FWHM [MeV]		$\bar{E}$ [MeV]	
		Measured	Δ	Measured	Δ	Measured	Δ
Initial Values	6	7.35 ± 0.04	-	1.84 ± 0.06	-	6.99 ± 0.02	-
F/C Ratio 1	13	7.45 ± <0.01	0.10 ± 0.04	1.88 ± 0.09	0.04 ± 0.11	7.13 ± 0.02	0.14 ± 0.03
F/C Ratio 2	17	7.67 ± 0.04	0.32 ±0.06	1.70 ± 0.09	-0.14 ± 0.11	7.32 ± 0.04	0.33 ± 0.05
F/C Ratio 3	20	7.15 ± <0.01	-0.20 ± 0.04	1.98 ± 0.10	0.14 ± 0.12	6.86 ± 0.04	-0.13 ± 0.05

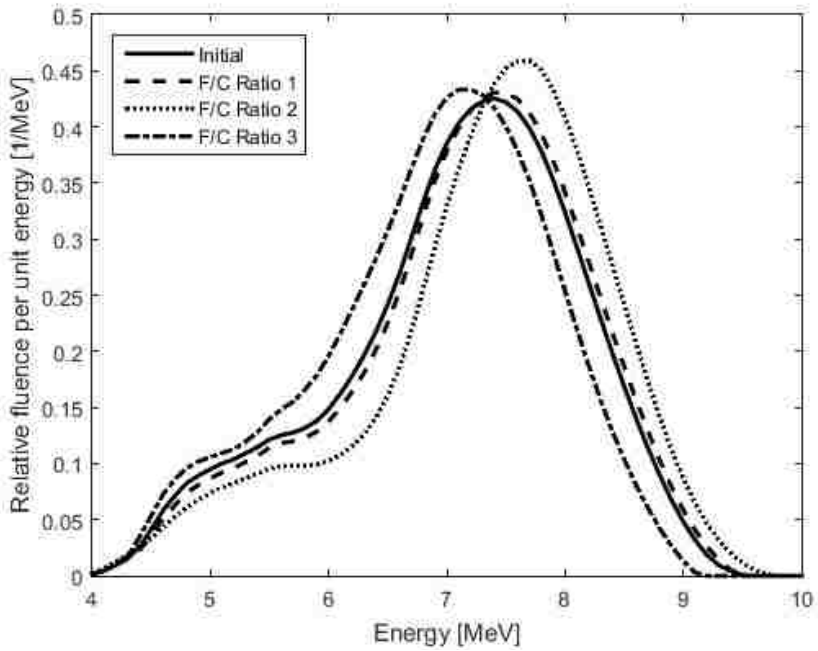

Figure 82. Average spectra for different bending magnet settings, for a nominal beam energy of 7 MeV. Refer to Table 11 and Table 12 for details on the linac settings and spectral parameters.

The bending magnet coarse current selects the center energy of the beam passband through the optics system (q.v. Section 1.4.2.1 and Figure 7). For a change in coarse current of 1.5 A at a fixed fine current (F/C Ratio 1 and F/C Ratio 3), we expected $\bar{E}$ shifts of +0.2 MeV and -0.2 MeV respectively. The measured shift values were +0.14 MeV for the increased current (F/C Ratio 1) and -0.13 MeV for the decreased current (F/C Ratio 3). The measured changes were in the proper direction, but of a smaller than theoretically predicted. For F/C Ratio 2, when both the coarse current and fine current were change, we measured a +0.33 MeV increase in the average

energy, compared to a theoretical value of +0.59 due to the coarse current change alone; this larger discrepancy in the change may be due to the modified bending fine current.

The bending fine current is an additional current in magnet M3 (Figure 6) used to change the focus of electron beam exiting the bending magnets. The magnetic field strength (and therefore the beam energy) in M3 is not linearly related to its current (personal communication, Neil McCann, Elekta Engineer); with the information available to us, we were unable to theoretically predict the effect of the bending fine current on the energy spectrum.

Changing the F/C ratio had the unanticipated result of modifying the FWHM as well as the $\bar{E}$ and E_{p0}. The largest changes in the FWHM occurred for F/C Ratio 2 and F/C Ratio 3. This may be due to the fine current being improperly turned to provide proper focusing of the electron beam.

5.3.2. High Power Phase Shifter Variations at 13 MeV

Using the 13 MeV beam, we increased or decreased the HPph setting; this should modify the FWHM of the energy spectra as well as its peak energy (private communications, Paul Kairdolf, Elekta Service Engineer). The HPph setting on the Versa HD was changed to provide a measured FWHM that matched a reference spectrum. The reference spectrum was the average spectrum measured on the Agility linac (Section 5.2). Once the FWHM was matched, the fine/coarse ratio was adjusted to shift the spectra to a more appropriate average energy. The collection of the HPph and F/C positions tested is presented in Table 13.

The 12.3 HPph setting provided a FWHM comparable to the reference spectrum, so it was used as the setting for modified F/C tests. The modified F/C ratio presented does not reflect all F/C variations we tested, only one that provided the best agreement of the tested values. For all HPph changes, the gun current and magnetron tuner were modified as needed to provide better

stability of the linac or, for the 12.5 HPph setting, the accelerator to operate at all. The dose rate was affected by HPph modifications, though this data was not recorded.

Table 13. 13 MeV Settings Variations. HPph is the high power phase shifter setting in cm. F/C is the bending fine to bending coarse ratio.

	Start/default	Decrease HPph	Increase HPph 1	Increase HPph 2	Modified F/C
HPph	11.8	11.0	12.5	12.3	12.3
F/C	85/4.2 = 4.94 %	4.94 %	4.94 %	4.94 %	95/4.2 = 4.42 %

Table 14. Results of varied linac tuning at a nominal 13 MeV energy.

Settings	N	E_{p0} [MeV]	FWHM [MeV]	$\bar{E}$ [MeV]
Reference (Agility)	-	13.00	1.96	12.07
Initial	20	13.31 ± 0.06	2.39 ± 0.10	12.28 ± 0.10
Decrease HPph	10	13.35 ± <0.01	2.80 ± 0.10	12.45 ± 0.03
Increase HPph 1	4	12.99 ± 0.05	2.35 ± 0.04	12.03 ± 0.03
Increase HPph 2	10	12.26 ± 0.03	2.09 ± 0.07	11.40 ± 0.04
Modified F/C Ratio	8	13.15 ± <0.01	1.76 ± 0.03	11.93 ± 0.05

Representative measured spectra and calculated PPD curves are presented in Figure 83Figure 87. The PDD curves were computed for the measured and reference spectra because PDDs are more familiar to a clinical physicist; PDD curves we not computed and displayed during the initial acquisitions because that functionality had not been implemented at that time. The measured PDD was checked for matching against the reference PDD for based on the commissioning matching criteria of 2%/0.5 mm.

The "Increased HPph 1" trial (Figure 85) was the only setting that provided PDDs that matched to within the clinical criteria; the spectra for this trial had similar E_{p0} and $\bar{E}$ values as compared to the reference, though a wider FWHM. This suggest that PDDs matched to the commissioning criteria do not mean equivalent linac performance in the energy regime. Because clinical PDDs are acquired using a homogenous water phantom, variations in the energy

spectrum, and therefore energy dependent scattering, do not produce a measureable effect. In the presence of heterogeneities or in the beam penumbra, inaccurate spectral assumptions such as a monoenergetic beam may have noticeable effects on calculated dose distributions [66]; though they can be more accurately modeled by using a polyenergetic spectral model of the electron beam [67].

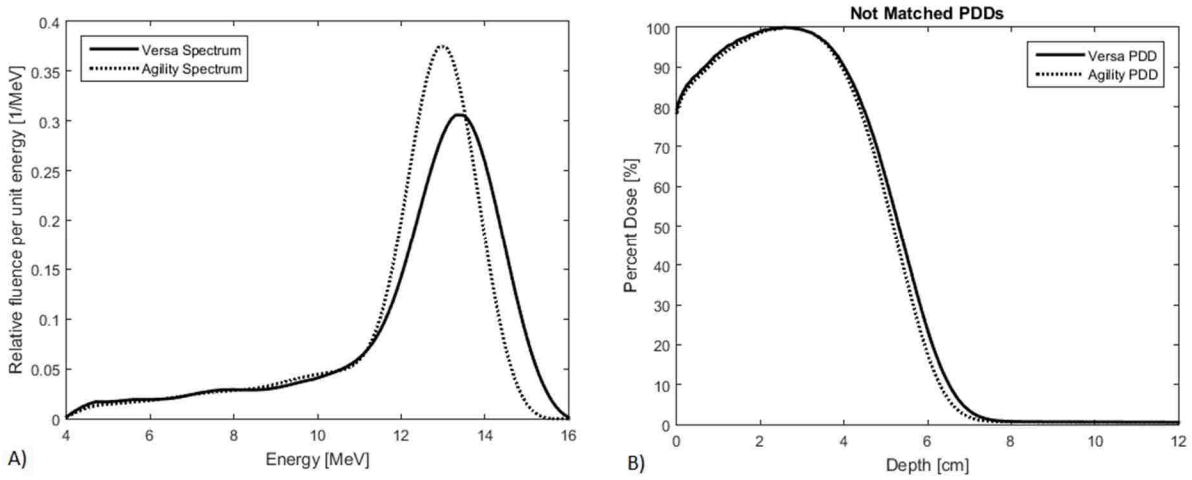

Figure 83. Default/original tuning. F/C = 4.94%, HPph = 11.8. PDDs not matched. A) shows the energy spectra; B) shows the calculated PDDs.

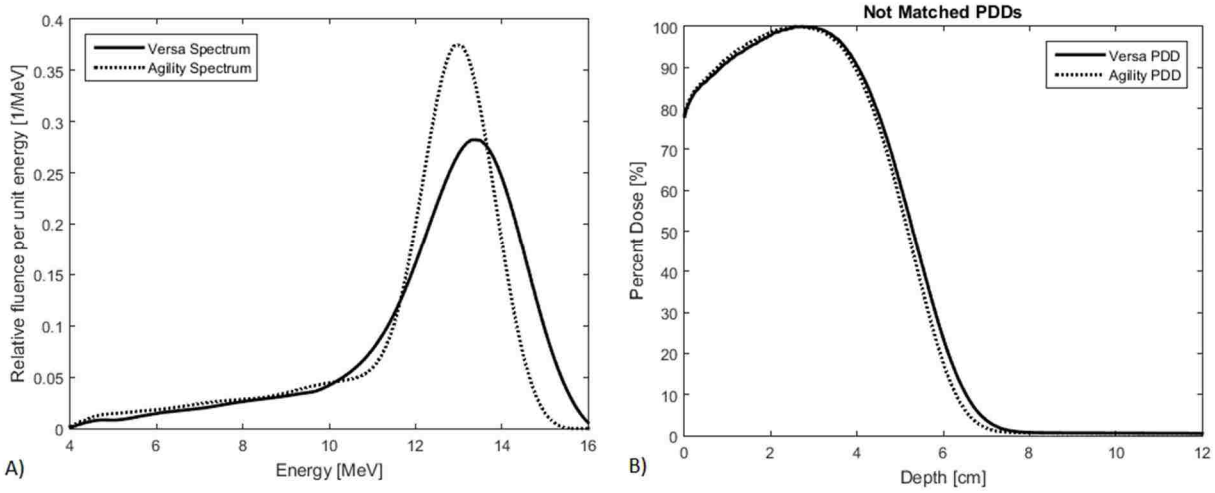

Figure 84. Decreased HPph. F/C = 4.94%, HPph = 11.0. PDDs not matched. A) shows the energy spectra; B) shows the calculated PDDs.

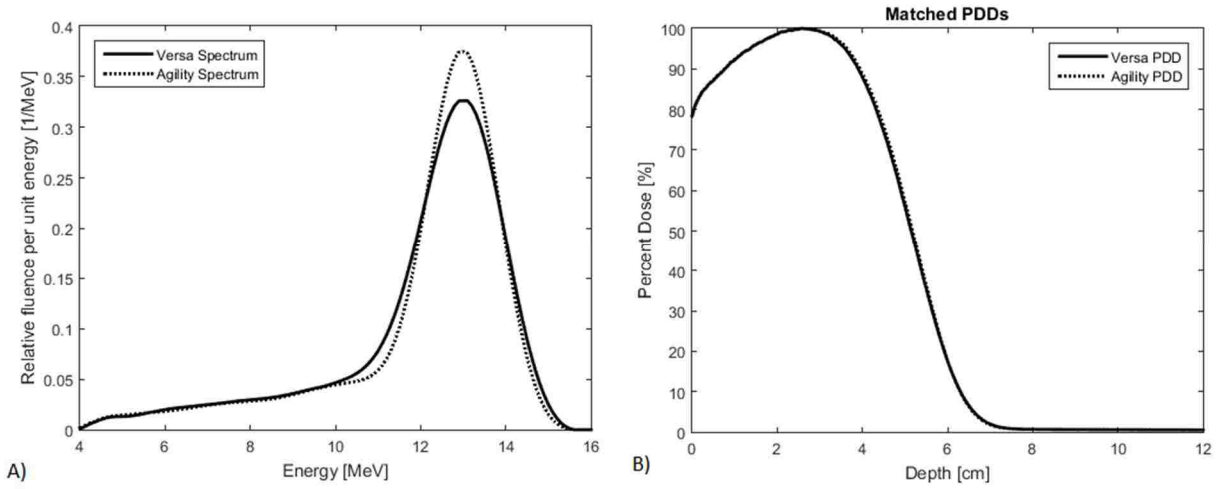

Figure 85. Increased HPph, test 1. F/C = 4.94%, HPph = 12.5. PDDs matched. A) shows the energy spectra; B) shows the calculated PDDs.

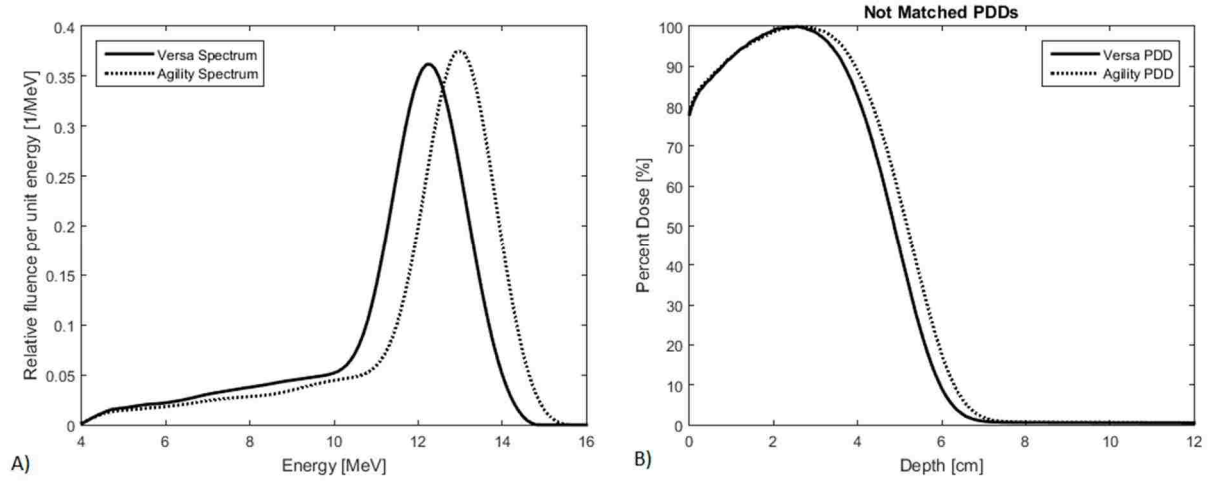

Figure 86. Increased HPph, test 2. F/C = 4.94%, HPph = 12.3. PDDs not matched. A) shows the energy spectra; B) shows the calculated PDDs.

5.4. Effect of Reduced Camera Exposure Time on Unfolded Spectrum Quality

The design goal of spectrometer was to acquire and display spectra at a 1 Hz interval. In practice, the acquisition interval results from the sum of the exposure time on the camera used for adequate signal accumulation, disk read/write time, processing time for spectral unfolding, and data plotting and display. Since the majority of this time was due to image acquisition and disk read/write time, we can increase the acquisition rate at the expense of measurement quality by reducing the exposure time. This section compares spectra acquired at 1000 ms exposure time

with spectra acquired at 100 ms exposure time. The 13 MeV beam was used, and all data was acquired during a single beam on instance.

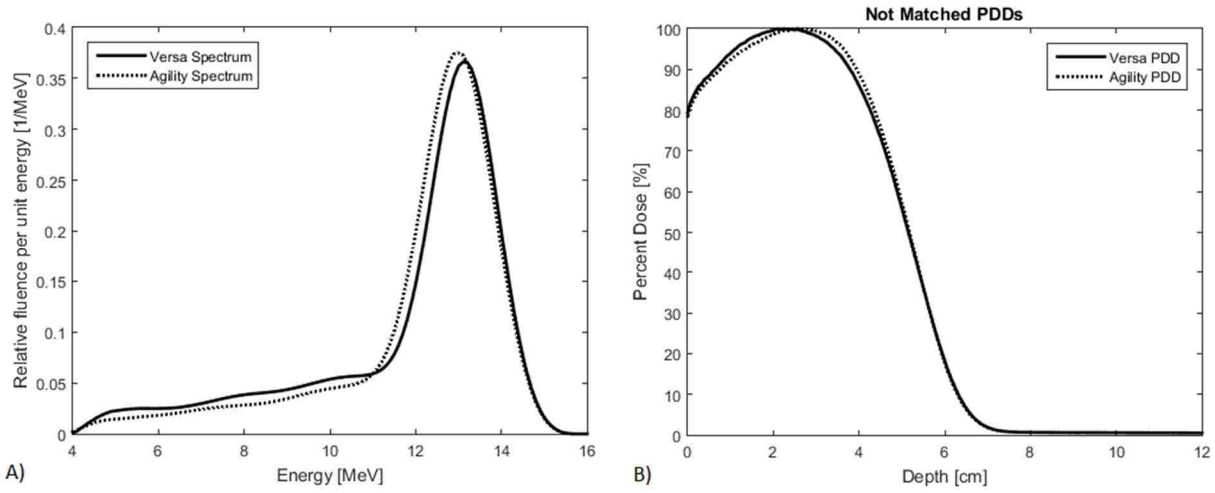

Figure 87. Modified F/C. F/C =4.42%, HPph = 12.3. PDDs not matched. A) shows the energy spectra; B) shows the calculated PDDs.

Figure 88 shows the fiber response for the two different exposures. As expected, a one tenth reduction in exposure time resulted in one tenth the total signal. The mean signal magnitude to mean uncertainty ratio decreased from to 11.7 at 1000 ms to 1.9 at 100 ms, indicating an overall degradation in signal quality. This reduction in the signal to uncertainty ratio resulted in increased 95% confidence bounds as shown in Figure 89.

While repeated measurements at 1000 ms did not show significant fluctuations in the reconstructed spectra (q.v. Section 5.2), 100 ms measurements exhibited a large variation in repeated measurements during the same irradiation (Figure 90). This may be due to uncharacterized small-timescale fluctuations in the linac performance, or limitation of the unfolding algorithm in the presence of large measurement uncertainties.

This section has demonstrated the potential tradeoff between exposure time and spectral variability. While this section only focused on a signal reduction due to decreased exposure time, the signal reduction could be achieved from using smaller fibers or a smaller entrance aperture to

the spectrometer; however, reduced signal resulting from modifying the detector system may result in an overall improvement of the spectral quality due to increased sampling resolution, or decreased signal smearing.

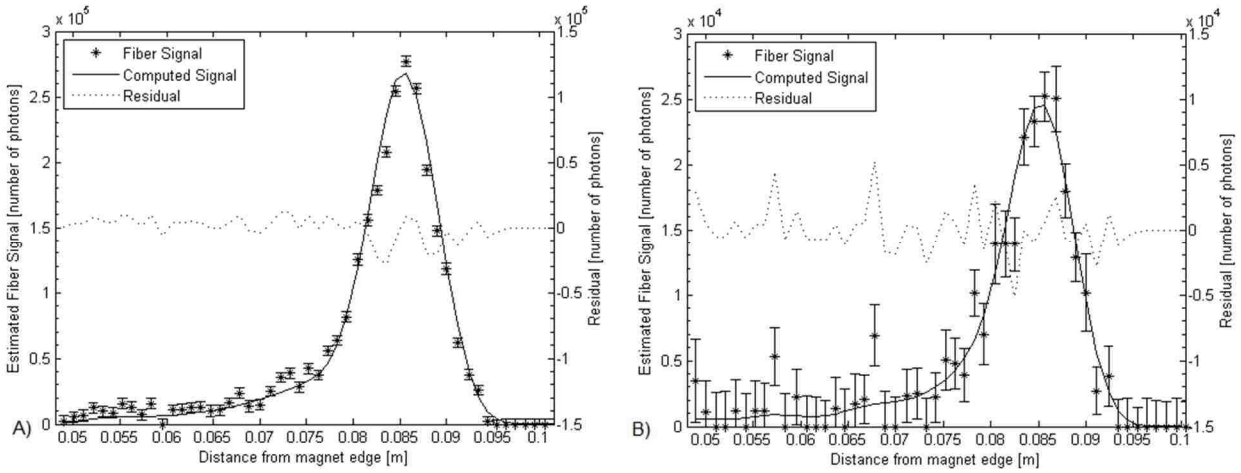

Figure 88. Comparison of fiber signal at different camera exposure times. A) Acquisition at 1000 ms exposure. B) Acquisition at 100 ms exposure.

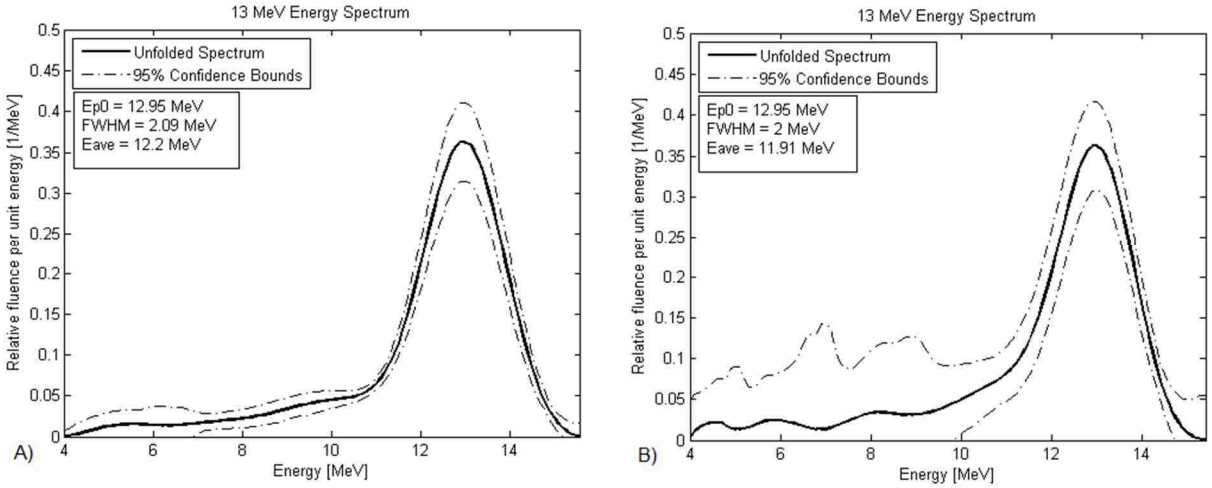

Figure 89. Comparison of unfolded energy spectra at different camera exposure times. The spectral descriptive quantities are listed in the top left corner. A) Representative acquisition at 1000 ms exposure. B) First acquisition at 100 ms exposure.

5.5. Energy Changes over Time

As discussed in the Section 1.2, QA measurements take place on daily, monthly, and yearly time intervals with different tests and tolerances. We assessed the spectrometer's ability to assist

in these QA measurements by acquiring spectra four months apart (May and September); we compared the spectra themselves, their descriptive quantities, and the calculated PDDs. According to AAPM TG-142 [13], the monthly tolerance range for electron energy constancy is 2%/2 mm referenced to $R_{50;}$ for annual tests, R_{50} has a tolerance of ±1 mm. The average spectra at all energies over the two months is plotted in Figure 91.

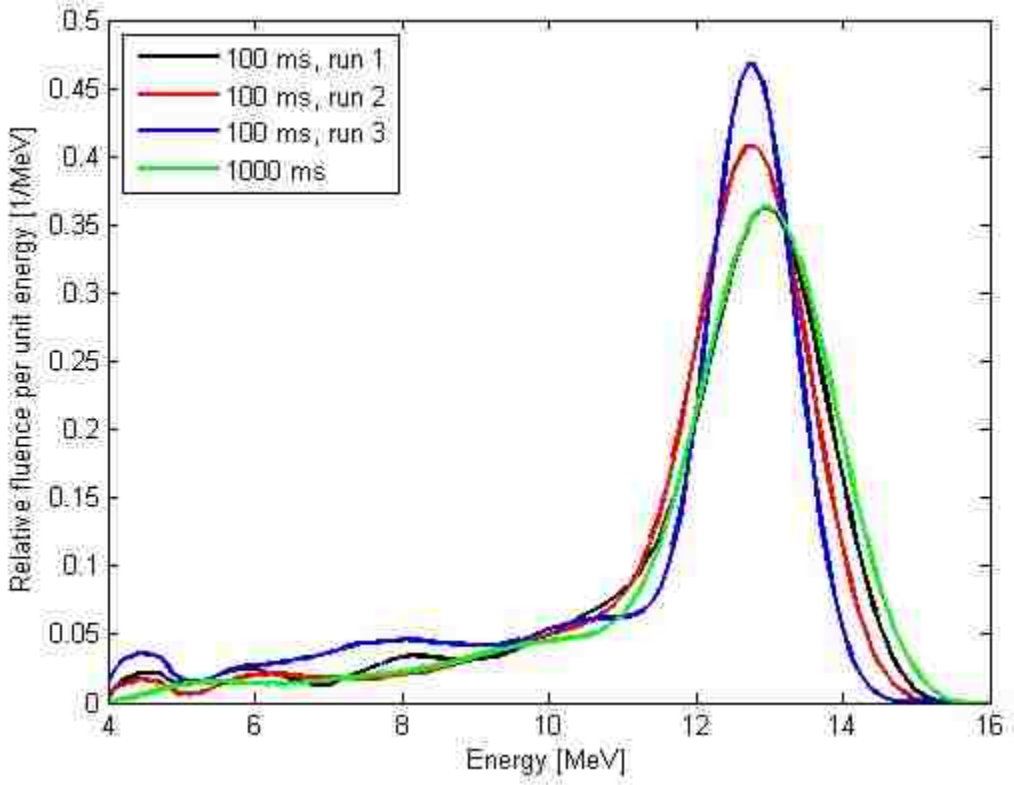

Figure 90. Repeat measurement stability at different exposure times.

Most spectra (7, 9, 10, 11, 13 MeV) were consistent between the two months, with only minor variations in the spectral descriptive parameters. The two highest energy beams, 16 and 20 MeV deviated the most between the two months, with 16 MeV having the largest change in all categories.

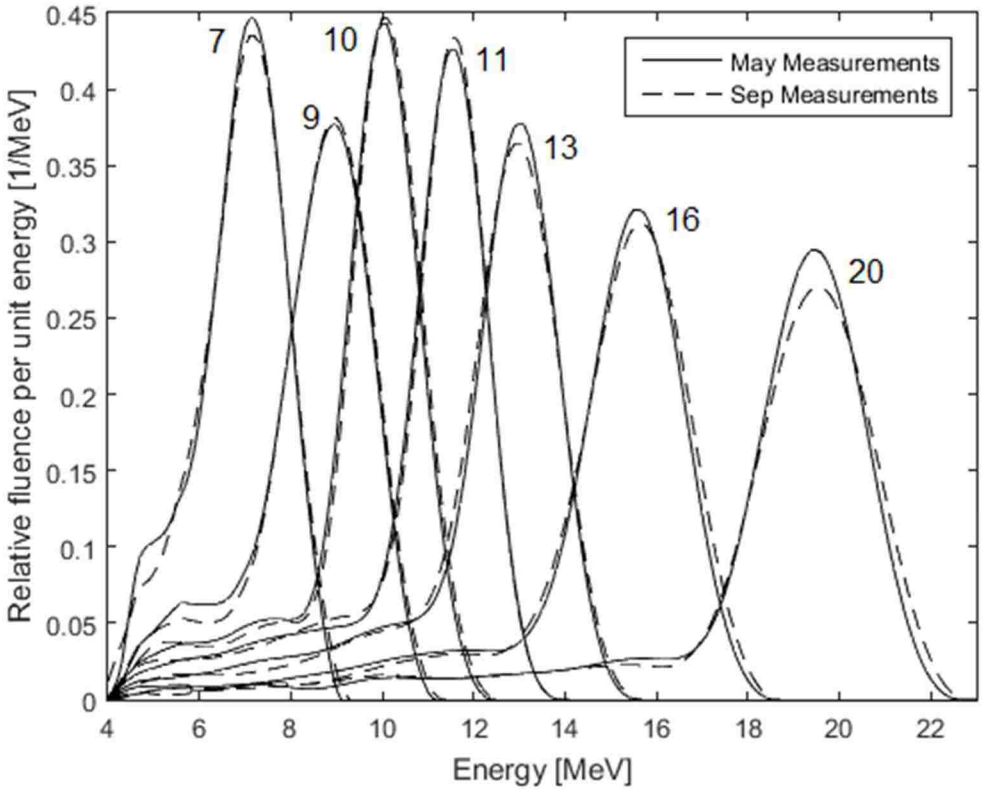

Figure 91. Comparison of average spectra taken four months apart. The numerical labels above the spectra are the nominal beam energy in MeV.

All R_{50} values were within the annual tolerance change of ≤1 mm difference. According to MBPCC documentation (Internal QA Report, MBPCC, Baton Rouge, LA), this linac passed all monthly QA measurements performed in May and the end of August, 2017, meaning no performance abnormalities were detected by the current routine clinical tools. All PDDs besides the 16 MeV beam matched at all points to within the commissioning criteria (2%/0.5 mm), indicating good overall stability on the linac behavior.

For the 16 MeV beam shown in Figure 92, the September spectrum exhibited a higher average energy, resulting from a shallower low energy tail, and an increased peak energy. This resulted in a potentially clinically significant change (i.e. up to 5% dose difference) in the calculated PDD for depths less than R_{100}. Such a change would not normally be detected until the next annual QA assessment scheduled for early 2018, because daily and monthly QA only spot

checks of R_{50} or R_{90} values, which matched between May and September. This result suggests that an electron spectrometer may be able to detect clinically significant dose differences that the current QA methods would not detect.

Table 15. Energy spectra descriptive quantities for measurements made four months apart. Shaded cells indicated values that were not consistent between the two months.

Nominal Energy [MeV]	E_{p0} [MeV]			FWHM [MeV]			$\bar{E}$ [MeV]		
	T = 0	T = 4 months	$\lvert\Delta\rvert$	T = 0	T = 4 months	$\lvert\Delta\rvert$	T = 4 months	T = 4 months	$\lvert\Delta\rvert$
7 MeV	7.15 ± <0.01	7.15 ± <0.01	0	1.82 ± 0.13	1.93 ± 0.10	0.11	6.86 ± 0.03	6.88 ± 0.02	0.02
9 MeV	8.95 ± <0.01	8.95 ± <0.01	0	2.06 ± 0.03	2.15 ± 0.10	0.09	8.40 ± 0.03	8.48 ± 0.01	0.08
10 MeV	10.05 ± <0.01	10.05 ± <0.01	0	1.65 ± 0.10	1.67 ± 0.11	0.02	9.48 ± 0.02	9.54 ± 0.02	0.06
11 MeV	11.55 ± <0.01	11.55 ± <0.01	0	1.75 ± <0.01	1.56 ± 0.09	0.19	10.74 ± 0.04	10.72 ± 0.04	0.02
13 MeV	13.02 ± 0.06	12.95 ± <0.01	0.07	1.95 ± 0.10	2.04 ± 0.10	0.09	12.10 ± 0.04	12.16 ± 0.04	0.06
16 MeV	15.55 ± <0.01	15.68 ± 0.06	0.13	2.33 ± 0.12	2.58 ± 0.08	0.25	14.57 ± 0.11	14.86 ± 0.08	0.29
20 MeV	19.45 ± <0.01	19.55 ± <0.01	0.10	2.63 ± 0.10	2.83 ± 0.10	0.20	18.15 ± 0.19	18.15 ± 0.04	0

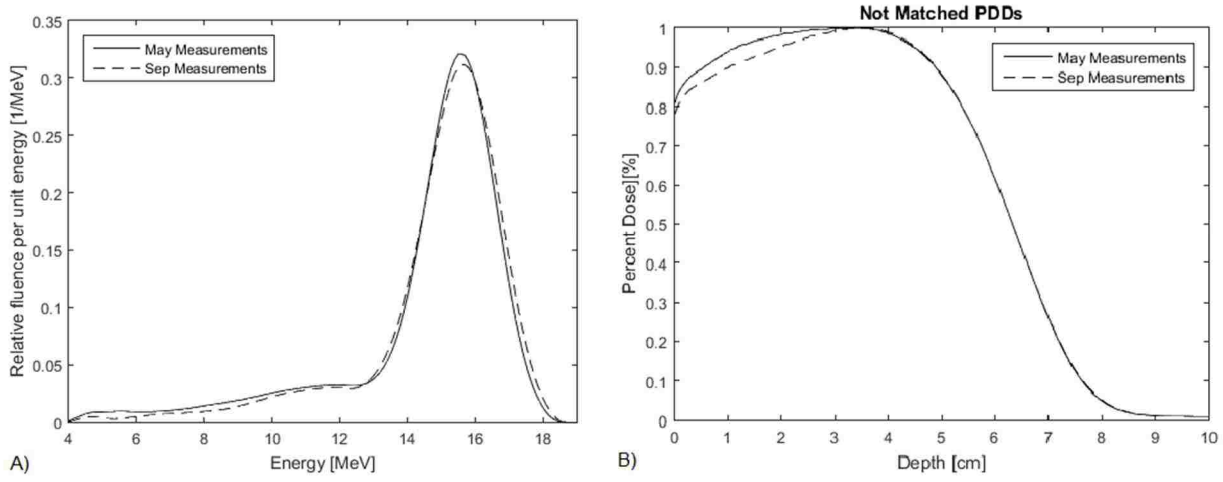

Figure 92. Comparison between May and September energy spectra (A) and PDD curve (B) at 16 MeV. Note the difference in the PDD curves at shallow depths.

Table 16. Calculated PDD descriptive quantities four months apart.

Nominal Energy [MeV]	R_{90} [cm] T = 0	R_{90} [cm] T = 4 months	$\lvert\Delta\rvert$	R_{50} [cm] T = 0	R_{50} [cm] T = 4 months	$\lvert\Delta\rvert$	R_p [cm] T = 0	R_p [cm] T = 4 months	$\lvert\Delta\rvert$
7	2.05 ± <0.01	2.07 ± 0.03	0.02	2.75 ± <0.01	2.75 ± <0.01	0.00	3.45 ± <0.01	3.46 ± 0.01	0.01
9	2.60 ± <0.01	2.60 ± <0.01	0.00	3.48 ± 0.03	3.50 ± <0.01	0.02	4.33 ± <0.01	4.35 ± <0.01	0.02
10	3.05 ± <0.01	3.07 ± 0.03	0.02	4.00 ± <0.01	4.02 ± 0.03	0.02	4.90 ± <0.01	4.93 ± <0.01	0.03
11	3.50 ± <0.01	3.50 ± <0.01	0.00	4.60 ± <0.01	4.60 ± <0.01	0.00	5.61 ± <0.01	5.62 ± 0.01	0.01
13	3.97 ± 0.03	4.00 ± <0.01	0.03	5.20 ± <0.01	5.20 ± <0.01	0.00	6.35 ± <0.01	6.34 ± <0.01	0.01
16	4.83 ± 0.06	4.90 ± <0.01	0.07	6.30 ± <0.01	6.35 ± <0.01	0.05	7.63 ± <0.01	7.66 ± 0.01	0.03
20	6.00 ± 0.09	6.00 ± 0.05	0.00	7.90 ± <0.01	7.93 ± 0.03	0.03	9.49 ± <0.01	9.54 ± <0.01	0.05

6. CONCLUSIONS

This work presented a real-time electron energy spectrometer for use with medical accelerators that is able to acquire and display spectra at a rate of 0.8 Hz, and an energy measurement range of 4 to 25 MeV. This device enables a detailed study of linac operating performance and stability that, to the authors' knowledge, has not been achievable using current clinical tools. The spectrometer allowed an Elekta service engineer to evaluate linac performance for multiple operating parameters in a quicker, more informative way than by using a scanning water tank. The energy spectrum produced by a linac is a more direct measurement of linac performance, unlike depth-dose curves or ionization measurements, as it directly relates to the operating parameters of the machine, e.g. bending magnet strength and average energy[68]. Measurements of the energy spectra revealed changes in linac performance that were not caught by routine QA measurements.

Another application of this device is facilitating beam matching based on energy spectra in lieu of PDD curves. This would be valuable for verifying consistent linac performance after repairs, or during installation and commissioning of a new treatment machine. This work demonstrated that the spectrometer allowed rapid assessment of the effect of linac tuning parameters on the energy spectra. Measured spectra can be used to calculate PDDs, illustrated in this work with a simplified PDD model; the spectrometer can provide real-time PDD calculations as well as energy spectra for electron beams.

6.1. Possible Design Improvements

The spectrometer design presented in this work was not the only possible design, or even an optimal design, but it successfully illustrates the capability for real-time measurements. The design here leaned heavily on simplicity and low-cost, incorporating a scintillating fiber readout

system for which materials were already available. The experience with this design points to various possible improvements that could increase the quality of measured spectra, particularly by simplifying the spectral unfolding model.

For example, the detector's physical resolution could be increased by moving to smaller fibers (though this would decrease the signal output), or by adding a second row of offset fibers downstream from the current one. The fibers can also be mounted to a motorized linear stage so that they can be shifted; this would allow finer sampling of the dispersed electron fluence, providing higher spatial resolution at the cost of increased complexity and decreased readout speed. Septa added between fibers in the 2D bundle would reduce or eliminate light sharing, simplifying signal processing and possibly decreasing overall measurement uncertainty. Alternatively, the fiber-camera detector could be replaced by a pixelated semiconductor detector that directly images the dispersed electron fluence. A direct imaging detector would likely be more compact, and possibly allow the spectrometer to be physically mounted to the linac gantry. This would simplify setup, and allow for spectral acquisitions at gantry angles other than 3 o'clock or 9 o'clock . A larger magnet block that allows for 180º electron trajectories, rather than ~90º used in this work, would allow a simplification of the unfolding algorithm; however this would increase the overall size of the device.

A single interface and control program should be implemented to simplify the use of the spectrometer. The current system had separate image acquisition and analysis software (PixeLINK Capture and MATLAB respectively), complicating use. This resulted in images being acquired and written to disk, to then be read back into memory for processing. The added overhead of disk write/read times resulted in a desynchronization between the 1-second image acquisition time and the analysis; this resulted in ~1.25 seconds being needed to capture, write,

read, process and display a spectrum if used continually. Furthermore, the current analysis software was unable to queue image acquisition, and instead ran a "wait" routine until a new image was acquired. A unified software environment should allow image data acquired on demand, directly into memory, reducing the overhead time for image import. This would also allow for variable control of the exposure time, allowing the software to achieve a requested refresh rate by modifying exposure time on the fly.

6.2. Limitations

The primary limitation of our spectrometer was the lack of a calibration using an externally well-characterized electron source. If we had access to a source with a variable energy and spectral distribution, we could determine any systematic errors created by unfolding method. In this work, we were seeking to characterize our spectrometer's performance, while also characterizing the linac. We were not able to establish physical "truth," only consistency with other methods. The current approximate verification that our spectrometer is producing accurate results is based on empirical relations, given in ICRU 35[5], using the most probable energy and the practical electron range (q.v. Section 2.2.1); this only provided a consistency measurement, not a full assessment of systematic uncertainties. Our secondary accuracy check was comparing spectra acquired with the real-time system to those acquired by the passive system (q.v. Section 5.1). While the spectra shapes were similar, we cannot fully assess if they are the real spectra. To that end, as long as the systematic uncertainties remain constant, and the spectrometer functions is a predicable, reproducible fashion, it can still be effectively used as clinical tool.

A secondary limitation to the spectrometer was our simplifications for both the magnetic field and the physics model used to generate the DRF kernels. We did not fully model all 3D electron trajectories within the magnet block; this may have introduced small errors in the final

electron positions and angles at the detector plane. Additionally, the physics model used during our DRF generation did not fully model in-air, or large angle probabilistic scatter. Both of these simplifications should only introduce unchanging systematic uncertainties. While the most direct solution to this limitation is generating DRF kernels using a full, 3D Monte Carlo simulation, it offers little practical improvement over the current method because without a proper calibration source, we cannot fully assess the improvement. For the purpose of developing and demonstrating the utility of a real-time spectrometer system for constancy measurements, the simplified physics model was appropriate.

REFERENCES

1. Siegel R, Ma J, Zou Z, Jemal A. Cancer statistics, 2014. *CA: A Cancer Journal for Clinicians.* 2014;64(1):9-29.

2. ASTRO. Fast Facts About Radiation Therapy. 2012; https://www.astro.org/News-and-Media/Media-Resources/FAQs/Fast-Facts-About-Radiation-Therapy/Index.aspx. Accessed June 4, 2014, 2014.

3. Henderson S, Holmes S, Alonso J, et al. *Accelerators for America's Future.* US DOE;2009.

4. Hogstrom KR, Almond PR. Review of electron beam therapy physics. *Phys Med Biol.* 2006;51(13):R455-489.

5. ICRU. *International Commission on Radiation Units and Measurements, "Radiation Dosimetry: Electrons with Initial Energies Between 1 and 50 MeV".* Bethesda, MD: International Commision on Radiation Units and Measurements;1984. 35.

6. Deasy JO, Almond PR, McEllistrem MT. Measured electron energy and angular distributions from clinical accelerators. *Med Phys.* 1996;23(5):675-684.

7. Gerbi BJ, Antolak JA, Deibel FC, et al. Recommendations for clinical electron beam dosimetry: Supplement to the recommendations of Task Group 25. *Medical Physics.* 2009;36(7):3239-3279.

8. Svensson H, Hettinger G. Dosimetric Measurements at the Nordic Medical Accelerators I. Characteristics of the radiation beam. *Acta Radiologica: Therapy, Physics, Biology.* 1971;10(3):369-384.

9. Faddegon BA, Blevis I. Electron spectra derived from depth dose distributions. *Med Phys.* 2000;27(3):514-526.

10. Ali OA, Willemse CA, Shaw W, O'Reilly FH, du Plessis FC. Monte carlo electron source model validation for an Elekta Precise linac. *Med Phys.* 2011;38(5):2366-2373.

11. Kok JG, Welleweerd J. Finding mechanisms responsible for the spectral distribution of electron beams produced by a linear accelerator. *Med Phys.* 1999;26(12):2589-2596.

12. Das IJ, Cheng C-W, Watts RJ, et al. Accelerator beam data commissioning equipment and procedures: Report of the TG-106 of the Therapy Physics Committee of the AAPM. *Medical Physics.* 2008;35(9):4186-4215.

13. Klein EE, Hanley J, Bayouth J, et al. Task Group 142 report: Quality assurance of medical acceleratorsa). *Medical Physics.* 2009;36(9):4197-4212.

14. McLaughlin D. *Energy Spectra Comparisons for Matched Clinical Electron Beams on Elekta Linear Accelerators using a Permanent Magnet Spectrometer* [Master of Science]: Physics & Astronomy, Louisiana State University; 2013.

15. Humphries S. *Principles of charged particle acceleration.* J. Wiley, Dover; 1986, 2012.

16. Karzmark CJ, Nunan CS, Tanabe E. *Medical Electron Accelerators.* McGraw-Hill, Incorporated, Health Professions Division; 1993.

17. Pozar DA. *Microwave Engineering.* 4th Edition ed. Hoboken, New Jersey: John Wiley & Sons; 2012.

18. Scharf WH. *Biomedical Particle Accelerators.* Woodbury, New York: AIP Press; 1994.

19. Karzmark CJ, Pering NC. Electron linear accelerators for radiation therapy: history, principles and contemporary developments. *Physics in Medicine & Biology.* 1973;18(3):321.

20. Bjarngard BE, Piontek RW, Svensson GK. Electron scattering and collimation system for a 12-MeV linear accelerator. *Med Phys.* 1976;3(3):153-158.

21. Carver RL, Hogstrom KR, Price MJ, LeBlanc JD, Pitcher GM. Real-time simulator for designing electron dual scattering foil systems. *Journal of applied clinical medical physics / American College of Medical Physics.* 2014;15(6):4849.

22. Kainz KK, Antolak JA, Almond PR, Bloch CD, Hogstrom KR. Dual scattering foil design for poly-energetic electron beams. *Phys Med Biol.* 2005;50(5):755-767.

23. Kok JGM. Fixed bending current for Elekta SL25 linear accelerators. *Journal of Medical Engineering & Technology.* 2001;25(4):169-172.

24. Karzmark CJ. Advances in linear accelerator design for radiotherapy. *Medical Physics.* 1984;11(2):105-128.

25. Houwen W. A doubly achromatic asymmetric three-magnet 90° deflection system. *Medical Physics.* 1994;21(7):1065-1068.

26. Botman JIM, Bates T, Hagedoorn HL. A Double Focusing Magnet System for a Medical Linear Electron-Accelerator. *Nucl Instrum Meth B.* 1985;10-1(May):796-798.

27. Bates T, Inventor; Google Patents, assignee. Deflection system for charged-particle beam. 1983.

28. de la Vega JM, Guirado D, Vilches M, Perdices JI, Lallena AM. Obtaining the intrinsic electron spectrum of linear accelerators using the relation between the current of the

bending magnet and the absorbed dose in water. *Radiotherapy and Oncology.* 2008;86(1):109-113.

29. McDermott PN. *Tutorials in Radiotherapy Physics: Advanced Topics with Problems and Solutions.* CRC Press; 2016.

30. Cooper RK, Carter RG. High-Power RF Transmission. 2005.

31. Ohsawa S, Abe I, Yokota M, et al. High-power hybrid attenuator & phase-shifter systems. Paper presented at: Linear Accelerator Conference1990; Albuquerque, NM, USA.

32. Limited E. *Elekta Digital Linear Accelerator Corrective Maintenance Manual, HT and RF System.* Crawley, UK2011.

33. Roy D, Tremblay D. Design of electron spectrometers. *Reports on Progress in Physics.* 1990;53(12):1621.

34. Enge HA. Particle Detection Systems. *IEEE Transactions on Nuclear Science.* 1979;26(2):2420.

35. Helliwell TM. *Special Relativity.* University Science Books; 2010.

36. Enge HA. Magnetic spectrographs. *Physics Today.* 1967;20(7):65.

37. Siegbahn K. III - BETA-RAY SPECTROMETER THEORY AND DESIGN. MAGNETIC ALPHA-RAY SPECTROSCOPY. HIGH RESOLUTION SPECTROSCOPY. *Alpha-, Beta- and Gamma-Ray Spectroscopy*. Amsterdam: Elsevier; 1968:79-202.

38. Deasy JO, Almond PR, McEllistrem MT, Ross CK. A simple magnetic spectrometer for radiotherapy electron beams. *Med Phys.* 1994;21(11):1703-1714.

39. Gobet F, Caron J, Bessieres I, et al. Experimental and Monte Carlo absolute characterization of a medical electron beam using a magnetic spectrometer. *Radiation Measurements.* 2016;86:16-23.

40. McLaughlin DJ, Hogstrom KR, Carver RL, et al. Permanent-magnet energy spectrometer for electron beams from radiotherapy accelerators. *Med Phys.* 2015;42(9):5517-5529.

41. Sorcini BB, Rosander S. Energy distributions from a racetrack microtron measured with a magnetic spectrometer. *Med Phys.* 1993;20(3):695-702.

42. Bushberg JS, J. Anthony; Leidholdt, Edwin; Boone, John. *The Essential Physics of the Medical Imaging, 3rd ed.* Lippincott Williams & Wilkins; 2012.

43. Tirpak LS, Thomas; Shi, Jie; Simon, William; Main, Bill; Pawlak, Dan; and Mallia, Pierre. Beam Quality Verification Using IC Profiler with Quad Wedge Accessories. *Customer Technical Bulletin.* 2015.

44. Bjork P, Knoos T, Nilsson P. Influence of initial electron beam characteristics on monte carlo calculated absorbed dose distributions for linear accelerator electron beams. *Phys Med Biol.* 2002;47(22):4019-4041.

45. Aljarrah K, Sharp GC, Neicu T, Jiang SB. Determination of the initial beam parameters in Monte Carlo linac simulation. *Medical Physics.* 2006;33(4):850-858.

46. Bush K, Zavgorodni S, Beckham W. Inference of the optimal pretarget electron beam parameters in a Monte Carlo virtual linac model through simulated annealing. *Medical Physics.* 2009;36(6):2309-2319.

47. Harris GM. *Development and Validation of an Electron Monte Carlo Model for the Elekta Infinity Accelerator* [Master of Science]: Physics & Astronomy, Louisiana State University; 2012.

48. Ma CM, Faddegon BA, Rogers DWO, Mackie TR. Accurate characterization of Monte Carlo calculated electron beams for radiotherapy. *Medical Physics.* 1997;24(3):401-416.

49. Ma CM, Jiang SB. Monte Carlo modelling of electron beams from medical accelerators. *Phys Med Biol.* 1999;44(12):R157-189.

50. Chetty IJ, Curran B, Cygler JE, et al. Report of the AAPM Task Group No. 105: Issues associated with clinical implementation of Monte Carlo-based photon and electron external beam treatment planning. *Medical Physics.* 2007;34(12):4818-4853.

51. Gahn C, Tsakiris GD, Witte KJ, Thirolf P, Habs D. A novel 45-channel electron spectrometer for high intensity laser-plasma interaction studies. *Review of Scientific Instruments.* 2000;71(4):1642-1645.

52. Livingood J. *The Optics of Dipole Magnets.* New York, New York: Academic Press; 1969.

53. Antonuk LE. Electronic portal imaging devices: a review and historical perspective of contemporary technologies and research. *Phys Med Biol.* 2002;47(6):R31-65.

54. Kramberger G. Solid State Detectors for High Radiation Environments. In: Fabjan CW, Schopper H, eds. *Detectors for Particles and Radiation. Part 2: Systems and Applications*. Berlin, Heidelberg: Springer Berlin Heidelberg; 2011:210-250.

55. Saint-Gobain. Scintillating Optical Fibers. In: Saint-Gobain, ed. *Scintillation Products*: Saint-Gobain; 2011.

56. Palais JC. *Fiber Optic Communications.* Fifth Edition ed. Upper Saddle River, NJ: Pearson Education Inc.; 2005.

57. Schneider CA, Rasband WS, Eliceiri KW. NIH Image to ImageJ: 25 years of Image Analysis. *Nature methods.* 2012;9(7):671-675.

58. PixeLINK. PixeLINK PL-954&955 Datasheet. Ontario, CAN: PixeLINK.

59. Werner BL, Khan FM, Deibel FC. A model for calculating electron beam scattering in treatment planning. *Med Phys.* 1982;9(2):180-187.

60. Landau L. On the energy loss of fast particles by ionization. *Journal of Physics, USSR.* 1944;8(1-6):201-205.

61. Agostinelli S, Allison J, Amako K, et al. GEANT4-a simulation toolkit. *Nucl Instrum Meth A.* 2003;506(3):250-303.

62. Allison J, Amako K, Apostolakis J, et al. Recent developments in GEANT4. *Nucl Instrum Meth A.* 2016;835:186-225.

63. Allison J, Amako K, Apostolakis J, et al. Geant4 developments and applications. *Ieee Transactions on Nuclear Science.* 2006;53(1):270-278.

64. Mayneord WV. Energy Absorption. IV—The Mathematical Theory of Integral Dose in Radium Therapy. *The British Journal of Radiology.* 1945;18(205):12-19.

65. Ruf M, Muller S, Setzer S, Schmidt LP. Beam position and energy monitoring in compact linear accelerators for radiotherapy. *IEEE transactions on bio-medical engineering.* 2014;61(2):381-387.

66. Boyd RA, Hogstrom KR, Rosen, II. Effect of using an initial polyenergetic spectrum with the pencil-beam redefinition algorithm for electron-dose calculations in water. *Med Phys.* 1998;25(11):2176-2185.

67. Boyd RA, Hogstrom KR, Starkschall G. Electron pencil-beam redefinition algorithm dose calculations in the presence of heterogeneities. *Med Phys.* 2001;28(10):2096-2104.

68. Brown KL. Achromatic Beam Translation Systems for Linear Accelerators. *Review of Scientific Instruments.* 1956;27(11):959-963.

APPENDIX: FIBER BRACKET DRAWINGS

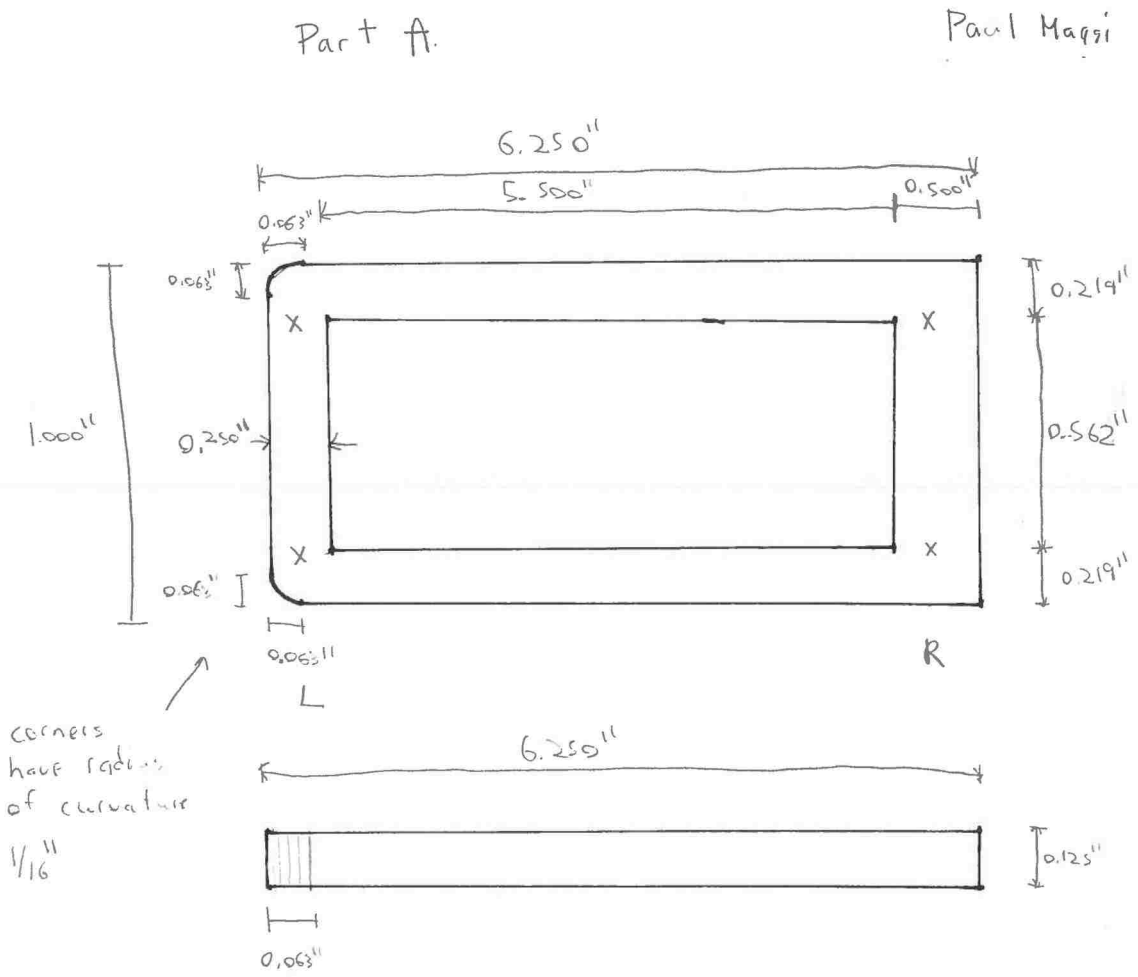

X = #6-32 taped screw hole
located in the center of the vertical portion, 0.219" from the top / bottom edge
↳ 0.125" inches inward on the left vertical
0.250" on the right vertical

Part B, perspective view Paul Maggi

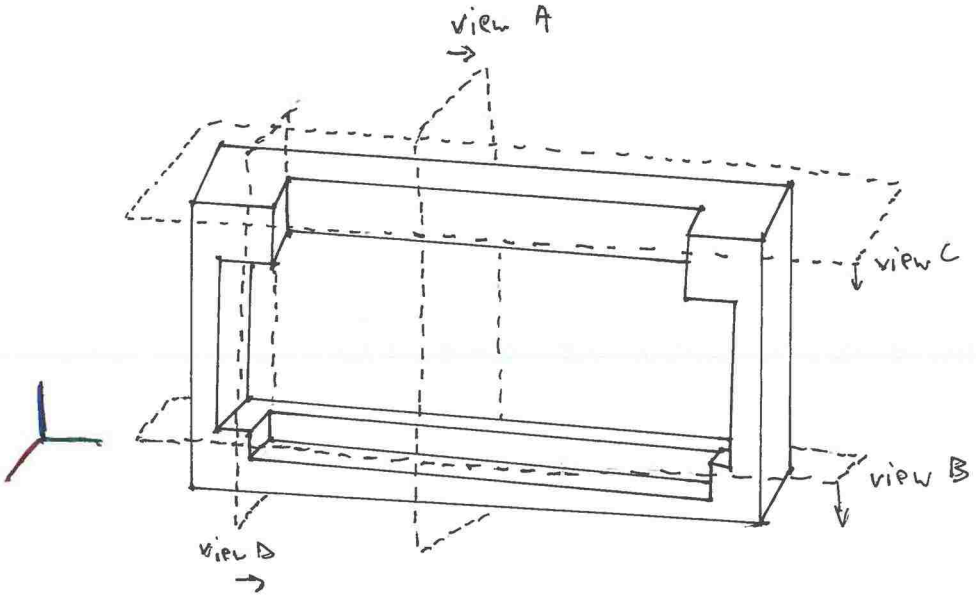

Part B

Paul Maggi

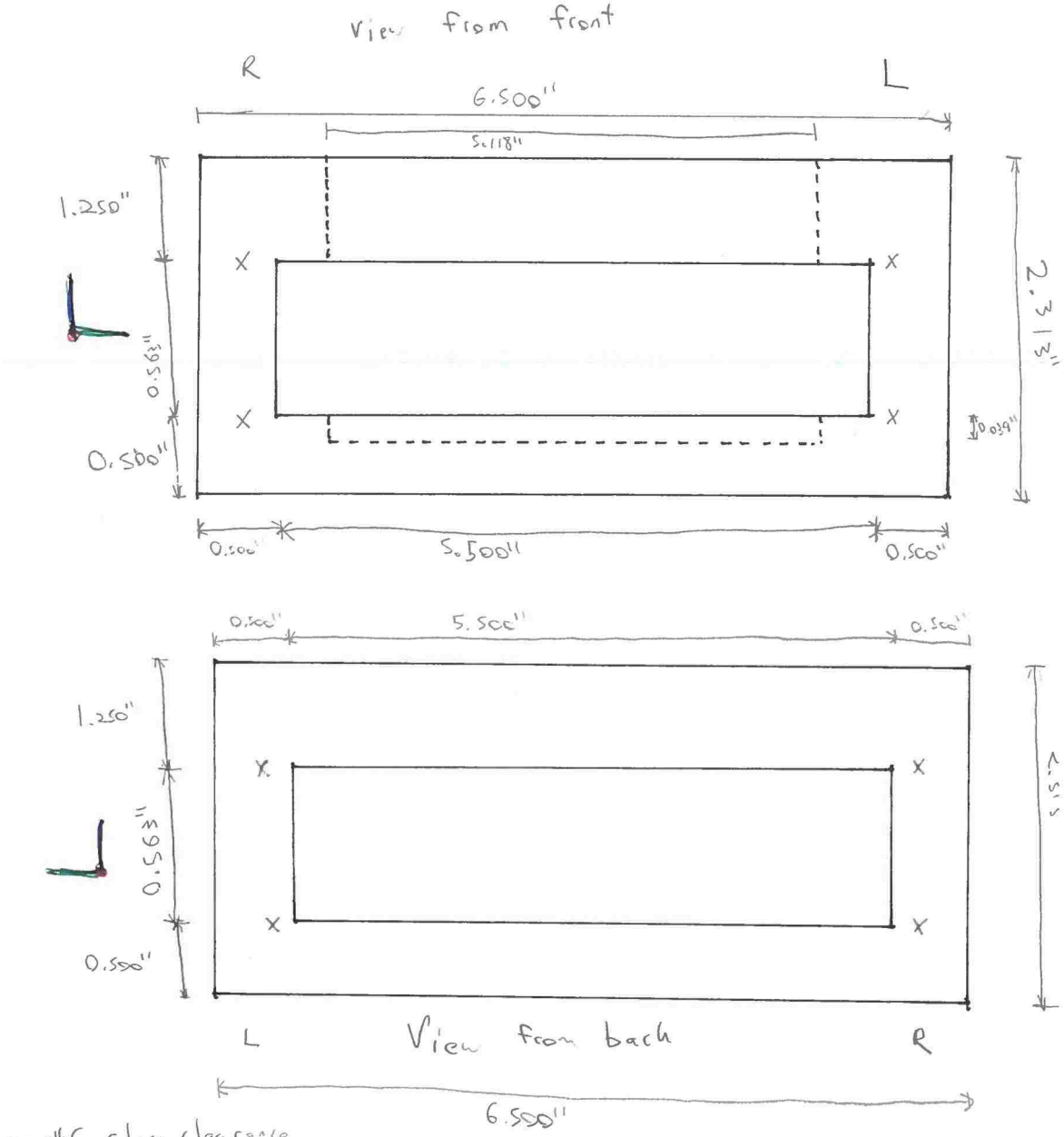

X = #6 close clearance hole, parallel to aperture opening → clearance holes to match holes on part A.

(top holes 1.250" from top, bottom holes 0.500" from bottom).

1 cc holes 0.125" inward. Right holes [illegible]

Paul Maggi

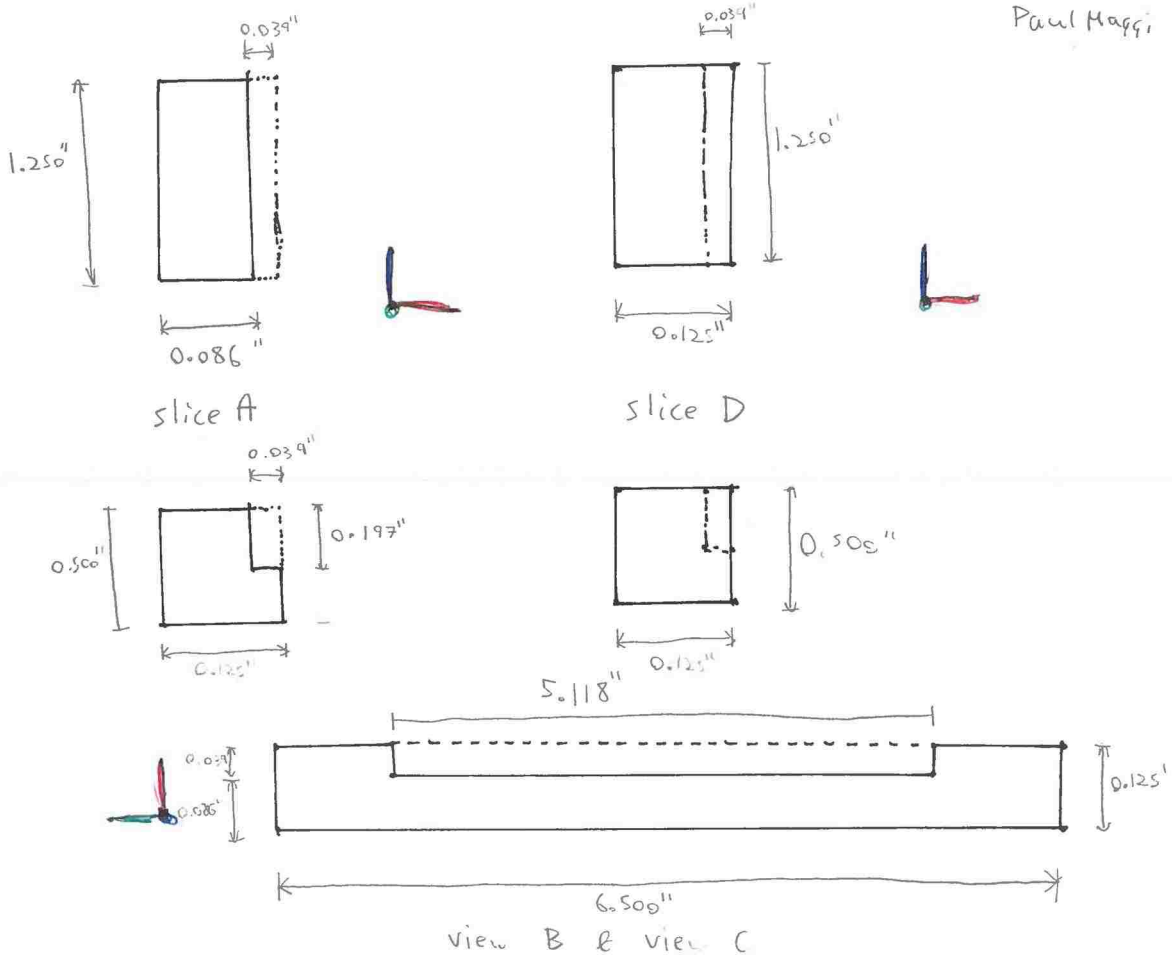

Part B, slice view

---- indicates information in other dimensions (depth.

VITA

Paul Maggi was born and raised in Modesto, CA. He attended the California Polytechnic State University, San Luis Obispo (Cal Poly SLO), where he obtained a B.S. in Electrical Engineering with a minor in Physics in Spring of 2012. That summer, in the timespan of a week, he got married to his wife Christine, moved across the country from California to Baton Rouge, and started graduate school at LSU. Upon completion of his PhD, he will begin a postdoc in Baltimore, MD, continuing his research interest in radiation metrology.